Neuron

Article

Dissecting human cortical similarity networks across the lifespan

Highlights

- We analyze lifespan maturation patterns in morphometric networks in the human brain
- Sensory and association cortices show divergent maturation in morphometric networks
- Morphometric network growth correlates with function, metabolism, and transcriptome
- Morphometric network-based normative models detect individual brain deviations

Authors

Xinyuan Liang, Lianglong Sun, Mingrui Xia, ..., Alzheimer's Disease Neuroimaging Initiative, MCADI, DIDA-MDD Working Group, Yong He

Correspondence

yong.he@bnu.edu.cn

In brief

Liang et al. characterize the lifespan maturation of human cortical morphometric networks (0–80 years, 33,937 participants), revealing distinct trajectories between sensory and association cortices. These developmental patterns correlate with functional, metabolic, and transcriptomic profiles. Morphometric network-based normative modeling identifies disorder-specific, connectivity-phenotypic deviations, establishing a quantitative benchmark for assessing individual brain variations.

Liang et al., 2025, Neuron *113*, 1–21

https://doi.org/10.1016/j.neuron.2025.06.018

Please cite this article in press as: Liang et al., Dissecting human cortical similarity networks across the lifespan, Neuron (2025), https://doi.org/10.1016/j.neuron.2025.06.018

Neuron

CellPress

Article

Dissecting human cortical similarity networks across the lifespan

Xinyuan Liang,[1,2,3,42] Lianglong Sun,[1,2,3,42] Mingrui Xia,[1,2,3] Tengda Zhao,[1,2,3] Gaolang Gong,[1,2,3,4] Qiongling Li,[1,2,3] Xuhong Liao,[5] Zaixu Cui,[4] Dingna Duan,[1,2,3] Chenxuan Pang,[1,2,3] Qian Wang,[1,2,3] Qian Yu,[1,2,3] Yanchao Bi,[1,6,7] Pindong Chen,[8] Rui Chen,[1] Yuan Chen,[9] Taolin Chen,[10] Jingliang Cheng,[9] Yuqi Cheng,[11] Zhengjia Dai,[1,2,3] Yao Deng,[1] Yuyin Ding,[1] Qi Dong,[1] Jia-Hong Gao,[7,12,13] Qiyong Gong,[10,14,15] Ying Han,[16] Zaizhu Han,[1,3] Chu-Chung Huang,[17] Ruiwang Huang,[1,3,18] Ran Huo,[19] Lingjiang Li,[20,21] Ching-Po Lin,[22,23] Qixiang Lin,[1,2,3]

(Author list continued on next page)

[1]State Key Laboratory of Cognitive Neuroscience and Learning, Beijing Normal University, Beijing 100875, China
[2]Beijing Key Laboratory of Brain Imaging and Connectomics, Beijing Normal University, Beijing 100875, China
[3]IDG/McGovern Institute for Brain Research, Beijing Normal University, Beijing 100875, China
[4]Chinese Institute for Brain Research, Beijing 102206, China
[5]School of Systems Science, Beijing Normal University, Beijing 100875, China
[6]School of Psychological and Cognitive Sciences and Beijing Key Laboratory of Behavior and Mental Health, Peking University, Beijing 100871, China
[7]IDG/McGovern Institute for Brain Research, Peking University, Beijing 100871, China
[8]Brainnetome Center & National Laboratory of Pattern Recognition, Institute of Automation, Chinese Academy of Sciences, Beijing 100190, China
[9]Department of Magnetic Resonance Imaging, The First Affiliated Hospital of Zhengzhou University, Zhengzhou 450052, China
[10]Department of Radiology, Huaxi MR Research Center (HMRRC), Institute of Radiology, Functional and Molecular Imaging Key Laboratory of Sichuan Province, West China Hospital of Sichuan University, Chengdu 610041, China
[11]Department of Psychiatry, First Affiliated Hospital of Kunming Medical University, Kunming 650032, China
[12]Center for MRI Research, Academy for Advanced Interdisciplinary Studies, Peking University, Beijing 100871, China
[13]Beijing City Key Laboratory for Medical Physics and Engineering, Institute of Heavy Ion Physics, School of Physics, Peking University, Beijing 100871, China
[14]Research Unit of Psychoradiology, Chinese Academy of Medical Sciences, Chengdu 610052, China
[15]Xiamen Key Laboratory of Psychoradiology and Neuromodulation, Department of Radiology, West China Xiamen Hospital of Sichuan University, Xiamen 361021, China
[16]Department of Neurology, Xuanwu Hospital of Capital Medical University, Beijing 100053, China

(Affiliations continued on next page)

SUMMARY

The human cortex exhibits remarkable morphometric similarity between regions; however, the form and extent of lifespan network remodeling remain unknown. Here, we show the spatiotemporal maturation of morphometric brain networks, using multimodal neuroimaging data from 33,937 healthy participants aged 0–80 years. Global architecture matures from birth to early adulthood through enhanced modularity and small worldness. Early development features cytoarchitecturally distinct remodeling: sensory cortices exhibit increased morphometric differentiation, paralimbic cortices show increased morphometric similarity, and association cortices retain stable hub roles. Morphology-function coupling peaks in early adolescence and then decreases, supporting protracted functional maturation. These growth patterns of morphometric networks are correlated with gene expression related to synaptic signaling, neurodevelopment, and metabolism. Normative models based on morphometric networks identify person-specific, connectivity-phenotypic deviations in 1,202 patients with brain disorders. These data provide a blueprint for elucidating the principle of cortical network reconfiguration and a benchmark for quantifying interindividual network variations.

INTRODUCTION

Cortical morphology represents the fundamental structural architecture of the cerebral cortex.[1] The morphometric features of cortical structures, including cortical thickness (CT), surface area (SA), and folding, undergo complex, genetically regulated, and regionally heterogeneous growth processes across the human lifespan.[2–7] However, cortical growth is not confined to a

Please cite this article in press as: Liang et al., Dissecting human cortical similarity networks across the lifespan, Neuron (2025), https://doi.org/10.1016/j.neuron.2025.06.018

Bangshan Liu,[20,21] Chao Liu,[1,3] Ningyu Liu,[1] Ying Liu,[19] Yong Liu,[24] Jing Lu,[1] Leilei Ma,[1] Weiwei Men,[12,13] Shaozheng Qin,[1,2,3,4] Wen Qin,[25] Jiang Qiu,[26,27,28] Shijun Qiu,[29] Tianmei Si,[30] Shuping Tan,[31] Yanqing Tang,[32] Sha Tao,[1] Dawei Wang,[33] Fei Wang,[34] Jiali Wang,[1] Jinhui Wang,[35,36,37] Pan Wang,[38] Xiaoqin Wang,[26,27] Yanpei Wang,[1] Dongtao Wei,[26,27] Yankun Wu,[30] Peng Xie,[39,40] Xiufeng Xu,[11] Yuehua Xu,[1,2,3] Zhilei Xu,[1,2,3] Liyuan Yang,[1,2,3] Chunshui Yu,[25] Huishu Yuan,[19] Zilong Zeng,[1,2,3] Haibo Zhang,[1] Xi Zhang,[41] Gai Zhao,[1] Yanting Zheng,[29] Suyu Zhong,[24] Alzheimer's Disese Neuroimagig Initiative, MCADI, DIDA-MDD Working Group, and Yong He[1,2,3,4,43,*]

[17]Key Laboratory of Brain Functional Genomics (Ministry of Education), Affiliated Mental Health Center (ECNU), School of Psychology and Cognitive Science, East China Normal University, Shanghai 200062, China
[18]School of Psychology, South China Normal University, Guangzhou 510631, China
[19]Department of Radiology, Peking University Third Hospital, Beijing 100191, China
[20]Department of Psychiatry and National Clinical Research Center for Mental Disorders, The Second Xiangya Hospital of Central South University, Changsha 410011, China
[21]Mental Health Institute of Central South University, China National Technology Institute on Mental Disorders, Hunan Technology Institute of Psychiatry, Hunan Key Laboratory of Psychiatry and Mental Health, Hunan Medical Center for Mental Health, Changsha 410011, China
[22]Institute of Neuroscience, National Yang Ming Chiao Tung University, Taipei 112304, China
[23]Department of Education and Research, Taipei City Hospital, Taipei 103212, China
[24]Center for Artificial Intelligence in Medical Imaging, School of Artificial Intelligence, Beijing University of Posts and Telecommunications, Beijing 100876, China
[25]Department of Radiology & Tianjin Key Laboratory of Functional Imaging & Tianjin Institute of Radiology & State Key Laboratory of Experimental Hematology, Tianjin Medical University General Hospital, Tianjin 300052, China
[26]Key Laboratory of Cognition and Personality (SWU), Ministry of Education, Chongqing 400715, China
[27]Department of Psychology, Southwest University, Chongqing 400715, China
[28]Southwest University Branch, Collaborative Innovation Center of Assessment Toward Basic Education Quality at Beijing Normal University, Chongqing 400715, China
[29]Department of Radiology, The First Affiliated Hospital of Guangzhou University of Chinese Medicine, Guangzhou 510405, China
[30]Peking University Sixth Hospital, Peking University Institute of Mental Health, NHC Key Laboratory of Mental Health (Peking University), National Clinical Research Center for Mental Disorders (Peking University Sixth Hospital), Peking University, Beijing 100191, China
[31]Beijing Huilongguan Hospital, Peking University Huilongguan Clinical Medical School, Beijing 100096, China
[32]Department of Psychiatry, Shengjing Hospital of China Medical University, Shenyang 117004, China
[33]Department of Radiology, Qilu Hospital of Shandong University, Ji'nan 250012, China
[34]Department of Psychiatry, The First Affiliated Hospital of China Medical University, Shenyang 110001, China
[35]Institute for Brain Research and Rehabilitation, South China Normal University, Guangzhou 510631, China
[36]Guangdong Key Laboratory of Mental Health and Cognitive Science, South China Normal University, Guangzhou 510631, China
[37]Key Laboratory of Brain, Cognition and Education Sciences, Ministry of Education, South China Normal University, Guangzhou 510631, China
[38]Department of Neurology, Tianjin Huanhu Hospital, Tianjin University, Tianjin 300072, China
[39]Chongqing Key Laboratory of Neurobiology, Chongqing 400016, China
[40]Department of Neurology, The First Affiliated Hospital of Chongqing Medical University, Chongqing 400016, China
[41]Department of Neurology, the Second Medical Centre, National Clinical Research Centre for Geriatric Diseases, Chinese PLA General Hospital, Beijing 100853, China
[42]These authors contributed equally
[43]Lead contact
*Correspondence: yong.he@bnu.edu.cn

https://doi.org/10.1016/j.neuron.2025.06.018

single region but exhibits morphometric similarity between regions, thereby forming an interconnected network.[8–10] At the microscopic level, the homophily wiring principle provides a theoretical basis for the relationship between cortical morphometric similarity and axonal projection.[10–12] Histological studies of several species, such as *Caenorhabditis elegans*,[13] mice,[14] cats,[15,16] and macaques,[17,18] have shown that neurons or cortical regions sharing similar cytoarchitectural features tend to be axonally connected. Recent technological advances have facilitated the investigation of person-specific morphometric networks in terms of single or multiple structural features.[9,10] Specifically, several intriguing models for network reconstruction have been proposed, including the morphometric similarity network method, which estimates the pairwise correlations between structural feature vectors,[19] and the morphometric inverse divergence (MIND) method, which estimates the pairwise divergence between the multivariate distributions of multiple structural features.[20] These person-specific, morphology-based brain networks at the macroscale have also been shown to effectively recapitulate cortical cytoarchitectural classes, tract-tracing axonal connectivity, and gene co-expression profiles.[9,10] Despite these advances, however, the form and extent of the growth of cortical morphology networks across the human lifespan remain largely unknown.

Previous studies have reported age-related alterations in cortical morphometric networks on the basis of single or multiple structural features derived from magnetic resonance imaging (MRI) data.[8,9] While these studies have provided valuable insights into the development and degeneration of morphological organization at specific ages or growth stages, they have several

Please cite this article in press as: Liang et al., Dissecting human cortical similarity networks across the lifespan, Neuron (2025), https://doi.org/10.1016/j.neuron.2025.06.018

important limitations. First, the majority of previous studies have been limited to narrow age windows, such as fetal ages,[21] neonatal ages,[22] childhood and adolescence,[23–25] and adulthood.[26–28] Several recent studies have sought to cover a broad age range, such as the entirety of adulthood[26–28] or the period from childhood to late adulthood,[29,30] but they lack data from early years of life, which are particularly important for cortical network development. Moreover, the restricted sample sizes employed in these studies (typically below 2,000) present a substantial challenge for robustly estimating the lifespan growth of morphometric networks. Second, previous findings regarding age-related alterations in cortical morphometric networks have indicated notable inconsistencies. For example, increased connections in cortical morphometric networks have been observed in the paralimbic cortices (insula and cingulate) during the fetal period,[21] adolescence,[23] and adulthood,[26] whereas other studies have reported the opposite pattern.[22,30] With respect to the statistical modeling of network phenotypes, some researchers have reported linear trajectories with increasing age,[21–23,25] whereas others have identified nonlinear trajectories.[24,26,27,29] The inconsistencies among these studies could be attributed, at least in part, to the heterogeneity of the study cohorts, imaging platforms, acquisition protocols, data processing, and statistical models. Therefore, a robust mapping of lifespan changes in cortical morphometric networks necessitates a substantial sample size of individuals from birth to old age, as well as the use of advanced techniques and methods, such as rigorous quality control, harmonized data processing methods, biologically validated methods of network construction, standardized statistical modeling, and comprehensive validation analyses.

Once lifespan growth models of morphometric brain networks are established, critical questions remain that require further investigation. One such question is how morphometric networks coordinate with the functional connectome across the human lifespan. Structural brain networks provide a critical anatomical substrate that shapes functional networks.[31,32] Morphometric similarity networks (assessed via the MIND method) approximate axonal connectivity networks,[19,20] offering a plausible alternative to structural connectome. Notably, Dorfschmidt et al.[23] reported divergent morphology-function coupling patterns during adolescence: paralimbic regions exhibit increased coupling, whereas neocortical regions show reduced coupling, promoting functional modular diversity. However, no studies have yet examined lifespan changes in morphology-function coupling in the cortical networks from birth to late adulthood. Another important but unresolved question is the biological basis of morphometric network maturation, particularly links to metabolic demands and transcriptomic signatures. Finally, the potential clinical utility of the morphometric network as a reference model for quantifying individual heterogeneity in patients with neuropsychiatric disorders remains unvalidated, although lifespan growth charts of single morphometric features have been well established.[4,33]

Here, we address these important questions by collecting a large, multimodal neuroimaging dataset comprising data from 33,937 healthy participants age 0–80 years, collected from 141 scanning sites worldwide. We first constructed person-specific, morphology-based brain networks using the state-of-the-art MIND method[20] because of its unique advantages over other methods in terms of technical reliability, biological validity, and developmental sensitivity.[10,20] We then mapped the normative growth patterns of the morphometric brain networks at the global, class, and regional levels and morphology-function coupling across the lifespan, with a particular focus on key developmental milestones. We also examined the biological relevance of network growth by linking it to brain metabolism and gene expression profiles. Finally, the potential clinical value of the normative models of the morphometric networks was validated for three representative brain disorders (1,202 patients): Alzheimer's disease (AD), major depressive disorder (MDD), and autism spectrum disorder (ASD). Overall, this study elucidates the lifespan growth patterns of morphometric brain networks and their functional significance, biological underpinnings, and clinical relevance.

RESULTS

After rigorous quality control,[34] we ultimately included the following data samples (Figure 1A; Table S1): (1) the structural images of 33,937 healthy participants (aged 0–80 years), employed to delineate the lifespan growth patterns of morphometric brain networks (aim I, Figure 1B); (2) a subsample of 32,887 healthy participants (aged 0–80 years) with both structural and functional images for investigating morphology-function coupling across the lifespan (aim II, Figure 1C); (3) positron emission tomography (PET)-based brain imaging data from 165 participants (aged 20–82 years)[35] and gene expression data from 6 donors (aged 24–57 years),[36] employed to investigate biological relevance of lifespan growth of morphometric brain networks (aim III, Figure 1D); and (4) the structural images of 1,202 patients with brain disorders, encompassing 180 patients with AD, 622 patients with MDD, and 400 patients with ASD, which were used to validate the clinical relevance of the network-based normative models (aim IV, Figure 1E). The detailed demographics and imaging protocols of the datasets are presented in Table S2.

For each participant, we first extracted five cortical morphology features (CT, SA, gray matter volume [Vol], mean curvature [MC], and sulcal depth [SD]) (see STAR Methods). Each individual's cortical surface was subsequently partitioned into 318 parcels of similar volume size via a modified Desikan-Killiany atlas[37] (referred to as DK-318) and an age-specific surface registration strategy (see STAR Methods). Each morphometric feature was further standardized across all vertices (*Z* score) to ensure the removal of global mean effects and the alignment of all features to a common scale. Finally, we generated a 318 × 318 within-participant morphometric network by estimating the pairwise divergence between the multivariate distributions of the 5 features[20] (Figure 1B). To investigate the lifespan normative growth of the networks, we applied a generalized additive model for location, scale, and shape (GAMLSS),[38,39] with network phenotype as the dependent variable, age as a smoothing term, sex and the Euler number as covariates, and scanner site as a random effect.

Global-level growth of morphometric brain networks across the lifespan

To characterize the global growth patterns of morphometric networks, two measures were initially considered: the global

Please cite this article in press as: Liang et al., Dissecting human cortical similarity networks across the lifespan, Neuron (2025), https://doi.org/10.1016/j.neuron.2025.06.018

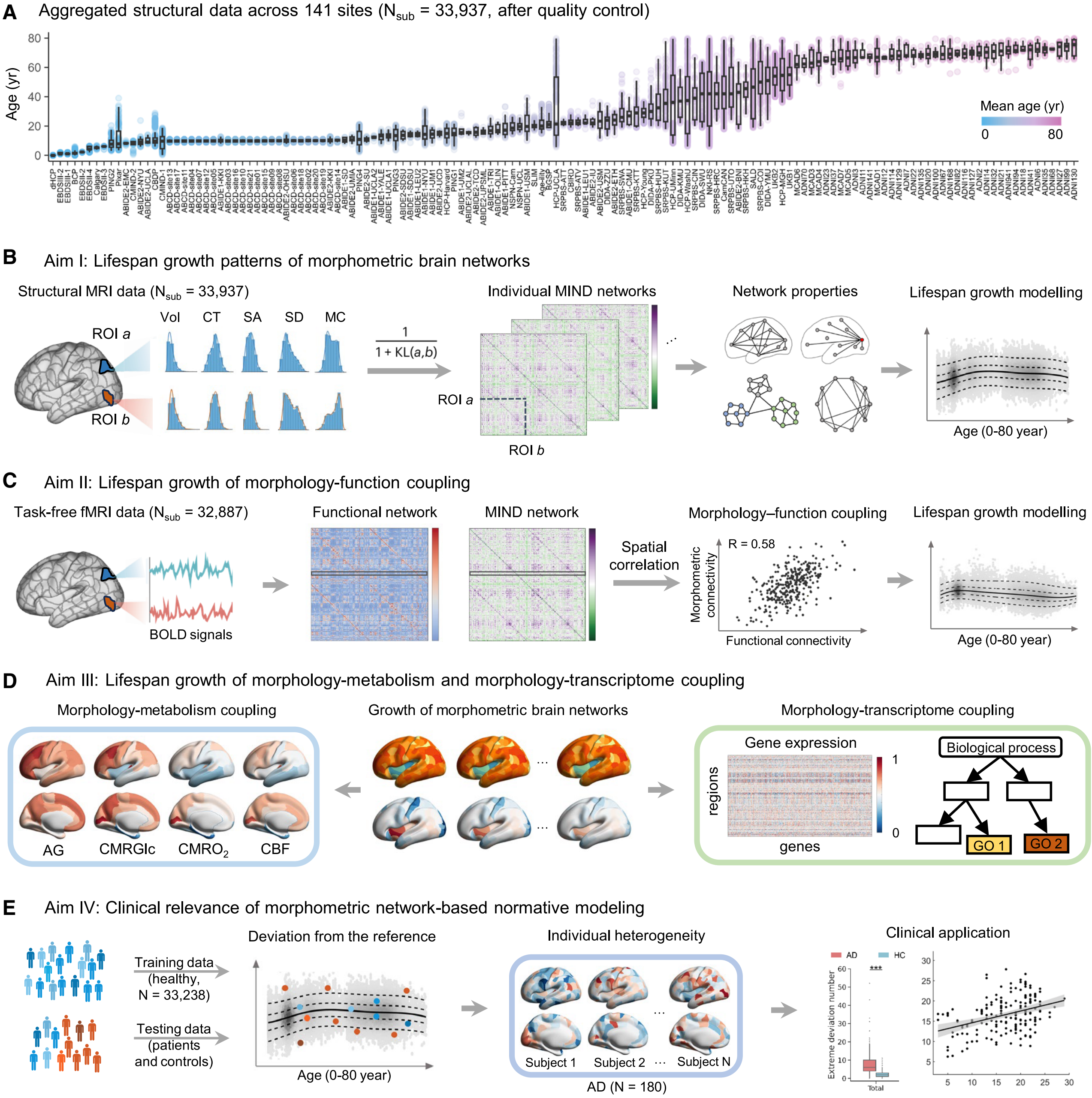

Figure 1. Flowchart of the data analysis

(A) Age distribution of participants at each site.

(B) Overview of the lifespan growth mapping of the morphometric network (the MIND method).

(C) The functional network for each participant was constructed and then used to estimate morphology-function coupling.

(D) The metabolic and gene expression data were used to explore the potential biological basis of morphometric network growths.

(E) Characterization of individual deviations in morphometric network metrics for patients with a given disorder (orange dots) and controls (blue dots). Case-control differences and clinical predictions were then conducted on individual deviation patterns.

variance and the global mean. The lifespan growth curve of the global variance (standard deviation) of the networks exhibited a nonlinear increase from birth to early adolescence (peaking at 13.9 years; 95% bootstrapped confidence interval [CI] [12.5, 15.7]), followed by a relatively stable plateau (Figure 2A). This indicated an overall increase in the degree of diversity in morphometric similarity during early development. Furthermore, the morphometric network exhibited a decrease in global mean strength (indicating increased overall morphometric differentiation) during infancy and childhood, reaching a minimum in early

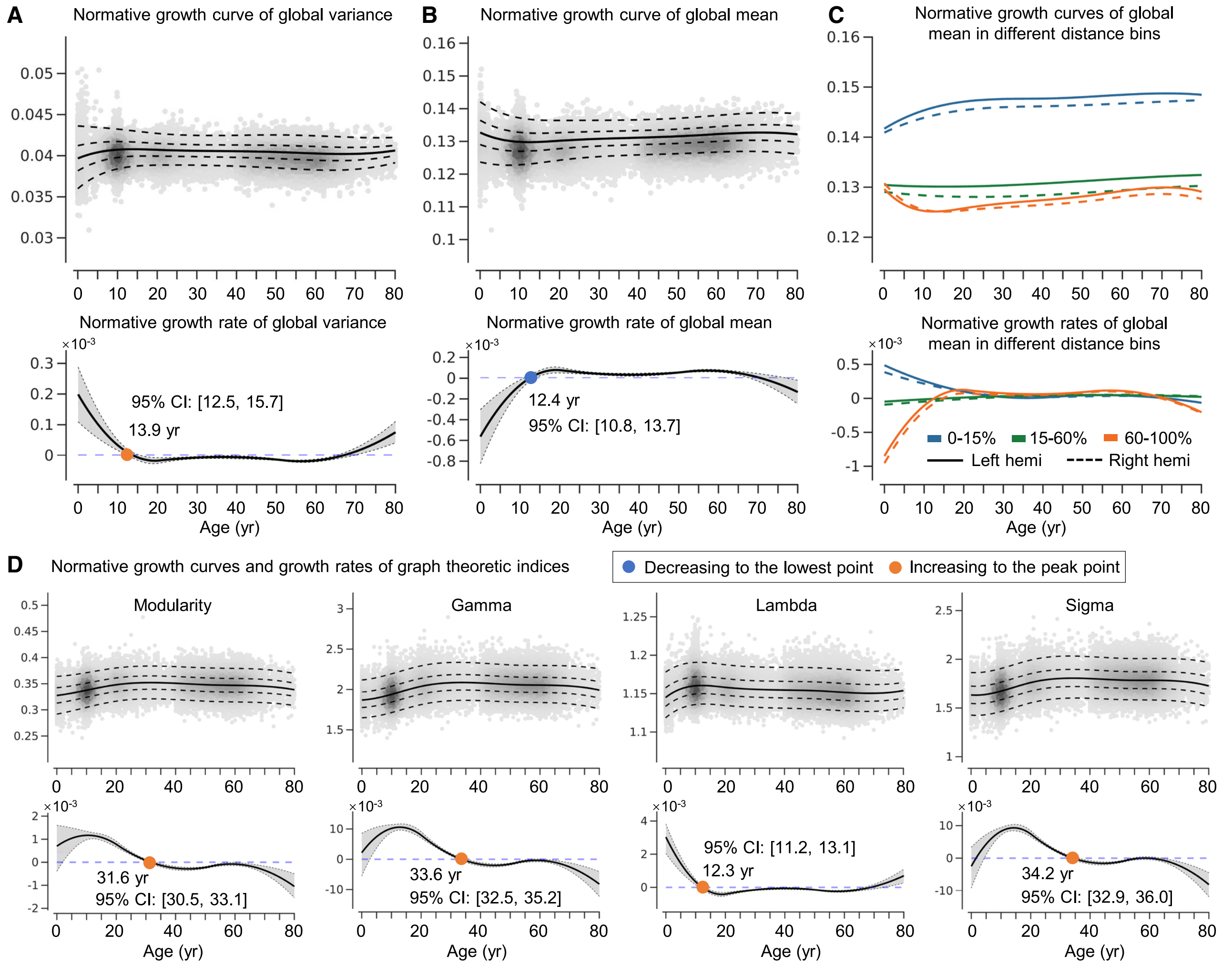

Figure 2. Normative growth of the morphometric network at the global level

(A) Normative growth curve (top) and growth rate (bottom) of the global variance of the morphometric network. The solid line (median) represents the 50% centile, and the dotted lines represent the 5%, 25%, 75%, and 95% centiles. The growth rate is assessed with the first derivative of the median line, with 95% CIs (shaded in gray) estimated by bootstrapping with 1,000 resamples.

(B) Normative growth curve and growth rate of the global mean of the morphometric network.

(C) Normative growth curve and growth rate of mean MSS across different distance bins.

(D) Normative growth curves and growth rates of modularity, Gamma, Lambda, and Sigma.

adolescence (12.4 years; 95% bootstrapped CI [10.8, 13.7]; Figure 2B). The inter-individual variability of these two global measures was greatest at the time of birth, followed by a rapid decline until adulthood (Figure S1; see STAR Methods). To examine the influence of connection distance on global growth, we divided the connections into three categories according to the inter-regional Euclidean distance: short (shortest 15%, blue), middle (15%–60%, green), and long (longest 40%, orange) (Figure 2C). The mean strength of the long-range connections exhibited a growth pattern similar to the global mean of the network. The short-range connections demonstrated the greatest strength across all three categories, with a notable increase during the first three decades of life. The middle-range connectivity strength remained relatively stable throughout the lifespan.

It is important to consider the topological refinements of the networks, which facilitate a balance between structural segregation and integration. To investigate the topological reorganization of the morphometric brain networks across the human lifespan, we binarized individual networks at 10% connection density and calculated the modularity (Q) and small-world measures (Gamma, Lambda, and Sigma). Specifically, modularity quantifies the extent to which a network is divided into discrete modules, whereas Gamma and Lambda represent the degree of local clustering (which quantifies network segregation) and characteristic path length (which quantifies network integration), respectively, relative to those for random networks. A network is considered small-world when Sigma (Gamma/Lambda) > 1. As shown in Figure 2D, both the modularity (peaking at 31.6 years; 95% bootstrapped CI [30.5, 33.1]) and Gamma (peaking at 33.6

Please cite this article in press as: Liang et al., Dissecting human cortical similarity networks across the lifespan, Neuron (2025), https://doi.org/10.1016/j.neuron.2025.06.018

years; 95% bootstrapped CI [32.5, 35.2]) values gradually increased from birth to early adulthood, which is in accordance with the lifespan growth observed for the short-range connections (Figure 2C). Lambda increased until early adolescence (peaking at 12.3 years; 95% bootstrapped CI [11.2, 13.1]), which is compatible with the lifespan growth observed for the long-range connections (Figure 2C). Finally, prominent small-world properties were observed in the morphometric brain networks across the lifespan, with all Sigma values exceeding 1.63. Nonetheless, Sigma gradually increased from birth to early adulthood, reaching a peak at 34.2 years (95% bootstrapped CI [32.9, 36.0]), followed by a slight decline (Figure 2D). Collectively, these results highlight a continuous, global optimization of network segregation and integration of the morphological connectome across the lifespan, particularly from birth to early adulthood.

Cytoarchitectonic class-level growth of morphometric brain networks across the lifespan

Prior research has indicated that morphometric similarity with MIND recapitulates the well-known cortical cytoarchitectonic classes.[20] Here, we examined whether seven cortical cytoarchitectonic classes[40] exhibit distinct lifespan growth patterns. We found that almost all intra- and inter-class connectivities presented nonlinear patterns of change across the lifespan, marked by substantial growth from birth to adolescence and partly continuing into early adulthood (Figures 3 and S2A).

Intra-class connectivity

Both the primary sensory (PS) and primary/secondary sensory (PSS) classes, which contain dense granule cells and exhibit clear laminar differentiation, presented a nonlinear decrease in morphometric similarity from birth to late childhood, suggesting increased morphometric differentiation within these classes. In contrast, the lateral frontal, parietal, and temporal association cortices (AC2), predominantly composed of pyramidal cells, presented a nonlinear increase in morphometric similarity from birth to early adolescence, whereas the paralimbic cortices, comprising the insular (IC) and limbic (LB) cortices with less-differentiated cortical layers, presented a more prolonged increase until early adulthood. The default-mode regions (AC1) presented a slight decrease in morphometric similarity from birth to early adulthood, and the primary motor (PM) exhibited a relatively stable pattern across the lifespan.

Inter-class connectivity

The sensory classes (PS and PSS) exhibited a nonlinear decrease in morphometric similarity with multiple brain classes (PM, AC1, AC2, and LB) from birth to late childhood and adolescence. In contrast, the paralimbic cortical areas (insula and cingulate) showed a nonlinear increase in morphometric similarity with multiple brain classes (PM, AC1, and AC2) from birth to adolescence.

We also showed the growth patterns of intra- and inter-class connectivity for the three distance bins (Figure S3). Moreover, the Z scores, derived by comparing each participant's intra-class and inter-class connectivity to the null distribution, revealed growth patterns that closely resembled those of the original connectivity curves (Figure S4). Collectively, the morphometric networks exhibited distinct nonlinear growth patterns with respect to cortical cytoarchitectonics, predominantly characterized by morphometric differentiation of the sensory classes (PS and PSS) and morphometric strengthening of the transmodal areas (AC1, AC2, IC, and LB) from birth to early adulthood.

Regional-level growth of morphometric brain networks across the lifespan

We further investigated the regional growth patterns of the morphometric networks. For a given region, we calculated its morphometric similarity strength (MSS) as the average morphometric similarity with all other regions. Figure 4A (top) shows the cortical maps of the fitted MSS at several representative ages. The pairwise spatial correlations among these age-specific MSS maps were calculated, followed by a hierarchical clustering analysis (Figure 4B). Four main clusters were identified: cluster I comprised MSS maps from birth to infancy (0–2 years, red), cluster II included MSS maps during early childhood (2.5–6 years, green), cluster III included MSS maps from late childhood to adolescence (8–25 years, cyan), and cluster IV comprised MSS maps in adulthood (30–80 years, purple).

The growth rate maps of regional MSS (Figure 4A, middle) revealed the most pronounced changes occurring from birth to early childhood. Specifically, the MSS exhibited a pronounced nonlinear increase in the paralimbic cortices, including the anterior cingulate cortex and IC, and a marked decrease in several sensory areas (PS and PSS). Although there were rapid increases in MSS in the paralimbic cortices during early development, these regions did not develop into network hubs over the lifespan (MSS < mean + SD) (Figure 4A, bottom). In contrast, the frontal and parietal association cortices (AC1 and AC2), which exhibited minimal changes in MSS (Figure 4A, middle), were identified as network hubs across the lifespan (MSS > mean + SD, Figures 4A, bottom, and 4C). The growth rates of the intra- and inter-class MSS were also estimated for a given region, demonstrating spatial patterns analogous to those observed for the global MSS (Figure S2B).

Finally, principal-component analysis (PCA) was performed to identify the spatial variation in regional MSS growth curves across the cortex. The first component (PC1), which accounted for 70.7% of the variance (Figure 4D, left), represents the principal growth axis of the morphometric network. The axis is anchored by sensorimotor areas (including the PS, PSS, and PM) at one end and transmodal areas (including frontal and parietal association regions and paralimbic regions) at the other. Division of the PC1 map into 20 equal bins, with the average growth rate calculated for all regions within each bin, served to further confirm the existence of distinct growth patterns between sensorimotor and transmodal regions over the human lifespan (Figure 4D, right).

Sex differences in the lifespan growth of morphometric brain networks

Understanding sex-related variations in morphometric networks is crucial for learning more about individual differences in brain development and aging. To depict sex-specific growth patterns in morphometric networks, we included sex as a covariate to estimate normative growth curves across the lifespan. Sex differences in the morphometric brain networks were observed at the global, cytoarchitectonic, and regional levels (as detailed in

Please cite this article in press as: Liang et al., Dissecting human cortical similarity networks across the lifespan, Neuron (2025), https://doi.org/10.1016/j.neuron.2025.06.018

Figure 3. Normative growth rates of the morphometric network at the cytoarchitectonic class level

A negative growth rate indicates a decrease in morphometric similarity with age and vice versa. When the growth rate changes from negative to zero, the mean morphometric similarity reaches its lowest value (blue dots). When the growth rate changes from positive to zero, the mean morphometric similarity reaches its maximum value (orange dots). The gray shading around the growth rate represents the 95% CIs.

the STAR Methods and Figure S5). Specifically, the global variance and global mean of the networks were both greater in males than in females ($p = 3.74 \times 10^{-105}$ and 5.6×10^{-39}, respectively; Figure S5A). Compared with males, females presented greater intra-class connectivity in the LB class ($p = 3.1 \times 10^{-16}$, false discovery rate [FDR] corrected) and lower intra-class connectivity in the PS, PSS, PM, AC2, and insula (all $p < 0.012$, FDR corrected). Moreover, females presented greater inter-class connectivity between the IC and all other classes and between PS areas and multiple classes (LB, AC1, and

Please cite this article in press as: Liang et al., Dissecting human cortical similarity networks across the lifespan, Neuron (2025), https://doi.org/10.1016/j.neuron.2025.06.018

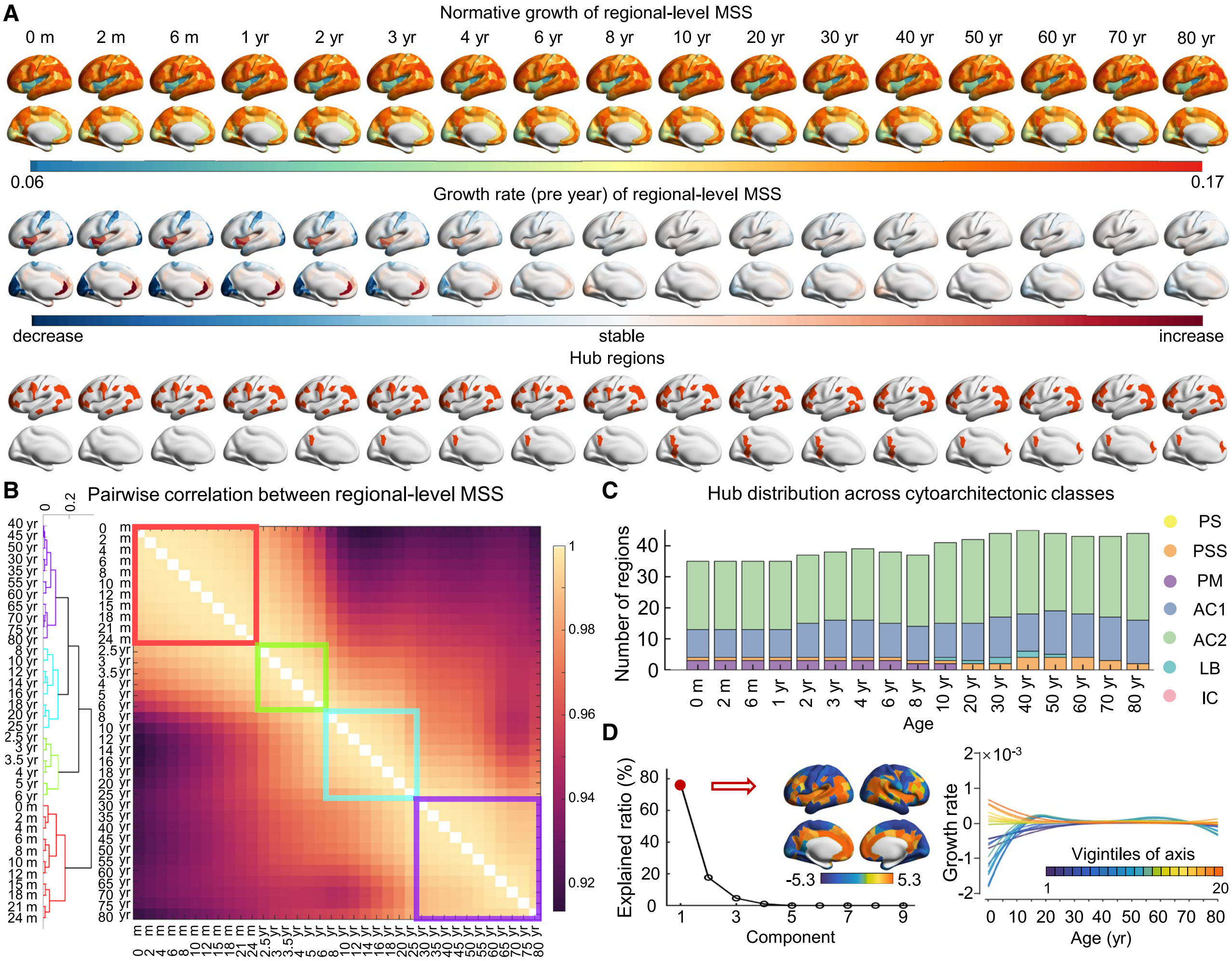

Figure 4. Normative growth of regional-level MSS

(A) Surface maps of normative growth, growth rate, and hub regions for the regional-level MSS at representative ages. The hub regions were defined as regions with MSS values exceeding the mean plus the standard error.

(B) Hierarchical clustering analysis of pairwise correlations based on regional MSS. The resulting dendrogram is partitioned into four clusters.

(C) Hub distribution across seven cytoarchitectonic classes.

(D) Explanation ratio of regional-level MSS curves derived from PCA. The first component accounts for 70.7% of the total variance, representing the lifespan dominant growth axis of morphometric similarity. We then divided the lifespan growth axis into 20 equal bins and calculated the average growth rate for all regions within each bin.

AC2) than males (all $p < 0.05$, FDR corrected; Figure S5B). In contrast, females presented smaller inter-class connectivity between the AC2 and multiple classes (PSS, PM, AC1, and LB) than males (all $p < 0.05$, FDR corrected; Figure S5B). At the regional level, we also observed widespread sex differences in MSS, with females showing greater MSS in the insula, anterior cingulate, and postcentral regions, whereas males showing greater MSS in the lateral prefrontal cortex, angular gyrus, and occipital regions ($p < 0.05$, FDR corrected; Figure S5C).

Lifespan growth patterns of morphology-function coupling

Morphometric similarity highly correlated with functional connectivity during childhood,[41] adolescence,[23,42] and adulthood,[43,44] but the lifespan changes in morphology-function coupling remain unknown. By analyzing structural MRI and task-free fMRI data from 32,887 healthy participants (aged 0–80 years), we explored morphology-function coupling changes throughout the lifespan. We first constructed the functional connectome for each participant (see STAR Methods)[34] and calculated the regional functional connectivity strength (FCS) as the total connectivity between a given region and the rest of the brain. We found that the regional FCS showed a prolonged growth trajectory from birth to early adulthood (Figure 5A), compared with the pronounced changes observed in regional MSS from birth to late childhood (Figure 4A, middle). Notably, sensory regions (e.g., PS and PSS) with a pronounced decrease in the regional MSS displayed an increase in the FCS during early

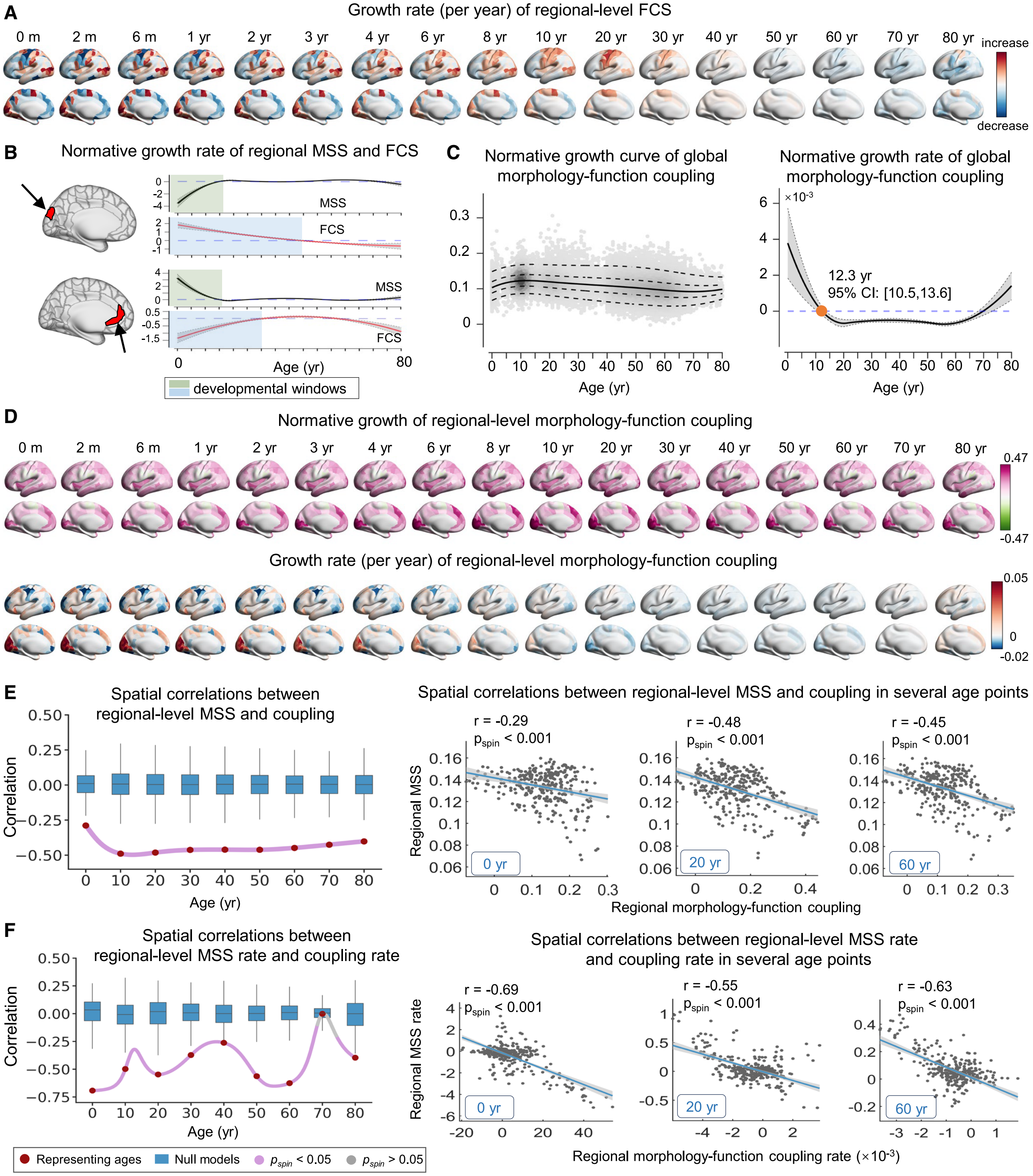

Figure 5. Normative growth of morphology-function coupling

(A) Normative growth rate of the regional FCS.

(B) Normative growth curves of regional MSS (black lines) and regional FCS (red lines) in example brain regions. The green and blue shades indicate the developmental windows for MSS and FCS, respectively.

(C) Normative growth curve and growth rate of global coupling.

(D) Surface maps of normative growth (top) and the growth rate (bottom) for regional coupling.

(legend continued on next page)

Please cite this article in press as: Liang et al., Dissecting human cortical similarity networks across the lifespan, Neuron (2025), https://doi.org/10.1016/j.neuron.2025.06.018

development (Figure 5B). Conversely, paralimbic regions (e.g., the anterior cingulate cortex) with a pronounced increase in regional MSS showed a notable decrease in FCS. These results reflect the distinct spatiotemporal growth patterns of morphometric and functional networks.

We further quantified global and regional morphology-function coupling by calculating edgewise correlations between morphometric and functional matrices and regional connectivity profile correlations, respectively (Figure 1C). Global coupling increased from birth to early adolescence (peak at 12.3 years; 95% bootstrapped CI [10.5, 13.6]) (Figure 5C), reflecting increased structural constraints on functional maturation, and then declined until late adulthood (lowest point at 69.8 years; 95% bootstrapped CI [68.0, 73.1]) (Figure 5C), indicating progressive decoupling. Regionally, several sensory areas (e.g., the visual cortex) with low MSSs (Figure 4A, top) displayed strong coupling at birth, and this degree of coupling continued to increase until early adolescence (Figure 5D). Conversely, several association areas (e.g., AC2) with high MSSs showed weak coupling across the lifespan (Figure 5D). Significant lifespan negative correlations were observed between the MSS and coupling maps (r: -0.29 to -0.50, $p_{\text{spin}} < 0.05$, FDR corrected; Figure 5E) and the corresponding growth rate maps (r: -0.10 to -0.69, $p_{\text{spin}} < 0.05$, FDR corrected; Figure 5F). These results suggest that stronger morphology-function coupling in low-level sensory areas facilitates functional specialization, whereas weaker coupling in high-order association areas enables functional flexibility.

Lifespan growth patterns of morphology-metabolism coupling

The brain network is inextricably linked to metabolism.[45,46] To gain insight into the lifespan association between the morphometric network and brain metabolism (Figure 1D), we assessed PET-based brain imaging data from 165 participants (aged 20–82 years).[35] The preprocessed data included four metabolic measures for each region, namely, aerobic glycolysis (AG), cerebral blood flow (CBF), the cerebral metabolic rate of glucose use (CMRGlc), and oxygen consumption ($CMRO_2$). Owing to the substantial challenges in obtaining PET data from early life stages, our analysis was limited to the age range of 20–80 years. We observed significant spatial correlations among metabolic measures across the lifespan ($p_{\text{spin}} < 0.05$, FDR corrected), including CMRGlc-$CMRO_2$ (r: 0.84–0.96), CMRGlc-CBF (r: 0.86–0.93), and $CMRO_2$-CBF (r: 0.91–0.96). We also observed significant AG-CMRGlc correlations before the age of 60 (r: 0.42–0.65).

For a given region, a normative growth model was first established for each metabolic measure via GAMLSS, with age treated as a smoothing term and sex as a covariate. Figure 6A shows the cortical maps of the fitted metabolic measures, illustrating region-specific metabolic decreases with age. The regional MSS maps of morphometric brain networks were then spatially correlated with each of the four metabolic maps at each corresponding age point (a total of 6,000 points, as detailed in the STAR Methods). The MSS maps showed positive correlations with the spatial maps of both the AG (r: 0.30–0.61, $p_{\text{spin}} < 0.05$, FDR corrected) and CMRGlc (r: 0.32–0.41, $p_{\text{spin}} < 0.05$, FDR corrected) throughout adulthood, whereas no significant results were observed for the other two measures (Figures 6B and 6C). These results indicate that the frontal and parietal association cortices, which presented a greater degree of morphometric similarity, as indicated by larger MSSs, tended to require a greater metabolic supply for the AG and CMRGlc.

Lifespan growth patterns of morphology-transcriptome coupling

To explore the potential biological basis of morphometric network growth, we examined their spatial relationships with the gene expression profiles obtained from the Allen Human Brain Atlas[36] (Figure 1D). Given that changes in the regional MSS growth rate were most pronounced during the first decade of life, we focused our analysis on this key developmental period. Partial least squares (PLS) regression[47] was used to relate the transcriptional profiles to the regional MSS growth rate maps (Figure 7A). The associations between gene expression and the MSS growth rate were significant from 0 to 8 years, with the first component explaining 20.8%–48.7% of the variance in the MSS growth rate maps across representative ages (all $p_{\text{spin}} < 0.05$, FDR corrected; Figure 7B). The scores of the first component were positively correlated with the Z map of the regional MSS growth rate (r: 0.46–0.70, all $p_{\text{spin}} < 0.05$, FDR corrected; Figure 7C). Gene Ontology (GO) enrichment analysis of the positively weighted genes ($Z > 5$) revealed significant enrichment in biological processes related to synaptic signaling and transmission, neuron projection development, and metabolic processes, particularly during the infancy and early childhood ($p < 0.05$, FDR corrected; Figure 7D; Table S3). Negatively weighted genes were enriched for GO biological processes, such as metal ion transport and monoatomic cation transmembrane transport ($p < 0.05$, FDR corrected; Table S3).

Clinical relevance of morphometric network-based normative models

While MRI normative models using single structural[4,48,49] or functional[50–52] features have shown potential clinical value, morphometric network-based models remain underexplored. We validated such models using AD ($N_{\text{AD}} = 180$, aged 51–80 years), MDD ($N_{\text{MDD}} = 622$, aged 11–77 years), and ASD ($N_{\text{ASD}} = 400$, aged 5–59 years)—disorders linked to network dysfunction[53] across distinct lifespan stages (Figure 1E; Table S1). For each cohort, we computed individual Z score deviations in morphometric networks at global, cytoarchitectonic class, and regional scales in patients and matched healthy controls (HCs). To avoid site-related confounders, half of the HCs ($n_{\text{HC-test}} = 649$, stratified by age, sex, and site) and all patients were included in the test set,

---

(E) Spatial correlations between the MSS and coupling maps. The scatterplots depict the MSS-coupling correlations at representative ages (0, 20, and 60 years), with a linear fit (central line in black) and a 95% CI (gray shading).

(F) Spatial correlations between the MSS rate and coupling rate maps.

For both (E) and (F), the correlation coefficients were calculated at each corresponding age point (at intervals of 0.01 years) and compared with those obtained from 1,000 spin tests. The purple dots indicate significant correlations ($p_{\text{spin}} < 0.05$, FDR corrected).

Please cite this article in press as: Liang et al., Dissecting human cortical similarity networks across the lifespan, Neuron (2025), https://doi.org/10.1016/j.neuron.2025.06.018

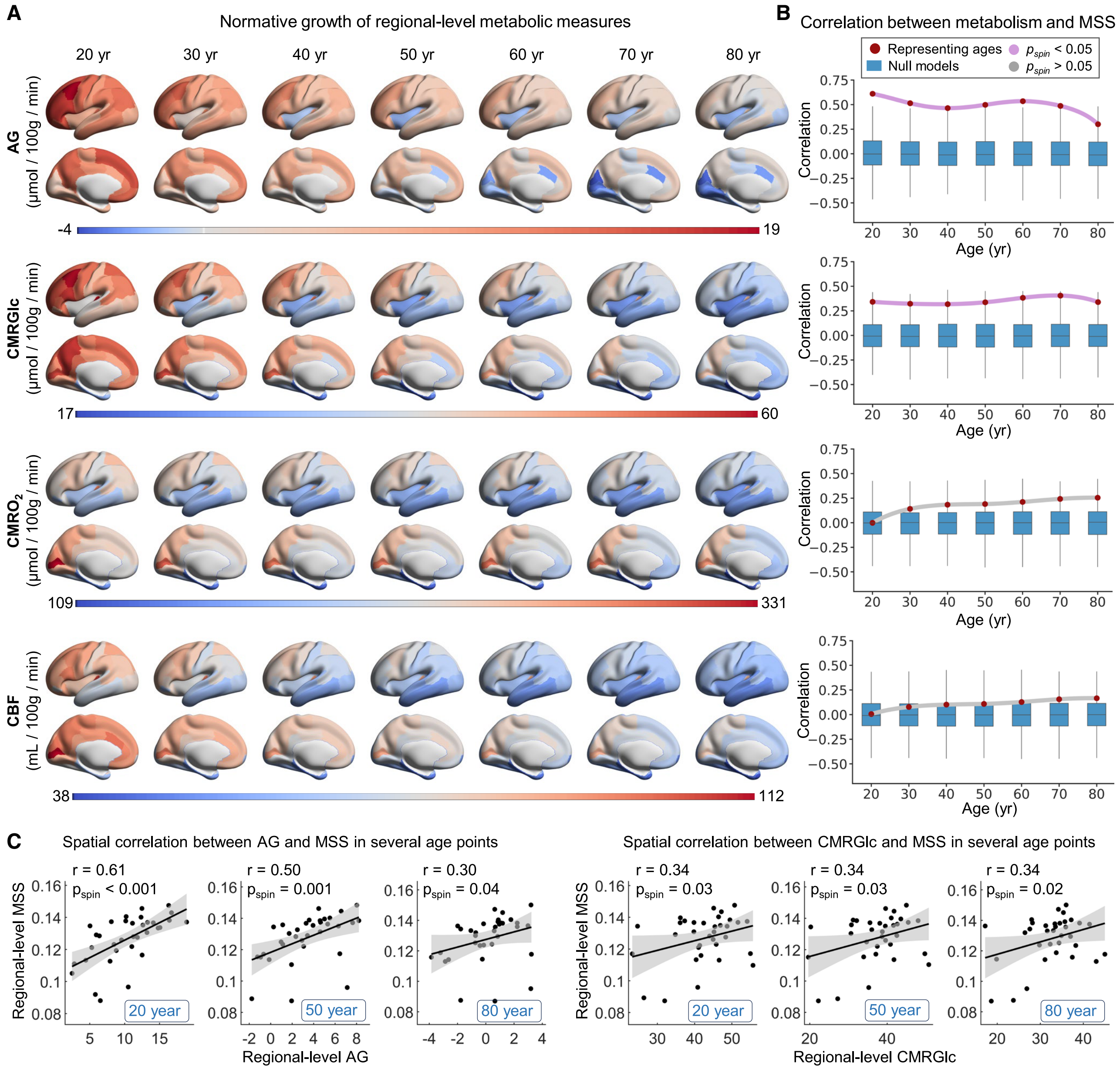

Figure 6. Normative growth of morphology-metabolism coupling

(A) Surface maps of normative growth for the regional-level AG, CMRGlc, $CMRO_2$, and CBF.

(B) Spatial correlations between the regional-level MSS maps of morphometric brain networks and regional-level metabolic maps at each corresponding age point (with intervals of 0.01 years). The observed correlations coefficients were compared with those obtained from 1,000 spin tests. The purple dots indicate significant correlations ($p_{spin} < 0.05$, FDR corrected), whereas the gray dots denote nonsignificant correlations ($p_{spin} > 0.05$, FDR-corrected).

(C) The scatterplots depict the Pearson correlation between the regional-level MSS and metabolic measures at representative ages, with a linear fit (central line in black) and a 95% CI (gray shading).

whereas the remaining 33,288 HCs (n_{train} = 33,937–$n_{HC\text{-}test}$) formed the training set for the normative models (Figure S6A). This split ensured unbiased estimation of site effects within clinical groups. This process was repeated 100 times to assess stability, yielding highly robust normative curves (mean r > 0.95) and patient deviation *Z* scores (average r > 0.95 and average mean squared error [MSE] < 0.09 for all metrics; see Figures S6B and S6C; Tables S4 and S5). For each cohort, patient deviations were averaged across 100 repetitions, with extreme deviations defined as |z| > 2.6.

Analyses revealed substantial individual heterogeneity in morphometric network deviations across disorders. In AD patients, 71% of patients showed extreme negative deviations in at least one metric, whereas 53% exhibited extreme

Please cite this article in press as: Liang et al., Dissecting human cortical similarity networks across the lifespan, Neuron (2025), https://doi.org/10.1016/j.neuron.2025.06.018

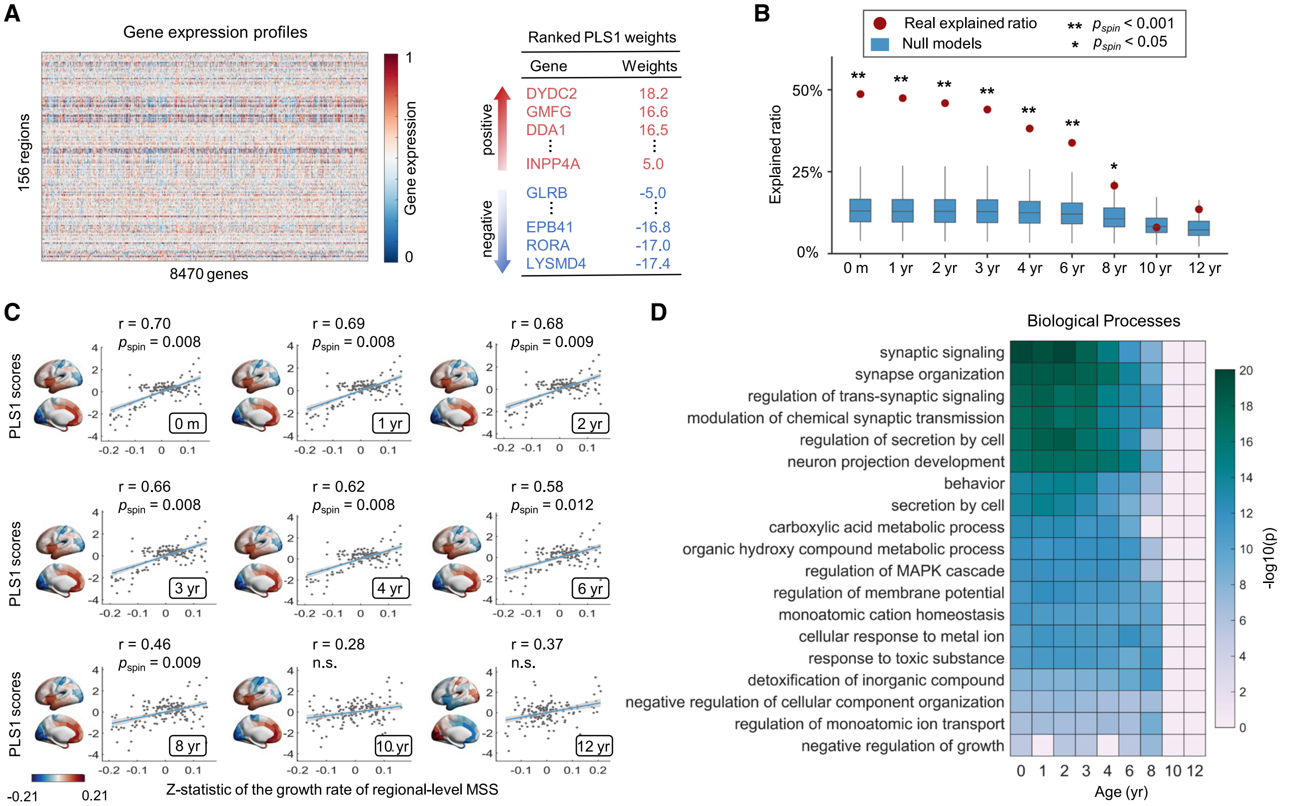

Figure 7. Normative growth of morphology-transcriptome coupling

(A) Gene expression profiles across brain nodes. We examined spatial associations between regional-level MSS growth rates and regional-level gene expression profiles using PLS regression, and we identified the top genes with positive or negative weights for the significant component.

(B) Explained ratios for the first component obtained from the PLS regression analysis. The observed explained ratios (red dots) were compared with those obtained from 1,000 null models (blue boxes).

(C) Scatterplots depicting the Pearson correlation between transcriptional profiles and the Z statistic of the growth rate of regional-level MSS at representative ages, with a linear fit (central line in black) and 95% CI (gray shading).

(D) Significant enrichment of GO biological processes was observed for the top genes with high weights (Z > 5) for the first PLS component. Here, we show the union of the 10 most significantly enriched terms identified across representative ages from 0 to 8 years.

positive deviations (Figure S6D). The corresponding rates were comparatively lower in MDD patients (32% negative and 36% positive) and ASD patients (33% negative and 24% positive) (Figure S6D). All patient groups displayed significantly more extreme deviations than the HCs (Figures 8A and 8B). Specifically, AD patients presented increased total, positive, and negative extreme deviations ($p_{FDR} < 0.05$ in 100% of repetitions), MDD patients showed similar results (total/positive/negative deviations: $p_{FDR} < 0.05$ in 100%, 98%, and 78% of the repetitions), and ASD patients presented increased total/negative deviations ($p_{FDR} < 0.05$ in 98% and 60% of repetitions, respectively) without significant positive deviations with respect to the HCs (Figure 8B). Notably, extreme deviations were highly heterogeneous across individuals: $\leq$13% of AD patients and $\leq$4% of MDD/ASD patients deviated for any single measure (Figure 8C).

Machine learning approaches based on support vector regression (SVR) linked network phenotypic deviations to clinical scores (Figure 8D). AD patients' spatial deviation patterns predicted mini-mental state examination scores ($r = 0.37$, $p_{perm} < 0.001$), while MDD deviations predicted the total Hamilton depression rating scale (HDRS) score ($r = 0.11$, $p_{perm} = 0.007$). ASD was not significantly associated with total repetitive restrictive behavior (RRB) scores ($r = 0.06$, $p_{perm} = 0.24$). These results highlight the potential clinical utility of morphometric network-based normative modeling in capturing disorder-specific heterogeneity, particularly in AD and MDD patients.

Sensitivity analyses

We validated lifespan growth patterns of the morphometric brain networks through seven sensitivity analyses as follows (see STAR Methods): (1) sample variability, bootstrapping analysis with 1,000 resamples; (2) reproducibility, using a split-half analysis; (3) site effects, using a leave-one-site-out (LOSO) analysis; (4) balanced resampling (strategy I), balancing age distribution (1,000 times); (5) balanced resampling (strategy II), balancing the participant number and site number per age group (1,000 times); (6) parcellation effects, using a 219-region atlas analysis; and (7) feature stability, using the removal of individual features. Notably, almost all network growth curves from these sensitivity analyses showed strong correlations with the primary results,

Please cite this article in press as: Liang et al., Dissecting human cortical similarity networks across the lifespan, Neuron (2025), https://doi.org/10.1016/j.neuron.2025.06.018

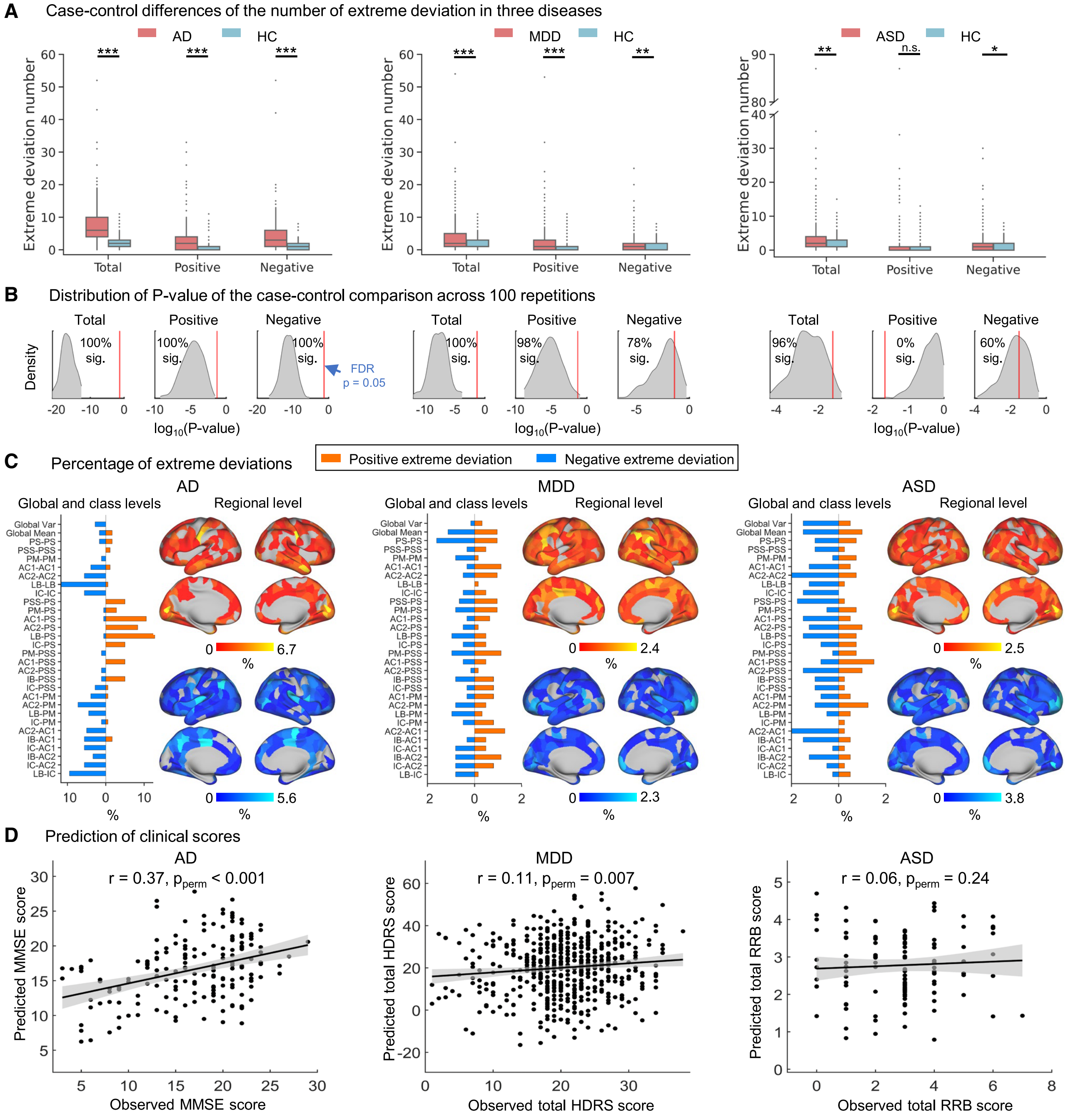

Figure 8. Clinical relevance of morphometric network-based deviations in three brain disorders

(A) Case-control differences in the extreme deviation number between HCs and patients with AD, MDD, and ASD for a single random repetition. ***$p < 0.001$, **$p < 0.01$, *$p < 0.05$.

(B) Distribution of p values for the case-control differences in the number of extreme deviations across 100 repetitions for the three brain disorders.

(C) Percentages of patients with extreme deviations at the global, class, and regional levels.

(D) Predictive accuracy for the clinical scores of the individual deviation patterns.

regardless of global, class, and regional scales (Table S6). Specifically, for sensitivity analyses (1)–(6), we observed highly consistent growth trajectories of all metrics with the primary results (r = 0.80–1.00). For sensitivity analysis (7), we also showed similar growth trajectories with the primary results across scales: global variance (r = 0.67–0.97); global mean (r = 0.91–0.97); global morphology-function coupling (r = 0.98–1.00); class-level connectivity (r = 0.89–0.98); and regional MSS (r = 0.97–1.00) and coupling (r = 0.94–1.00) maps, except for global and class-level metrics when the CT feature was removed. High spatiotemporal consistency across methodologies demonstrated that the lifespan growth patterns of morphometric networks are robust to analytical variability.

DISCUSSION

Using multimodal neuroimaging data from 33,937 healthy participants (0–80 years), we mapped the spatiotemporal trajectories of cortical morphometric networks. From birth to early adulthood, sensory cortices showed increasing morphometric differentiation, whereas paralimbic cortices (e.g., cingulate/insula) exhibited increasing morphometric similarity. These morphometric networks showed dynamic interactions with functional maturation and brain metabolism and were linked to gene expression profiles related to synaptic signaling, neurodevelopment, and metabolism processes. Normative models derived from morphometric networks captured individual heterogeneity in three brain disorders and predicted clinical outcomes. Collectively, our study establishes a normative framework of cortical morphometric networks across the human lifespan and reveals their associations with functional, metabolic, and transcriptomic profiles. This work also bridges morphology-based network modeling with clinical translation, advancing precision approaches in brain disorder research.

Using the MIND method,[20] which integrates multiple cortical features, we constructed a morphometric brain network and further investigated its lifespan growth patterns. Global network similarity declined from birth to early adolescence, whereas global variance increased, indicating increased cortical architectural diversification. Morphometric network topology was dynamically reorganized into early adulthood, paralleling prolonged functional network maturation until the fourth decade of life.[34,54] At birth, morphometric networks exhibited established modularity and small-world properties—critical for efficient information processing—which intensified until the third decade of life. These findings align with fetal morphometric network studies, which indicated that small-world topology emerges in the late second trimester and strengthens prenatally,[21] a pattern that is persistent across developmental stages such as infancy, childhood, adolescence, and adulthood.[19,27,55,56] Similarly, functional networks display a small-world topology at birth,[57,58] with a gradual increase in global system segregation over the first three decades of life.[34] This parallel optimization in morphometric and functional networks highlights the ongoing refinement of the segregation-integration balance, supporting efficient communication during development.

Sensory and paralimbic cortices exhibit opposing lifespan growth trajectories in morphometric networks. Sensory connectivity strength decreases from birth to early adolescence, whereas paralimbic connections strengthen progressively into adulthood. These findings extend previous adolescent-focused research by Dorfschmidt et al.[23] Three key factors may explain these divergent patterns. First, paralimbic regions, which serve as transitional structures between the older, simpler allocortex (e.g., three-layered hippocampus) and the six-layered neocortex,[59,60] may gradually align with neocortical organization during development, thus enhancing morphometric similarity. Second, paralimbic areas demonstrate greater plasticity than sensory areas, as characterized by lower myelination and higher synaptic density.[60] While sensory cortices complete myelination and synaptic pruning earlier,[61,62] paralimbic regions continue these processes longer,[63] amplifying developmental divergence. Third, at the macroscale, morphometric networks are organized along a principal gradient spanning from the sensory cortex to the IC.[29,64,65] This inherent organizational axis may naturally support these contrasting growth patterns. Notably, increased morphometric differentiation between isocortical and paralimbic regions during childhood is correlated with improved cognitive performance,[66] suggesting that this developmental divergence supports healthy cognition.

The intrinsic organization of the brain is closely linked to metabolic processes.[45,46] Here, we observed that morphometric connectivity strength is spatially correlated with the AG and CMRGlc. AG supports rapid ATP production[67] and synaptic plasticity[68] via nonoxidative glucose metabolism. The high-level AG is located primarily in association areas[69] that also serve as morphometric network hubs. These areas facilitate complex information integration and higher cognition,[70] aligning with prior evidence connecting high-level AG to both structural and functional network hubs.[65,69,71] Thus, morphometric networks reflect, at least in part, functional network organization. In support of our findings, global structure-function coupling gradually increases during infancy and childhood[57,72] and peaks in early adolescence before it decreases.[23,73] Early regional coupling increases in sensory areas may reflect enhanced neural synchronization and stimulus responsiveness,[72,74] whereas adolescent decoupling enables flexible dynamics for advanced cognition.[73] Notably, we found that regional MSS is negatively correlated with morphology-function coupling strength. Morphometric connectivity is often considered a proxy for monosynaptic connections between brain regions of the same cytoarchitectonic class, whereas functional connectivity is commonly used to represent polysynaptic pathways.[23] When morphometric connectivity is stronger, inter-regional information transfer may more heavily rely on direct physical connections, reducing the need for morphology-function coupling. Conversely, when morphometric connectivity is weaker, the brain may rely more heavily on complex functional integration to compensate for structural limitations, thereby increasing morphology-function coupling.

Elucidating the biological basis of morphometric brain networks is crucial for understanding their lifespan maturation dynamics. Growing evidence indicates that inter-regional morphometric similarity reflects a variety of biological properties, such as axonal connectivity, gene expression similarity, cytoarchitecture and chemoarchitecture, synchronized maturation, and experience-dependent plasticity.[8,19,20,75–78] With respect to the MIND method, the derived morphometric brain networks demonstrated striking alignment with cortical cytoarchitecture and transcriptional similarity, forming a biologically meaningful and reliable framework.[20] Despite these advances, the developmental biological basis of morphometric networks remains unclear. By integrating morphometric network growth with gene expression profiles, we provide insights into their biological underpinnings. Gene enrichment analysis revealed that early growth in terms of

Please cite this article in press as: Liang et al., Dissecting human cortical similarity networks across the lifespan, Neuron (2025), https://doi.org/10.1016/j.neuron.2025.06.018

MSS is associated with biological processes involved in synaptic signaling and transmission, neuron projection development, and metabolism. These processes are likely to contribute to morphometric network development through multiple mechanisms, including promoting axon guidance and elongation,[79] and supporting the metabolic demands of axonal growth.[80] Previous case-control research in MDD has suggested that disruption of morphometric networks is linked to similar synaptic signaling pathways.[81] These findings underscore the importance of these biological processes in regulating normative development and disease-related alterations in morphometric brain networks.

Studying the trajectories of morphometric networks across the human lifespan could unveil critical timelines for cortical organization and create a normative reference to quantify individual deviations in brain disorders. Growing evidence highlights disrupted inter-regional communication and global network dysfunction as key contributors to neuropsychiatric conditions.[82–84] By constructing lifespan growth curves, we assessed how individual connectivity metrics deviate from population norms, demonstrating the potential clinical applicability of connectome-based models. We analyzed morphometric network heterogeneity across AD, MDD, and ASD patients at the global, cytoarchitectonic, and regional levels. While $\leq$13% of patients showed extreme deviations in single metrics, neurodegenerative disorders exhibited greater overlap in morphometric network-based deviations than did psychiatric conditions. Connectome-based models showed stronger clinical symptom prediction for AD patients than MDD/ASD patients, aligning with prior findings of widespread morphometric abnormalities in AD patients[85,86] versus subtler, more heterogeneous alterations in MDD/ASD patients, with reduced detection sensitivity.[87,88] Neurodegenerative patterns' severity likely enhances network-based predictive capacity, whereas the variability of psychiatric disorders challenges morphology-focused approaches. In future work, growth charts and their derived heterogeneity metrics must be validated in clinical practice while restricting homogeneous cohorts to gain subtyping insights or expanding to larger, diverse cohorts to gain transdiagnostic insights.[4,89,90] Despite these challenges, this framework could evolve into a lifespan-based assessment tool for early diagnosis, disease monitoring, and personalized intervention.

Several limitations warrant further consideration. First, while our large cohort was ideal for performing robust analyses, an imbalanced age distribution, particularly the sparsity of data for infancy and late adulthood, may bias the growth models. Validation analyses harmonizing age/site effects partially addressed this issue, but future studies require expanded datasets targeting underrepresented age groups. Second, geographic bias persists as the data primarily originated from Europe, North America, Asia, and Australia. The inclusion of diverse populations with varied socioeconomic/cultural backgrounds would enhance generalizability. Third, the cross-sectional design could lead to the underestimation of the lifespan trajectories of morphometric brain networks.[91] Longitudinal data with a dense temporal sampling interval are needed to precisely map morphometric network maturation. Fourth, PET metabolic data were restricted to adults because of ethical/practical barriers in pediatric imaging. Lifespan PET datasets tracking metabolism, neurotransmitter receptors, and transporters could aid in better elucidating the neurobiological drivers of development. Finally, in our morphology-function coupling analysis, a morphometric correlation approach was used rather than diffusion MRI tractography[57,72]—the conventional structural network approach. While tractography struggles in cases with crossing fibers and long-range connections,[92] morphometric networks provide complementary insights into structure-function relationships. Methodological pluralism (e.g., integrating graph theory[73,74] and nonlinear dynamics[93,94]) will advance this field.

RESOURCE AVAILABILITY

Lead contact

Requests for further information and resources should be directed to and will be fulfilled by the lead contact, Yong He (yong.he@bnu.edu.cn).

Materials availability

This study did not generate new unique reagents.

Data and code availability

- All datasets used in this study are listed in the key resources table, with public availability or access upon reasonable request.
- All original code has been deposited at Zenodo at https://doi.org/10.5281/zenodo.15662487. Links to other resources are listed in the key resources table.
- Any additional information required to reanalyze the data reported in this paper is available from the lead contact upon request.

ACKNOWLEDGMENTS

This work was supported by grants from the National Natural Science Foundation of China (82021004 and 82327807 to Y. He, 824B2051 to X. Liang, and T24B2012 to L.S.), the scientific and technological innovation 2030 – the major project of the Brain Science and Brain-Inspired Intelligence Technology (2021ZD0200500 to Q.D. and 2022ZD0211500 to M.X.), the Changjiang Scholar Professorship Award (T2015027 to Y. He), the Beijing Natural Science Foundation (JQ23033 to M.X.), the National Natural Science Foundation of China (31521063 and 31221003 to Q.D.; 82071998 to M.X.; T2325006 to G. G.; 82202245 to Q. Li; 81971690 to X. Liao; 32130045 to S. Qin; 81571062 and 82172018 to Yong Liu; 81471120 to X.Z.; 61633018 to Y. Han; 81901101 to P.W.; 81400890 to D. Wang; 81920108019, 82330058, 91649117, 81771344, and 81471251 to S. Qiu; 82430063 to C.Y.; 32471096 to J.Q.; 82102131 to Y.X.; and 81425013 to W.Q.), the Beijing Brain Initiative of Beijing Municipal Science & Technology Commission (Z18110000151 8003 to S. Tao), the Fund of Shenzhen Institute for Neuroscience Research (S. Tao), the Science and Technology Plan Project of Guangzhou (2018-1002-SF-0442 to S. Qiu), the Guangzhou Key Laboratory (09002344 to S. Qiu), and the Key R&D Program of Sichuan Province (2023YFS0076 to T.C.). We are grateful to all the data contributors.

AUTHOR CONTRIBUTIONS

Conceptualization, X. Liang, L.S., and Y. He; supervision, Y. He; visualization, X. Liang and L.S.; methodology, X. Liang, L.S., M.X., T.Z., Q. Li, X. Liao, Z.C., D.D., Z.Z., Z.X., Jinhui Wang, and Y. He; data curation, X. Liang, L.S., C.P., Q. W., Q.Y., Q. Li, Y.X., R. Huo, H.Y., Ying Liu, M.X., G.G., Y.B., P.C., R.C., Y. Chen, T.C., J.C., Y. Cheng, Z.D., Y. Deng, Y. Ding, Q.D., J.-H.G., Q.G., Y. Han, Z.H., C.-C.H., R. Huang, L.L., C.-P.L., Q. Lin, B.L., C.L., N.L., Yong Liu, J.L., L.M., W.M., S. Qin, W.Q., J.Q., S. Qiu, T.S., S. Tan, Y.T., S. Tao, D. Wang, F.W., Jiali Wang, P.W., X.W., Y. Wang, D. Wei, Y. Wu, P.X., X.X., L.Y., C.Y., H.Z., X.Z., G.Z., Y.Z., and S.Z.; formal analysis, X. Liang; validation, X. Liang; writing – original draft, X. Liang, L.S., and Y. He; and all authors reviewed the final manuscript.

DECLARATION OF INTERESTS

A patent related to this work has been submitted (no. 202411715325.8). X. Liang, L.S., M.X., T.Z., and Y. He are listed as co-inventors on the application.

STAR★METHODS

Detailed methods are provided in the online version of this paper and include the following:

- KEY RESOURCES TABLE
- EXPERIMENTAL MODEL AND SUBJECT DETAILS
    - Participants
- METHOD DETAILS
    - Image quality control
    - Data processing
    - Construction of morphometric networks and functional networks
    - Morphometric similarity strength analysis
    - Graph-theory analysis
    - Lifespan associations of morphometric networks and functional networks
    - Lifespan associations between morphometric networks and brain metabolism
    - Lifespan associations between morphometric networks and gene expression profiles
    - Clinical relevance of morphometric network-based normative models in brain disorders
- QUANTIFICATION AND STATISTICAL ANALYSIS
    - Statistical analysis
    - Normative growth modeling of the morphometric brain network
    - Sensitivity analysis of the normative models
- ADDITIONAL RESOURCES

SUPPLEMENTAL INFORMATION

Supplemental information can be found online at https://doi.org/10.1016/j.neuron.2025.06.018.

Received: January 8, 2025
Revised: April 13, 2025
Accepted: June 25, 2025

REFERENCES

1. Rakic, P. (2009). Evolution of the neocortex: a perspective from developmental biology. Nat. Rev. Neurosci. *10*, 724–735. https://doi.org/10.1038/nrn2719.
2. van der Meer, D., and Kaufmann, T. (2022). Mapping the genetic architecture of cortical morphology through neuroimaging: progress and perspectives. Transl. Psychiatry *12*, 447. https://doi.org/10.1038/s41398-022-02193-5.
3. van der Meer, D., Kaufmann, T., Shadrin, A.A., Makowski, C., Frei, O., Roelfs, D., Monereo-Sánchez, J., Linden, D.E.J., Rokicki, J., Alnæs, D., et al. (2021). The genetic architecture of human cortical folding. Sci. Adv. *7*, eabj9446. https://doi.org/10.1126/sciadv.abj9446.
4. Bethlehem, R.A.I., Seidlitz, J., White, S.R., Vogel, J.W., Anderson, K.M., Adamson, C., Adler, S., Alexopoulos, G.S., Anagnostou, E., Areces-Gonzalez, A., et al. (2022). Brain charts for the human lifespan. Nature *604*, 525–533. https://doi.org/10.1038/s41586-022-04554-y.
5. Frangou, S., Modabbernia, A., Williams, S.C.R., Papachristou, E., Doucet, G.E., Agartz, I., Aghajani, M., Akudjedu, T.N., Albajes-Eizagirre, A., Alnæs, D., et al. (2022). Cortical thickness across the lifespan: Data from 17,075 healthy individuals aged 3–90 years. Hum. Brain Mapp. *43*, 431–451. https://doi.org/10.1002/hbm.25364.
6. Brouwer, R.M., Klein, M., Grasby, K.L., Schnack, H.G., Jahanshad, N., Teeuw, J., Thomopoulos, S.I., Sprooten, E., Franz, C.E., Gogtay, N., et al. (2022). Genetic variants associated with longitudinal changes in brain structure across the lifespan. Nat. Neurosci. *25*, 421–432. https://doi.org/10.1038/s41593-022-01042-4.
7. Grasby, K.L., Jahanshad, N., Painter, J.N., Colodro-Conde, L., Bralten, J., Hibar, D.P., Lind, P.A., Pizzagalli, F., Ching, C.R.K., McMahon, M.A. B., et al. (2020). The genetic architecture of the human cerebral cortex. Science *367*, eaay6690. https://doi.org/10.1126/science.aay6690.
8. Alexander-Bloch, A., Giedd, J.N., and Bullmore, E. (2013). Imaging structural co-variance between human brain regions. Nat. Rev. Neurosci. *14*, 322–336. https://doi.org/10.1038/nrn3465.
9. Wang, J., and He, Y. (2024). Toward individualized connectomes of brain morphology. Trends Neurosci. *47*, 106–119. https://doi.org/10.1016/j.tins.2023.11.011.
10. Sebenius, I., Dorfschmidt, L., Seidlitz, J., Alexander-Bloch, A., Morgan, S.E., and Bullmore, E. (2025). Structural MRI of brain similarity networks. Nat. Rev. Neurosci. *26*, 42–59. https://doi.org/10.1038/s41583-024-00882-2.
11. Barbas, H., and Rempel-Clower, N. (1997). Cortical structure predicts the pattern of corticocortical connections. Cereb. Cortex *7*, 635–646. https://doi.org/10.1093/cercor/7.7.635.
12. Bazinet, V., Hansen, J.Y., and Misic, B. (2023). Towards a biologically annotated brain connectome. Nat. Rev. Neurosci. *24*, 747–760. https://doi.org/10.1038/s41583-023-00752-3.
13. Pathak, A., Chatterjee, N., and Sinha, S. (2020). Developmental trajectory of Caenorhabditis elegans nervous system governs its structural organization. PLoS Comp. Biol. *16*, e1007602. https://doi.org/10.1371/journal.pcbi.1007602.
14. Jin, S., Li, J., and Wang, J. (2025). Brain connectome from neuronal morphology. Netw. Neurosci. 1–25. https://doi.org/10.1162/netn_a_00458.
15. Beul, S.F., Barbas, H., and Hilgetag, C.C. (2017). A predictive structural model of the primate connectome. Sci. Rep. *7*, 43176. https://doi.org/10.1038/srep43176.
16. Beul, S.F., Grant, S., and Hilgetag, C.C. (2015). A predictive model of the cat cortical connectome based on cytoarchitecture and distance. Brain Struct. Funct. *220*, 3167–3184. https://doi.org/10.1007/s00429-014-0849-y.
17. Hilgetag, C.C., Beul, S.F., van Albada, S.J., and Goulas, A. (2019). An architectonic type principle integrates macroscopic cortico-cortical connections with intrinsic cortical circuits of the primate brain. Netw. Neurosci. *3*, 905–923. https://doi.org/10.1162/netn_a_00100.
18. Hilgetag, C.C., and Amunts, K. (2016). Connectivity and cortical architecture. e-Neuroforum *22*, 56–63. https://doi.org/10.1515/s13295-016-0028-0.
19. Seidlitz, J., Váša, F., Shinn, M., Romero-Garcia, R., Whitaker, K.J., Vértes, P.E., Wagstyl, K., Kirkpatrick Reardon, P., Clasen, L., Liu, S., et al. (2018). Morphometric Similarity Networks Detect Microscale Cortical Organization and Predict Inter-Individual Cognitive Variation. Neuron *97*, 231–247.e7. https://doi.org/10.1016/j.neuron.2017.11.039.
20. Sebenius, I., Seidlitz, J., Warrier, V., Bethlehem, R.A.I., Alexander-Bloch, A., Mallard, T.T., Garcia, R.R., Bullmore, E.T., and Morgan, S.E. (2023). Robust estimation of cortical similarity networks from brain MRI. Nat. Neurosci. *26*, 1461–1471. https://doi.org/10.1038/s41593-023-01376-7.
21. Zhao, R., Sun, C., Xu, X., Zhao, Z., Li, M., Chen, R., Shen, Y., Pan, Y., Zhang, S., Wang, G., and Wu, D. (2023). Developmental pattern of individual morphometric similarity network in the human fetal brain. NeuroImage *283*, 120410. https://doi.org/10.1016/j.neuroimage.2023.120410.
22. Fenchel, D., Dimitrova, R., Seidlitz, J., Robinson, E.C., Batalle, D., Hutter, J., Christiaens, D., Pietsch, M., Brandon, J., Hughes, E.J., et al. (2020). Development of microstructural and morphological cortical profiles in the neonatal brain. Cereb. Cortex *30*, 5767–5779. https://doi.org/10.1093/cercor/bhaa150.

23. Dorfschmidt, L., Váša, F., White, S.R., Romero-García, R., Kitzbichler, M.G., Alexander-Bloch, A., Cieslak, M., Mehta, K., Satterthwaite, T.D., et al.; NSPN Consortium (2024). Human adolescent brain similarity development is different for paralimbic versus neocortical zones. Proc. Natl. Acad. Sci. USA *121*, e2314074121. https://doi.org/10.1073/pnas.2314074121.
24. Vijayakumar, N., Ball, G., Seal, M.L., Mundy, L., Whittle, S., and Silk, T. (2021). The development of structural covariance networks during the transition from childhood to adolescence. Sci. Rep. *11*, 9451. https://doi.org/10.1038/s41598-021-88918-w.
25. Váša, F., Seidlitz, J., Romero-Garcia, R., Whitaker, K.J., Rosenthal, G., Vértes, P.E., Shinn, M., Alexander-Bloch, A., Fonagy, P., Dolan, R.J., et al. (2018). Adolescent tuning of association cortex in human structural brain networks. Cereb. Cortex *28*, 281–294. https://doi.org/10.1093/cercor/bhx249.
26. Ruan, J., Wang, N., Li, J., Wang, J., Zou, Q., Lv, Y., Zhang, H., and Wang, J. (2023). Single-subject cortical morphological brain networks across the adult lifespan. Hum. Brain Mapp. *44*, 5429–5449. https://doi.org/10.1002/hbm.26450.
27. Shigemoto, Y., Sato, N., Maikusa, N., Sone, D., Ota, M., Kimura, Y., Chiba, E., Okita, K., Yamao, T., Nakaya, M., et al. (2023). Age and sex-related effects on single-subject gray matter networks in healthy participants. J. Pers. Med. *13*, 419. https://doi.org/10.3390/jpm13030419.
28. Wang, Y., Zhang, Y., Zheng, W., Liu, X., Zhao, Z., Li, S., Chen, N., Yang, L., Fang, L., Yao, Z., and Hu, B. (2023). Age-related differences of cortical topology across the adult lifespan: Evidence from a multisite MRI study with 1427 individuals. J. Magn. Reson. Imaging *57*, 434–443. https://doi.org/10.1002/jmri.28318.
29. Li, J., Zhang, C., Meng, Y., Yang, S., Xia, J., Chen, H., and Liao, W. (2024). Morphometric brain organization across the human lifespan reveals increased dispersion linked to cognitive performance. PLoS Biol. *22*, e3002647. https://doi.org/10.1371/journal.pbio.3002647.
30. Li, J., Wang, Q., Li, K., Yao, L., and Guo, X. (2024). Tracking Age-Related Topological Changes in Individual Brain Morphological Networks Across the Human Lifespan. J. Magn. Reson. Imaging *59*, 1841–1851. https://doi.org/10.1002/jmri.28984.
31. Fotiadis, P., Parkes, L., Davis, K.A., Satterthwaite, T.D., Shinohara, R.T., and Bassett, D.S. (2024). Structure–function coupling in macroscale human brain networks. Nat. Rev. Neurosci. *25*, 688–704. https://doi.org/10.1038/s41583-024-00846-6.
32. Suárez, L.E., Markello, R.D., Betzel, R.F., and Misic, B. (2020). Linking structure and function in macroscale brain networks. Trends Cogn. Sci. *24*, 302–315. https://doi.org/10.1016/j.tics.2020.01.008.
33. Rutherford, S., Fraza, C., Dinga, R., Kia, S.M., Wolfers, T., Zabihi, M., Berthet, P., Worker, A., Verdi, S., Andrews, D., et al. (2022). Charting brain growth and aging at high spatial precision. eLife *11*, e72904. https://doi.org/10.7554/eLife.72904.
34. Sun, L., Zhao, T., Liang, X., Xia, M., Li, Q., Liao, X., Gong, G., Wang, Q., Pang, C., Yu, Q., et al. (2025). Human lifespan changes in the brain's functional connectome. Nat. Neurosci. *28*, 891–901. https://doi.org/10.1038/s41593-025-01907-4.
35. Goyal, M.S., Vlassenko, A.G., Blazey, T.M., Su, Y., Couture, L.E., Durbin, T.J., Bateman, R.J., Benzinger, T.L.-S., Morris, J.C., and Raichle, M.E. (2017). Loss of brain aerobic glycolysis in normal human aging. Cell Metab. *26*, 353–360.e3. https://doi.org/10.1016/j.cmet.2017.07.010.
36. Hawrylycz, M.J., Lein, E.S., Guillozet-Bongaarts, A.L., Shen, E.H., Ng, L., Miller, J.A., van de Lagemaat, L.N., Smith, K.A., Ebbert, A., Riley, Z.L., et al. (2012). An anatomically comprehensive atlas of the adult human brain transcriptome. Nature *489*, 391–399. https://doi.org/10.1038/nature11405.
37. Romero-Garcia, R., Atienza, M., Clemmensen, L.H., and Cantero, J.L. (2012). Effects of network resolution on topological properties of human neocortex. NeuroImage *59*, 3522–3532. https://doi.org/10.1016/j.neuroimage.2011.10.086.
38. Borghi, E., de Onis, M., Garza, C., Van den Broeck, J., Frongillo, E.A., Grummer-Strawn, L., Van Buuren, S., Pan, H., Molinari, L., Martorell, R., et al. (2006). Construction of the World Health Organization child growth standards: selection of methods for attained growth curves. Stat. Med. *25*, 247–265. https://doi.org/10.1002/sim.2227.
39. Stasinopoulos, D.M., and Rigby, R.A. (2007). Generalized additive models for location scale and shape (GAMLSS) in R. J. Stat. Softw. *23*, 1–46. https://doi.org/10.18637/jss.v023.i07.
40. von Economo, C.F., and Koskinas, G.N. (1926). Die Cytoarchitektonik der Hirnrinde des erwachsenen Menschen. (The Cyto-Architectonics of the Cerebral Cortex of Adult Man.). Arch. Neurol. Psychiatry *16*, 816. https://doi.org/10.1001/archneurpsyc.1926.02200300136013.
41. Geng, X., Li, G., Lu, Z., Gao, W., Wang, L., Shen, D., Zhu, H., and Gilmore, J.H. (2017). Structural and maturational covariance in early childhood brain development. Cereb. Cortex *27*, 1795–1807. https://doi.org/10.1093/cercor/bhw022.
42. Alexander-Bloch, A., Raznahan, A., Bullmore, E., and Giedd, J. (2013). The convergence of maturational change and structural covariance in human cortical networks. J. Neurosci. *33*, 2889–2899. https://doi.org/10.1523/JNEUROSCI.3554-12.2013.
43. Luo, N., Sui, J., Abrol, A., Chen, J., Turner, J.A., Damaraju, E., Fu, Z., Fan, L., Lin, D., Zhuo, C., et al. (2020). Structural brain architectures match intrinsic functional networks and vary across domains: a study from 15 000+ individuals. Cereb. Cortex *30*, 5460–5470. https://doi.org/10.1093/cercor/bhaa127.
44. Chen, Z.J., He, Y., Rosa-Neto, P., Gong, G., and Evans, A.C. (2011). Age-related alterations in the modular organization of structural cortical network by using cortical thickness from MRI. NeuroImage *56*, 235–245. https://doi.org/10.1016/j.neuroimage.2011.01.010.
45. Chen, Y., Lin, Q., Liao, X., Zhou, C., and He, Y. (2021). Association of aerobic glycolysis with the structural connectome reveals a benefit–risk balancing mechanism in the human brain. Proc. Natl. Acad. Sci. USA *118*, e2013232118. https://doi.org/10.1073/pnas.2013232118.
46. Liang, X., Zou, Q., He, Y., and Yang, Y. (2013). Coupling of functional connectivity and regional cerebral blood flow reveals a physiological basis for network hubs of the human brain. Proc. Natl. Acad. Sci. USA *110*, 1929–1934. https://doi.org/10.1073/pnas.1214900110.
47. Abdi, H. (2010). Partial least squares regression and projection on latent structure regression (PLS Regression). WIREs Comp. Stat. *2*, 97–106. https://doi.org/10.1002/wics.51.
48. Rutherford, S., Kia, S.M., Wolfers, T., Fraza, C., Zabihi, M., Dinga, R., Berthet, P., Worker, A., Verdi, S., Ruhe, H.G., et al. (2022). The normative modeling framework for computational psychiatry. Nat. Protoc. *17*, 1711–1734. https://doi.org/10.1038/s41596-022-00696-5.
49. Segal, A., Parkes, L., Aquino, K., Kia, S.M., Wolfers, T., Franke, B., Hoogman, M., Beckmann, C.F., Westlye, L.T., Andreassen, O.A., et al. (2023). Regional, circuit and network heterogeneity of brain abnormalities in psychiatric disorders. Nat. Neurosci. *26*, 1613–1629. https://doi.org/10.1038/s41593-023-01404-6.
50. Marquand, A.F., Rezek, I., Buitelaar, J., and Beckmann, C.F. (2016). Understanding heterogeneity in clinical cohorts using normative models: beyond case-control studies. Biol. Psychiatry *80*, 552–561. https://doi.org/10.1016/j.biopsych.2015.12.023.
51. Sun, X., Sun, J., Lu, X., Dong, Q., Zhang, L., Wang, W., Liu, J., Ma, Q., Wang, X., Wei, D., et al. (2023). Mapping neurophysiological subtypes of major depressive disorder using normative models of the functional connectome. Biol. Psychiatry *94*, 936–947. https://doi.org/10.1016/j.biopsych.2023.05.021.
52. Rutherford, S., Barkema, P., Tso, I.F., Sripada, C., Beckmann, C.F., Ruhe, H.G., and Marquand, A.F. (2023). Evidence for embracing normative modeling. eLife *12*, e85082. https://doi.org/10.7554/eLife.85082.

53. van den Heuvel, M.P., and Sporns, O. (2019). A cross-disorder connectome landscape of brain dysconnectivity. Nat. Rev. Neurosci. *20*, 435–446. https://doi.org/10.1038/s41583-019-0177-6.

54. Cao, M., Huang, H., and He, Y. (2017). Developmental connectomics from infancy through early childhood. Trends Neurosci. *40*, 494–506. https://doi.org/10.1016/j.tins.2017.06.003.

55. Fan, Y., Shi, F., Smith, J.K., Lin, W., Gilmore, J.H., and Shen, D. (2011). Brain anatomical networks in early human brain development. NeuroImage *54*, 1862–1871. https://doi.org/10.1016/j.neuroimage.2010.07.025.

56. Khundrakpam, B.S., Reid, A., Brauer, J., Carbonell, F., Lewis, J., Ameis, S., Karama, S., Lee, J., Chen, Z., Das, S., et al. (2013). Developmental changes in organization of structural brain networks. Cereb. Cortex *23*, 2072–2085. https://doi.org/10.1093/cercor/bhs187.

57. Van Den Heuvel, M.P., Kersbergen, K.J., De Reus, M.A., Keunen, K., Kahn, R.S., Groenendaal, F., De Vries, L.S., and Benders, M.J.N.L. (2015). The neonatal connectome during preterm brain development. Cereb. Cortex *25*, 3000–3013. https://doi.org/10.1093/cercor/bhu095.

58. Cao, M., He, Y., Dai, Z., Liao, X., Jeon, T., Ouyang, M., Chalak, L., Bi, Y., Rollins, N., Dong, Q., and Huang, H. (2017). Early development of functional network segregation revealed by connectomic analysis of the preterm human brain. Cereb. Cortex *27*, 1949–1963. https://doi.org/10.1093/cercor/bhw038.

59. Ramachandran, V.S. (2002). Encyclopedia of the Human Brain (Elsevier).

60. García-Cabezas, M.Á., Zikopoulos, B., and Barbas, H. (2019). The Structural Model: a theory linking connections, plasticity, pathology, development and evolution of the cerebral cortex. Brain Struct. Funct. *224*, 985–1008. https://doi.org/10.1007/s00429-019-01841-9.

61. Huttenlocher, P.R., and Dabholkar, A.S. (1997). Regional differences in synaptogenesis in human cerebral cortex. J. Comp. Neurol. *387*, 167–178. https://doi.org/10.1002/(SICI)1096-9861(19971020)387:2<167::AID-CNE1>3.0.CO;2-Z.

62. Sowell, E.R., Peterson, B.S., Thompson, P.M., Welcome, S.E., Henkenius, A.L., and Toga, A.W. (2003). Mapping cortical change across the human life span. Nat. Neurosci. *6*, 309–315. https://doi.org/10.1038/nn1008.

63. Baum, G.L., Flournoy, J.C., Glasser, M.F., Harms, M.P., Mair, P., Sanders, A.F.P., Barch, D.M., Buckner, R.L., Bookheimer, S., Dapretto, M., et al. (2022). Graded variation in T1w/T2w ratio during adolescence: measurement, caveats, and implications for development of cortical myelin. J. Neurosci. *42*, 5681–5694. https://doi.org/10.1523/JNEUROSCI.2380-21.2022.

64. Yang, S., Wagstyl, K., Meng, Y., Zhao, X., Li, J., Zhong, P., Li, B., Fan, Y.-S., Chen, H., and Liao, W. (2021). Cortical patterning of morphometric similarity gradient reveals diverged hierarchical organization in sensory-motor cortices. Cell Rep. *36*, 109582. https://doi.org/10.1016/j.celrep.2021.109582.

65. Bullmore, E., and Sporns, O. (2012). The economy of brain network organization. Nat. Rev. Neurosci. *13*, 336–349. https://doi.org/10.1038/nrn3214.

66. Wu, X., Palaniyappan, L., Yu, G., Zhang, K., Seidlitz, J., Liu, Z., Kong, X., Schumann, G., Feng, J., Sahakian, B.J., et al. (2023). Morphometric dissimilarity between cortical and subcortical areas underlies cognitive function and psychiatric symptomatology: a preadolescence study from ABCD. Mol. Psychiatry *28*, 1146–1158. https://doi.org/10.1038/s41380-022-01896-x.

67. Fünfschilling, U., Supplie, L.M., Mahad, D., Boretius, S., Saab, A.S., Edgar, J., Brinkmann, B.G., Kassmann, C.M., Tzvetanova, I.D., Möbius, W., et al. (2012). Glycolytic oligodendrocytes maintain myelin and long-term axonal integrity. Nature *485*, 517–521. https://doi.org/10.1038/nature11007.

68. Goyal, M.S., Hawrylycz, M., Miller, J.A., Snyder, A.Z., and Raichle, M.E. (2014). Aerobic glycolysis in the human brain is associated with development and neotenous gene expression. Cell Metab. *19*, 49–57. https://doi.org/10.1016/j.cmet.2013.11.020.

69. Vaishnavi, S.N., Vlassenko, A.G., Rundle, M.M., Snyder, A.Z., Mintun, M.A., and Raichle, M.E. (2010). Regional aerobic glycolysis in the human brain. Proc. Natl. Acad. Sci. USA *107*, 17757–17762. https://doi.org/10.1073/pnas.1010459107.

70. Yeo, B.T.T., Krienen, F.M., Eickhoff, S.B., Yaakub, S.N., Fox, P.T., Buckner, R.L., Asplund, C.L., and Chee, M.W.L. (2015). Functional specialization and flexibility in human association cortex. Cereb. Cortex *25*, 3654–3672. https://doi.org/10.1093/cercor/bhu217.

71. Vlassenko, A.G., and Raichle, M.E. (2015). Brain aerobic glycolysis functions and Alzheimer's disease. Clin. Transl. Imaging *3*, 27–37. https://doi.org/10.1007/s40336-014-0094-7.

72. Hagmann, P., Sporns, O., Madan, N., Cammoun, L., Pienaar, R., Wedeen, V.J., Meuli, R., Thiran, J.P., and Grant, P.E. (2010). White matter maturation reshapes structural connectivity in the late developing human brain. Proc. Natl. Acad. Sci. USA *107*, 19067–19072. https://doi.org/10.1073/pnas.1009073107.

73. Zamani Esfahlani, F., Faskowitz, J., Slack, J., Mišić, B., and Betzel, R.F. (2022). Local structure-function relationships in human brain networks across the lifespan. Nat. Commun. *13*, 2053. https://doi.org/10.1038/s41467-022-29770-y.

74. Baum, G.L., Cui, Z., Roalf, D.R., Ciric, R., Betzel, R.F., Larsen, B., Cieslak, M., Cook, P.A., Xia, C.H., Moore, T.M., et al. (2020). Development of structure–function coupling in human brain networks during youth. Proc. Natl. Acad. Sci. USA *117*, 771–778. https://doi.org/10.1073/pnas.1912034117.

75. Li, Z., Li, J., Wang, N., Lv, Y., Zou, Q., and Wang, J. (2023). Single-subject cortical morphological brain networks: phenotypic associations and neurobiological substrates. NeuroImage *283*, 120434. https://doi.org/10.1016/j.neuroimage.2023.120434.

76. Mechelli, A., Crinion, J.T., Noppeney, U., O'Doherty, J., Ashburner, J., Frackowiak, R.S., and Price, C.J. (2004). Neurolinguistics: structural plasticity in the bilingual brain. Nature *431*, 757. https://doi.org/10.1038/431757a.

77. Maguire, E.A., Gadian, D.G., Johnsrude, I.S., Good, C.D., Ashburner, J., Frackowiak, R.S., and Frith, C.D. (2000). Navigation-related structural change in the hippocampi of taxi drivers. Proc. Natl. Acad. Sci. USA *97*, 4398–4403. https://doi.org/10.1073/pnas.070039597.

78. Draganski, B., Gaser, C., Busch, V., Schuierer, G., Bogdahn, U., and May, A. (2004). Neuroplasticity: Changes in grey matter induced by training. Nature *427*, 311–312. https://doi.org/10.1038/427311a.

79. Vanderhaeghen, P., and Cheng, H.-J. (2010). Guidance molecules in axon pruning and cell death. Cold Spring Harbor Perspect. Biol. *2*, a001859. https://doi.org/10.1101/cshperspect.a001859.

80. Chamberlain, K.A., and Sheng, Z.H. (2019). Mechanisms for the maintenance and regulation of axonal energy supply. J. Neurosci. Res. *97*, 897–913. https://doi.org/10.1002/jnr.24411.

81. Li, J., Seidlitz, J., Suckling, J., Fan, F., Ji, G.-J., Meng, Y., Yang, S., Wang, K., Qiu, J., Chen, H., and Liao, W. (2021). Cortical structural differences in major depressive disorder correlate with cell type-specific transcriptional signatures. Nat. Commun. *12*, 1647. https://doi.org/10.1038/s41467-021-21943-5.

82. Gong, Q., and He, Y. (2015). Depression, Neuroimaging and Connectomics: A Selective Overview. Biol. Psychiatry *77*, 223–235. https://doi.org/10.1016/j.biopsych.2014.08.009.

83. Fornito, A., Zalesky, A., and Breakspear, M. (2015). The connectomics of brain disorders. Nat. Rev. Neurosci. *16*, 159–172. https://doi.org/10.1038/nrn3901.

84. Perovnik, M., Rus, T., Schindlbeck, K.A., and Eidelberg, D. (2023). Functional brain networks in the evaluation of patients with neurodegenerative disorders. Nat. Rev. Neurol. *19*, 73–90. https://doi.org/10.1038/s41582-022-00753-3.

85. Young, P.N.E., Estarellas, M., Coomans, E., Srikrishna, M., Beaumont, H., Maass, A., Venkataraman, A.V., Lissaman, R., Jiménez, D., Betts, M.J., et al. (2020). Imaging biomarkers in neurodegeneration: current and future practices. Alzheimers Res. Ther. *12*, 49. https://doi.org/10.1186/s13195-020-00612-7.

86. Pini, L., Pievani, M., Bocchetta, M., Altomare, D., Bosco, P., Cavedo, E., Galluzzi, S., Marizzoni, M., and Frisoni, G.B. (2016). Brain atrophy in Alzheimer's disease and aging. Ageing Res. Rev. *30*, 25–48. https://doi.org/10.1016/j.arr.2016.01.002.

87. Schmaal, L., Hibar, D.P., Sämann, P.G., Hall, G.B., Baune, B.T., Jahanshad, N., Cheung, J.W., van Erp, T.G.M., Bos, D., Ikram, M.A., et al. (2017). Cortical abnormalities in adults and adolescents with major depression based on brain scans from 20 cohorts worldwide in the ENIGMA Major Depressive Disorder Working Group. Mol. Psychiatry *22*, 900–909. https://doi.org/10.1038/mp.2016.60.

88. van Rooij, D., Anagnostou, E., Arango, C., Auzias, G., Behrmann, M., Busatto, G.F., Calderoni, S., Daly, E., Deruelle, C., Di Martino, A., et al. (2018). Cortical and subcortical brain morphometry differences between patients with autism spectrum disorder and healthy individuals across the lifespan: results from the ENIGMA ASD Working Group. Am. J. Psychiatry *175*, 359–369. https://doi.org/10.1176/appi.ajp.2017.17010100.

89. Bedford, S.A., Seidlitz, J., and Bethlehem, R.A.I. (2022). Translational potential of human brain charts. Clin. Transl. Med. *12*, e960. https://doi.org/10.1002/ctm2.960.

90. Zhou, Z.-X., Chen, L.-Z., Milham, M.P., and Zuo, X.-N.; Lifespan Brain Chart Consortium (LBCC) (2023). Six cornerstones for translational brain charts. Sci. Bull. *68*, 795–799. https://doi.org/10.1016/j.scib.2023.03.047.

91. Di Biase, M.A., Tian, Y.E., Bethlehem, R.A.I., Seidlitz, J., Alexander-Bloch, A.F., Yeo, B.T.T., and Zalesky, A. (2023). Mapping human brain charts cross-sectionally and longitudinally. Proc. Natl. Acad. Sci. USA *120*, e2216798120. https://doi.org/10.1073/pnas.2216798120.

92. Thomas, C., Ye, F.Q., Irfanoglu, M.O., Modi, P., Saleem, K.S., Leopold, D.A., and Pierpaoli, C. (2014). Anatomical accuracy of brain connections derived from diffusion MRI tractography is inherently limited. Proc. Natl. Acad. Sci. USA *111*, 16574–16579. https://doi.org/10.1073/pnas.1405672111.

93. Demirtaş, M., Burt, J.B., Helmer, M., Ji, J.L., Adkinson, B.D., Glasser, M. F., Van Essen, D.C., Sotiropoulos, S.N., Anticevic, A., and Murray, J.D. (2019). Hierarchical heterogeneity across human cortex shapes large-scale neural dynamics. Neuron *101*, 1181–1194.e13. https://doi.org/10.1016/j.neuron.2019.01.017.

94. Deco, G., Kringelbach, M.L., Arnatkeviciute, A., Oldham, S., Sabaroedin, K., Rogasch, N.C., Aquino, K.M., and Fornito, A. (2021). Dynamical consequences of regional heterogeneity in the brain's transcriptional landscape. Sci. Adv. *7*, eabf4752. https://doi.org/10.1126/sciadv.abf4752.

95. Casey, B.J., Cannonier, T., Conley, M.I., Cohen, A.O., Barch, D.M., Heitzeg, M.M., Soules, M.E., Teslovich, T., Dellarco, D.V., Garavan, H., et al. (2018). The adolescent brain cognitive development (ABCD) study: imaging acquisition across 21 sites. Dev. Cogn. Neurosci. *32*, 43–54. https://doi.org/10.1016/j.dcn.2018.03.001.

96. Di Martino, A., Yan, C.G., Li, Q., Denio, E., Castellanos, F.X., Alaerts, K., Anderson, J.S., Assaf, M., Bookheimer, S.Y., Dapretto, M., et al. (2014). The autism brain imaging data exchange: towards a large-scale evaluation of the intrinsic brain architecture in autism. Mol. Psychiatry *19*, 659–667. https://doi.org/10.1038/mp.2013.78.

97. Jack, C.R., Bernstein, M.A., Fox, N.C., Thompson, P., Alexander, G., Harvey, D., Borowski, B., Britson, P.J., L Whitwell, J., Ward, C., et al. (2008). The Alzheimer's Disease Neuroimaging Initiative (ADNI): MRI methods. J. Magn. Reson. Imaging *27*, 685–691. https://doi.org/10.1002/jmri.21049.

98. Karayanidis, F., Keuken, M.C., Wong, A., Rennie, J.L., de Hollander, G., Cooper, P.S., Ross Fulham, W., Lenroot, R., Parsons, M., Phillips, N., et al. (2016). The Age-ility Project (Phase 1): Structural and functional imaging and electrophysiological data repository. NeuroImage *124*, 1137–1142. https://doi.org/10.1016/j.neuroimage.2015.04.047.

99. Howell, B.R., Styner, M.A., Gao, W., Yap, P.-T., Wang, L., Baluyot, K., Yacoub, E., Chen, G., Potts, T., Salzwedel, A., et al. (2019). The UNC/UMN Baby Connectome Project (BCP): An overview of the study design and protocol development. NeuroImage *185*, 891–905. https://doi.org/10.1016/j.neuroimage.2018.03.049.

100. Holmes, A.J., Hollinshead, M.O., O'Keefe, T.M., Petrov, V.I., Fariello, G. R., Wald, L.L., Fischl, B., Rosen, B.R., Mair, R.W., Roffman, J.L., et al. (2015). Brain Genomics Superstruct Project initial data release with structural, functional, and behavioral measures. Sci. Data *2*, 150031. https://doi.org/10.1038/sdata.2015.31.

101. Lin, Q., Dai, Z., Xia, M., Han, Z., Huang, R., Gong, G., Liu, C., Bi, Y., and He, Y. (2015). A connectivity-based test-retest dataset of multi-modal magnetic resonance imaging in young healthy adults. Sci. Data *2*, 150056. https://doi.org/10.1038/sdata.2015.56.

102. Liang, X., Sun, L., Liao, X., Lei, T., Xia, M., Duan, D., Zeng, Z., Li, Q., Xu, Z., Men, W., et al. (2024). Structural connectome architecture shapes the maturation of cortical morphology from childhood to adolescence. Nat. Commun. *15*, 784. https://doi.org/10.1038/s41467-024-44863-6.

103. Reynolds, J.E., Long, X., Paniukov, D., Bagshawe, M., and Lebel, C. (2020). Calgary Preschool magnetic resonance imaging (MRI) dataset. Data Brief *29*, 105224. https://doi.org/10.1016/j.dib.2020.105224.

104. Shafto, M.A., Tyler, L.K., Dixon, M., Taylor, J.R., Rowe, J.B., Cusack, R., Calder, A.J., Marslen-Wilson, W.D., Duncan, J., Dalgleish, T., et al. (2014). The Cambridge Centre for ageing and neuroscience (Cam-CAN) study protocol: A cross-sectional, lifespan, multidisciplinary examination of healthy cognitive ageing. BMC Neurol. *14*, 204. https://doi.org/10.1186/s12883-014-0204-1.

105. Schmithorst, V.J., Vannest, J., Lee, G., Hernandez-Garcia, L., Plante, E., Rajagopal, A., and Holland, S.K.; CMIND Authorship Consortium (2015). Evidence that neurovascular coupling underlying the BOLD effect increases with age during childhood. Hum. Brain Mapp. *36*, 1–15. https://doi.org/10.1002/hbm.22608.

106. Edwards, A.D., Rueckert, D., Smith, S.M., Abo Seada, S., Alansary, A., Almalbis, J., Allsop, J., Andersson, J., Arichi, T., Arulkumaran, S., et al. (2022). The Developing Human Connectome Project Neonatal Data Release. Front. Neurosci. *16*, 886772. https://doi.org/10.3389/fnins.2022.886772.

107. Xia, M., Si, T., Sun, X., Ma, Q., Liu, B., Wang, L., Meng, J., Chang, M., Huang, X., Chen, Z., et al. (2019). Reproducibility of functional brain alterations in major depressive disorder: Evidence from a multisite resting-state functional MRI study with 1,434 individuals. NeuroImage *189*, 700–714. https://doi.org/10.1016/j.neuroimage.2019.01.074.

108. Gilmore, J.H., Langworthy, B., Girault, J.B., Fine, J., Jha, S.C., Kim, S.H., Cornea, E., and Styner, M. (2020). Individual variation of human cortical structure is established in the first year of life. Biol. Psychiatry Cogn. Neurosci. Neuroimaging *5*, 971–980. https://doi.org/10.1016/j.bpsc.2020.05.012.

109. Van Essen, D.C., Smith, S.M., Barch, D.M., Behrens, T.E.J., Yacoub, E., and Ugurbil, K.; WU-Minn HCP Consortium (2013). The WU-Minn human connectome project: an overview. NeuroImage *80*, 62–79. https://doi.org/10.1016/j.neuroimage.2013.05.041.

110. Bookheimer, S.Y., Salat, D.H., Terpstra, M., Ances, B.M., Barch, D.M., Buckner, R.L., Burgess, G.C., Curtiss, S.W., Diaz-Santos, M., Elam, J. S., et al. (2019). The Lifespan Human Connectome Project in Aging: An overview. NeuroImage *185*, 335–348. https://doi.org/10.1016/j.neuroimage.2018.10.009.

111. Chen, P., Yao, H., Tijms, B.M., Wang, P., Wang, D., Song, C., Yang, H., Zhang, Z., Zhao, K., Qu, Y., et al. (2023). Four distinct subtypes of Alzheimer's disease based on resting-state connectivity biomarkers. Biol. Psychiatry *93*, 759–769. https://doi.org/10.1016/j.biopsych.2022.06.019.

Please cite this article in press as: Liang et al., Dissecting human cortical similarity networks across the lifespan, Neuron (2025), https://doi.org/10.1016/j.neuron.2025.06.018

112. Nooner, K.B., Colcombe, S.J., Tobe, R.H., Mennes, M., Benedict, M.M., Moreno, A.L., Panek, L.J., Brown, S., Zavitz, S.T., Li, Q., et al. (2012). The NKI-Rockland sample: a model for accelerating the pace of discovery science in psychiatry. Front. Neurosci. *6*, 152. https://doi.org/10.3389/fnins.2012.00152.

113. Whitaker, K.J., Vértes, P.E., Romero-Garcia, R., Váša, F., Moutoussis, M., Prabhu, G., Weiskopf, N., Callaghan, M.F., Wagstyl, K., Rittman, T., et al. (2016). Adolescence is associated with genomically patterned consolidation of the hubs of the human brain connectome. Proc. Natl. Acad. Sci. USA *113*, 9105–9110. https://doi.org/10.1073/pnas.1601745113.

114. Jernigan, T.L., Brown, T.T., Hagler, D.J., Akshoomoff, N., Bartsch, H., Newman, E., Thompson, W.K., Bloss, C.S., Murray, S.S., Schork, N., et al. (2016). The pediatric imaging, neurocognition, and genetics (PING) data repository. NeuroImage *124*, 1149–1154. https://doi.org/10.1016/j.neuroimage.2015.04.057.

115. Richardson, H., Lisandrelli, G., Riobueno-Naylor, A., and Saxe, R. (2018). Development of the social brain from age three to twelve years. Nat. Commun. *9*, 1027. https://doi.org/10.1038/s41467-018-03399-2.

116. Tanaka, S.C., Yamashita, A., Yahata, N., Itahashi, T., Lisi, G., Yamada, T., Ichikawa, N., Takamura, M., Yoshihara, Y., Kunimatsu, A., et al. (2021). A multi-site, multi-disorder resting-state magnetic resonance image database. Sci. Data *8*, 227. https://doi.org/10.1038/s41597-021-01004-8.

117. Wei, D., Zhuang, K., Ai, L., Chen, Q., Yang, W., Liu, W., Wang, K., Sun, J., and Qiu, J. (2018). Structural and functional brain scans from the cross-sectional Southwest University adult lifespan dataset. Sci. Data *5*, 180134. https://doi.org/10.1038/sdata.2018.134.

118. Liu, W., Wei, D., Chen, Q., Yang, W., Meng, J., Wu, G., Bi, T., Zhang, Q., Zuo, X.-N., and Qiu, J. (2017). Longitudinal test-retest neuroimaging data from healthy young adults in southwest China. Sci. Data *4*, 170017. https://doi.org/10.1038/sdata.2017.17.

119. Miller, K.L., Alfaro-Almagro, F., Bangerter, N.K., Thomas, D.L., Yacoub, E., Xu, J., Bartsch, A.J., Jbabdi, S., Sotiropoulos, S.N., Andersson, J.L.R., et al. (2016). Multimodal population brain imaging in the UK Biobank prospective epidemiological study. Nat. Neurosci. *19*, 1523–1536. https://doi.org/10.1038/nn.4393.

120. Bozek, J., Makropoulos, A., Schuh, A., Fitzgibbon, S., Wright, R., Glasser, M.F., Coalson, T.S., O'Muircheartaigh, J., Hutter, J., Price, A.N., et al. (2018). Construction of a neonatal cortical surface atlas using Multimodal Surface Matching in the Developing Human Connectome Project. NeuroImage *179*, 11–29. https://doi.org/10.1016/j.neuroimage.2018.06.018.

121. Li, G., Wang, L., Shi, F., Gilmore, J.H., Lin, W., and Shen, D. (2015). Construction of 4D high-definition cortical surface atlases of infants: Methods and applications. Med. Image Anal. *25*, 22–36. https://doi.org/10.1016/j.media.2015.04.005.

122. Glasser, M.F., Sotiropoulos, S.N., Wilson, J.A., Coalson, T.S., Fischl, B., Andersson, J.L., Xu, J., Jbabdi, S., Webster, M., Polimeni, J.R., et al. (2013). The minimal preprocessing pipelines for the Human Connectome Project. NeuroImage *80*, 105–124. https://doi.org/10.1016/j.neuroimage.2013.04.127.

123. Esteban, O., Birman, D., Schaer, M., Koyejo, O.O., Poldrack, R.A., and Gorgolewski, K.J. (2017). MRIQC: Advancing the automatic prediction of image quality in MRI from unseen sites. PLoS One *12*, e0184661. https://doi.org/10.1371/journal.pone.0184661.

124. Ji, J.L., Demšar, J., Fonteneau, C., Tamayo, Z., Pan, L., Kraljič, A., Matkovič, A., Purg, N., Helmer, M., Warrington, S., et al. (2023). QuNex—An integrative platform for reproducible neuroimaging analytics. Front. Neuroinform. *17*, 1104508. https://doi.org/10.3389/fninf.2023.1104508.

125. Feczko, E., Conan, G., Marek, S., Tervo-Clemmens, B., Cordova, M., Doyle, O., Earl, E., Perrone, A., Sturgeon, D., Klein, R., et al. (2021). Adolescent Brain Cognitive Development (ABCD) Community MRI Collection and Utilities. Preprint at bioRxiv. https://doi.org/10.1101/2021.07.09.451638.

126. Makropoulos, A., Robinson, E.C., Schuh, A., Wright, R., Fitzgibbon, S., Bozek, J., Counsell, S.J., Steinweg, J., Vecchiato, K., Passerat-Palmbach, J., et al. (2018). The developing human connectome project: A minimal processing pipeline for neonatal cortical surface reconstruction. NeuroImage *173*, 88–112. https://doi.org/10.1016/j.neuroimage.2018.01.054.

127. Fitzgibbon, S.P., Harrison, S.J., Jenkinson, M., Baxter, L., Robinson, E.C., Bastiani, M., Bozek, J., Karolis, V., Cordero Grande, L., Price, A.N., et al. (2020). The developing Human Connectome Project (dHCP) automated resting-state functional processing framework for newborn infants. NeuroImage *223*, 117303. https://doi.org/10.1016/j.neuroimage.2020.117303.

128. Wang, L., Wu, Z., Chen, L., Sun, Y., Lin, W., and Li, G. (2023). iBEAT V2.0: a multisite-applicable, deep learning-based pipeline for infant cerebral cortical surface reconstruction. Nat. Protoc. *18*, 1488–1509. https://doi.org/10.1038/s41596-023-00806-x.

129. Robinson, E.C., Jbabdi, S., Glasser, M.F., Andersson, J., Burgess, G.C., Harms, M.P., Smith, S.M., Van Essen, D.C., and Jenkinson, M. (2014). MSM: a new flexible framework for Multimodal Surface Matching. NeuroImage *100*, 414–426. https://doi.org/10.1016/j.neuroimage.2014.05.069.

130. Fischl, B. (2012). FreeSurfer. NeuroImage *62*, 774–781. https://doi.org/10.1016/j.neuroimage.2012.01.021.

131. Smith, S.M., Jenkinson, M., Woolrich, M.W., Beckmann, C.F., Behrens, T.E.J., Johansen-Berg, H., Bannister, P.R., De Luca, M., Drobnjak, I., Flitney, D.E., et al. (2004). Advances in functional and structural MR image analysis and implementation as FSL. NeuroImage *23*, S208–S219. https://doi.org/10.1016/j.neuroimage.2004.07.051.

132. Glasser, M.F., Smith, S.M., Marcus, D.S., Andersson, J.L.R., Auerbach, E.J., Behrens, T.E.J., Coalson, T.S., Harms, M.P., Jenkinson, M., Moeller, S., et al. (2016). The human connectome project's neuroimaging approach. Nat. Neurosci. *19*, 1175–1187. https://doi.org/10.1038/nn.4361.

133. Wang, J., Wang, X., Xia, M., Liao, X., Evans, A., and He, Y. (2015). GRETNA: a graph theoretical network analysis toolbox for imaging connectomics. Front. Hum. Neurosci. *9*, 386. https://doi.org/10.3389/fnhum.2015.00386.

134. Xia, M., Wang, J., and He, Y. (2013). BrainNet Viewer: a network visualization tool for human brain connectomics. PLoS One *8*, e68910. https://doi.org/10.1371/journal.pone.0068910.

135. Chang, C.-C., and Lin, C.-J. (2011). LIBSVM: a library for support vector machines. ACM Trans. Intell. Syst. Technol. *2*, 1–27. https://doi.org/10.1145/1961189.1961199.

136. Wickham, H. (2011). Ggplot2. WIREs Computational Stats. *3*, 180–185. https://doi.org/10.1002/wics.147.

137. Markello, R.D., Arnatkeviciute, A., Poline, J.-B., Fulcher, B.D., Fornito, A., and Misic, B. (2021). Standardizing workflows in imaging transcriptomics with the abagen toolbox. eLife *10*, e72129. https://doi.org/10.7554/eLife.72129.

138. Rosen, A.F.G., Roalf, D.R., Ruparel, K., Blake, J., Seelaus, K., Villa, L.P., Ciric, R., Cook, P.A., Davatzikos, C., Elliott, M.A., et al. (2018). Quantitative assessment of structural image quality. NeuroImage *169*, 407–418. https://doi.org/10.1016/j.neuroimage.2017.12.059.

139. Elyounssi, S., Kunitoki, K., Clauss, J.A., Laurent, E., Kane, K., Hughes, D.E., Hopkinson, C.E., Bazer, O., Sussman, R.F., Doyle, A.E., et al. (2023). Uncovering and mitigating bias in large, automated MRI analyses of brain development. Preprint at bioRxiv. https://doi.org/10.1101/2023.02.28.530498.

140. Nadig, A., Seidlitz, J., McDermott, C.L., Liu, S., Bethlehem, R., Moore, T.M., Mallard, T.T., Clasen, L.S., Blumenthal, J.D., Lalonde, F., et al. (2021). Morphological integration of the human brain across adolescence and adulthood. Proc. Natl. Acad. Sci. USA *118*, e2023860118. https://doi.org/10.1073/pnas.2023860118.

141. Gilmore, J.H., Knickmeyer, R.C., and Gao, W. (2018). Imaging structural and functional brain development in early childhood. Nat. Rev. Neurosci. *19*, 123–137. https://doi.org/10.1038/nrn.2018.1.

142. Wu, Z., Wang, L., Lin, W., Gilmore, J.H., Li, G., and Shen, D. (2019). Construction of 4D infant cortical surface atlases with sharp folding patterns via spherical patch-based group-wise sparse representation. Hum. Brain Mapp. *40*, 3860–3880. https://doi.org/10.1002/hbm.24636.

143. Williams, L.Z.J., Fitzgibbon, S.P., Bozek, J., Winkler, A.M., Dimitrova, R., Poppe, T., Schuh, A., Makropoulos, A., Cupitt, J., O'Muircheartaigh, J., et al. (2023). Structural and functional asymmetry of the neonatal cerebral cortex. Nat. Hum. Behav. *7*, 942–955. https://doi.org/10.1038/s41562-023-01542-8.

144. Arnatkevičiūtė, A., Fulcher, B.D., and Fornito, A. (2019). A practical guide to linking brain-wide gene expression and neuroimaging data. NeuroImage *189*, 353–367. https://doi.org/10.1016/j.neuroimage.2019.01.011.

145. Newman, M.E. (2006). Modularity and community structure in networks. Proc. Natl. Acad. Sci. USA *103*, 8577–8582. https://doi.org/10.1073/pnas.0601602103.

146. Watts, D.J., and Strogatz, S.H. (1998). Collective dynamics of 'small-world'networks. Nature *393*, 440–442. https://doi.org/10.1038/30918.

147. Humphries, M.D., and Gurney, K. (2008). Network 'small-world-ness': a quantitative method for determining canonical network equivalence. PLoS One *3*, e0002051. https://doi.org/10.1371/journal.pone.0002051.

148. Maslov, S., and Sneppen, K. (2002). Specificity and stability in topology of protein networks. Science *296*, 910–913. https://doi.org/10.1126/science.1065103.

149. Alexander-Bloch, A.F., Shou, H., Liu, S., Satterthwaite, T.D., Glahn, D.C., Shinohara, R.T., Vandekar, S.N., and Raznahan, A. (2018). On testing for spatial correspondence between maps of human brain structure and function. NeuroImage *178*, 540–551. https://doi.org/10.1016/j.neuroimage.2018.05.070.

150. Dunn, P.K., and Smyth, G.K. (1996). Randomized Quantile Residuals. J. Comp. Graph. Stat. *5*, 236–244. https://doi.org/10.1080/10618600.1996.10474708.

151. Wolfers, T., Doan, N.T., Kaufmann, T., Alnæs, D., Moberget, T., Agartz, I., Buitelaar, J.K., Ueland, T., Melle, I., Franke, B., et al. (2018). Mapping the Heterogeneous Phenotype of Schizophrenia and Bipolar Disorder Using Normative Models. JAMA Psychiatry *75*, 1146–1155. https://doi.org/10.1001/jamapsychiatry.2018.2467.

152. Cui, Z., and Gong, G. (2018). The effect of machine learning regression algorithms and sample size on individualized behavioral prediction with functional connectivity features. NeuroImage *178*, 622–637. https://doi.org/10.1016/j.neuroimage.2018.06.001.

153. Tian, Y.E., Di Biase, M.A., Mosley, P.E., Lupton, M.K., Xia, Y., Fripp, J., Breakspear, M., Cropley, V., and Zalesky, A. (2023). Evaluation of brain-body health in individuals with common neuropsychiatric disorders. JAMA Psychiatry *80*, 567–576. https://doi.org/10.1001/jamapsychiatry.2023.0791.

154. Owen, A.B. (1995). Nonparametric likelihood confidence bands for a distribution function. J. Am. Stat. Assoc. *90*, 516–521. https://doi.org/10.1080/01621459.1995.10476543.

155. Shapiro, S.S., and Wilk, M.B. (1965). An analysis of variance test for normality (complete samples). Biometrika *52*, 591–611. https://doi.org/10.1093/biomet/52.3-4.591.

156. Dinga, R., Fraza, C.J., Bayer, J.M.M., Kia, S.M., Beckmann, C.F., and Marquand, A.F. (2021). Normative modeling of neuroimaging data using generalized additive models of location scale and shape. Preprint at bioRxiv. https://doi.org/10.1101/2021.06.14.448106.

157. Zalesky, A., Fornito, A., Harding, I.H., Cocchi, L., Yücel, M., Pantelis, C., and Bullmore, E.T. (2010). Whole-brain anatomical networks: does the choice of nodes matter? NeuroImage *50*, 970–983. https://doi.org/10.1016/j.neuroimage.2009.12.027.

Please cite this article in press as: Liang et al., Dissecting human cortical similarity networks across the lifespan, Neuron (2025), https://doi.org/10.1016/j.neuron.2025.06.018

STAR★METHODS

KEY RESOURCES TABLE

REAGENT or RESOURCE	SOURCE	IDENTIFIER
Deposited data		
Adolescent Brain Cognitive Development Study	Casey et al.[95]	https://nda.nih.gov/
Autism Brain Imaging Data Exchange Initiative	Di Martion et al.[96]	https://fcon_1000.projects.nitrc.org/indi/abide/
Alzheimer's Disease Neuroimaging Initiative	Jack et al.[97]	https://adni.loni.usc.edu/
Age_ility Project	Karayanidis et al.[98]	https://www.nitrc.org/projects/age-ility
Baby Connectome Project	Howell et al.[99]	https://nda.nih.gov/
Brain Genomics Superstruct Project	Holmes et al.[100]	https://doi.org/10.7910/DVN/25833
Connectivity-based Brain Imaging Research Database (C-BIRD) at Beijing Normal University	Lin et al.[101]	https://fcon_1000.projects.nitrc.org/indi/CoRR/html/bnu_1.html
Children Brain Development (CBD) project	Liang et al.[102]	N/A
Calgary Preschool MRI Dataset	Reynolds et al.[103]	https://osf.io/axz5r/
Cambridge Centre for Ageing and Neuroscience Dataset	Shafto et al.[104]	https://www.cam-can.org/index.php?content=dataset
Cincinnati MR Imaging of Neurodevelopment	Schmithorst et al.[105]	https://nda.nih.gov/edit_collection.html?id=2329
Developing Human Connectome Project	Edwards et al.[106]	http://www.developingconnectome.org/data-release/second-data-release/
Disease Imaging Data Archiving - Major Depressive Disorder Working Group	Xia et al.[107]	N/A
University of North Carolina Early Brain Development Study	Gilmore et al.[108]	https://www.med.unc.edu/psych/research/psychiatry-department-research-programs/early-brain-development-research/
Human Connectome Project	Van Essen et al.[109]	https://www.humanconnectome.org
Lifespan Human Connectome Project	Bookheimer et al.[110]	https://nda.nih.gov/
Multi-Center Alzheimer Disease Imaging Consortium (MCADI) dataset	Chen et al.[111]	N/A
Nathan Kline Institute-Rockland Sample Dataset	Nooner et al.[112]	https://fcon_1000.projects.nitrc.org/indi/pro/nki.html
Neuroscience in Psychiatry Network Dataset	Whitaker et al.[113]	https://nspn.org.uk/
Pediatric Imaging, Neurocognition, and Genetics (PING) Data Repository	Jernigan et al.[114]	http://pingstudy.ucsd.edu/
Pixar Dataset	Richardson et al.[115]	https://openfmri.org/dataset/ds000228/
Strategic Research Program for Brain Sciences (SRPBS) MRI Dataset	Tanaka et al.[116]	https://bicr-resource.atr.jp/srpbsopen/
Southwest University Adult Lifespan Dataset	Wei et al.[117]	http://fcon_1000.projects.nitrc.org/indi/retro/sald.html
Southwest University Longitudinal Imaging Multimodal Brain Data Repository	Liu et al.[118]	http://fcon_1000.projects.nitrc.org/indi/retro/southwestuni_qiu_index.html
UK Biobank Brain Imaging Dataset	Miller et al.[119]	https://www.ukbiobank.ac.uk/

(*Continued on next page*)

Continued

REAGENT or RESOURCE	SOURCE	IDENTIFIER
dhcpSym surface atlases	Bozek et al.[120]	https://brain-development.org/brain-atlases/atlases-from-the-dhcp-project/cortical-surface-template/
UNC 4D infant cortical surface atlases	Li et al.[121]	https://bbm.web.unc.edu/tools/
fs_LR_32k surface atlas	Glasser et al.[122]	https://balsa.wustl.edu/
Allen Human Brain Atlas datasets	Hawrylycz et al.[36]	https://human.brain-map.org/static/download
Brain charts of morphometric brain networks	This paper	https://github.com/Xinyuan-Liang/Cortical_Similarity_Networks_Lifespan (Zenodo: https://doi.org/10.5281/zenodo.15662487)
Software and algorithms		
MRIQC	Esteban et al.[123]	https://github.com/nipreps/mriqc
QuNex	Li et al.[124]	https://gitlab.qunex.yale.edu/
HCP pipeline	Glasser et al.[122]	https://github.com/Washington-University/HCPpipelines/releases
ABCD-HCP pipeline	Feczko et al.[125]	https://github.com/DCAN-Labs/abcd-hcp-pipeline
dHCP structural pipeline	Makropoulos et al.[126]	https://github.com/BioMedIA/dhcp-structural-pipeline
dHCP functional pipeline	Fitzgibbon et al.[127]	https://git.fmrib.ox.ac.uk/seanf/dhcp-neonatal-fmri-pipeline
iBEAT pipeline	Wang et al.[128]	https://github.com/iBEAT-V2/iBEAT-V2.0-Docker
MSM	Robinson et al.[129]	https://github.com/ecr05/MSM_HOCR
FreeSurfer	Fischl[130]	https://surfer.nmr.mgh.harvard.edu/
FSL	Smith et al.[131]	https://fsl.fmrib.ox.ac.uk/fsl/fslwiki
Connectome Workbench	Glasser et al.[132]	https://www.humanconnectome.org/software/connectome-workbench
MATLAB	Mathworks	https://www.mathworks.com/products/matlab.html
SPM	Wellcome Trust Centre for Neuroimaging (UCL)	https://www.fil.ion.ucl.ac.uk/spm/software/spm12
GRETNA	Wang et al.[133]	https://www.nitrc.org/projects/gretna
BrainNet Viewer	Xia et al.[134]	https://www.nitrc.org/projects/bnv
cifti-matlab	Glasser et al.[122]	https://github.com/Washington-University/cifti-matlab
LIBSVM	Chang and Lin[135]	https://www.csie.ntu.edu.tw/~cjlin/libsvm/
MIND calculation code	Sebenius et al.[20]	https://github.com/isebenius/MIND
Python	Python Software Foundation	https://www.python.org
R	R Foundation	https://www.r-project.org
GAMLSS	Stasinopoulos and Rigby[39]	https://www.gamlss.com/
ggplot2	Wickham[136]	https://ggplot2.tidyverse.org/
Abagen	Markello et al.[137]	https://github.com/rmarkello/abagen
Original code	This paper	https://github.com/Xinyuan-Liang/Cortical_Similarity_Networks_Lifespan (Zenodo: https://doi.org/10.5281/zenodo.15662487)

EXPERIMENTAL MODEL AND SUBJECT DETAILS

Participants

In this study, we aggregated 3T structural MRI data from multisite neuroimaging datasets and included corresponding task-free fMRI data where available. The original multimodal neuroimaging dataset consisted of the data of 45,833 participants aged 0 to 80 years from 183 sites across 30 different datasets. For participants who underwent imaging scans across multiple sessions, only the scan from a single session was selected for inclusion. The demographic details of the participants and the parameters used for the imaging scans across different sites are detailed in Tables S1 and S2, respectively. All participants and/or their legal guardians provided written informed consent. The recruitment procedures were approved by the local ethics committees corresponding to each dataset.

METHOD DETAILS

Image quality control

To ensure that the scans were of appropriate quality, we implemented a four-step quality control framework that combined automated evaluation techniques and expert manual review to assess all the structural and functional images thoroughly.[34] The overview of the quality control process for structural and functional MR images are provided at https://github.com/Xinyuan-Liang/Cortical_Similarity_Networks_Lifespan.

(i) Quality control of the raw imaging data

We first performed a preliminary quality assessment to exclude scans with acquisition issues. We performed initial quality control of the dHCP, HCP-Development, HCP-Ageing, HCP-Young Adult, and ABCD datasets according to their provided standard criteria for image quality and recommended inclusion criteria. For the BCP dataset, each scan was reviewed in detail by two experienced pediatric neuroradiologists. For the other datasets, we used the MRI Quality Control (MRIQC) tool to conduct automated evaluations, generating quality metrics for each T1-weighted (T1w), T2-weighted (T2w) and functional MRI image. In each dataset, structural images were disqualified if they were identified as outliers—exceeding 1.5 times the interquartile range (IQR) in terms of at least three of the following quality metrics: the entropy-focus criterion (EFC), foreground-background energy ratio (FBER), coefficient of joint variation (CJV), contrast-to-noise ratio (CNR), signal-to-noise ratio (SNR), and Dietrich's SNR (SNRd). Functional images were similarly excluded if flagged as outliers in terms of three or more of the following metrics: the AFNI's outlier ratio (AOR), AFNI's quality index (AQI), DVARS_std, DVARS_vstd, SNR, and temporal signal-to-noise ratio (tSNR).

(ii) Determination of whether to pass the entire processing pipeline

After the initial quality check, the images were submitted to the subsequent preprocessing stages. These stages are detailed in the 'Data preprocessing pipeline' section below. Scans that failed to progress through the entire processing pipeline were excluded.

(iii) Surface quality control and head motion control

For structural scans, surface quality was evaluated via the Euler number, a mathematical descriptor that quantifies the topological complexity of a surface. The Euler number is computed as 2-2n, with n denoting the number of topological defects such as holes or handles. Previous studies have demonstrated that the Euler number can serve as a reliable and quantitative measure for identifying structural images unsuitable for analysis.[4,138,139] A higher Euler number signifies fewer topological defects, indicative of high-quality cortical surface reconstruction. Images were considered outliers and excluded if the Euler number fell below 1.5 times the interquartile range from the study-specific distribution (Q1–1.5*IQR). We further excluded participants from all datasets with Euler numbers less than -217 to ensure that the brain surface reconstruction was of sufficient quality, consistent with the criteria used in previous studies.[138,140] For functional images, scans with large head motion artifacts (mean frame displacement (FD) > 0.5 mm or more than 20% of frames with FD > 0.5 mm) were excluded, along with scans with fewer than 100 final time points or a percentage of final time points to relative original time points <90%.

(iv) Visual double-check

To further validate that the remaining scans were of high quality, we implemented a detailed visual QC process. (a) A visual QC team was assembled, consisting of five anatomically trained experts: X.Y.L., L.L.S., C.X.P., Q.W., and Q.Y. Each participant performed QC of one 2D picture generated for the structural scan. If functional scans were available, two additional 2D pictures were produced for these scans. (b) X.Y.L. and L.L.S. undertook the first round of visual inspection for both structural and functional datasets, noting the IDs of scans with quality issues. (c) The pictures were then equally distributed to Q.W., Q.Y., and C.X.P. for further evaluation. The participant IDs corresponding to images with any quality defects were recorded.

The final participant exclusion list was generated by combining these records. The QC team held detailed discussions to ensure consistent application of the exclusion criteria. The criteria for excluding structural MRI data focus on detecting artifacts and assessing the quality of cortical segmentation, surface reconstruction, and surface registration. For participants with T2w images, those whose images presented with abnormal myelination distributions (as measured by the T1/T2 ratio) were also excluded. The functional MRI data were assessed in terms of brain coverage, alignment of individual data with structural data and the standard space, and the accuracy of volume-to-surface mapping; participants whose images displayed any of these issues were excluded. A comprehensive tutorial on visual QC procedures[34] is available at https://github.com/sunlianglong/BrainChart-FC-Lifespan/blob/main/QC/README.md.

These strict procedures ensured that scans containing imaging artifacts or errors could be detected and excluded, increasing the reliability and precision of the neuroimaging dataset. Following this procedure, the final sample included 33,937 healthy participants and 1,202 patients (180 patients with AD, 622 patients with MDD, and 400 patients with ASD) with high-quality structural images. A subset of these individuals, including 32,887 healthy participants and 1,202 patients, had corresponding high-quality functional images.

Data processing

(i) Structural data preprocessing

Owing to the substantial variability in the structure and function of the human brain across the lifespan, employing a unified structural preprocessing pipeline across all datasets would be significantly challenging,[34] particularly for datasets corresponding to the perinatal and infancy periods, when the anatomical characteristics are substantially different from those in adulthood.[141] Given the lack of a uniform applicable preprocessing pipeline for all stages of life, it was essential to adapt specific methods for datasets focusing on early development while maintaining consistency in preprocessing approaches across other age groups.

For participants aged 2 years and above (except those in the ABCD dataset), we used the HCP structural preprocessing pipeline (v4.4.0-rc-MOD-e7a6af9)[122] containerized through the QuNex platform (v0.93.2).[124] This pipeline consists of three stages. (a) PreFreeSurfer Stage. This initial phase included several preprocessing procedures, such as brain extraction, denoising, and bias field correction for both T1w and T2w (if available) MRI data. (b) FreeSurfer Stage. This stage focuses on generating cortical surfaces from the normalized structural image, including segmentation of brain tissues and the creation of pial, white, and mid-thickness surfaces, followed by alignment to the standard *fsaverage* atlas. (c) PostFreeSurfer Stage. The final stage involves converting the processed data into HCP format (CIFTI), aligning volumetric data to the MNI standard space through nonlinear registration, and mapping surface data to the standard fs_LR_32k space via spherical registration and surface downsampling. For participants in the ABCD dataset, the T1w imaging data were processed with FreeSurfer software, following the same procedures as the FreeSurfer Stage of the HCP pipeline. To obtain regional morphometric measurements at the individual level, the parcellation atlas in the standard *fsaverage* space were registered back to each participant's surface space.

For participants aged 0–24 months, we used the iBEAT V2.0 pipelines.[128] Compared with alternative approaches, this pipeline is optimized for preprocessing early-age neuroimaging data with advanced algorithms and shows superior performance in tissue segmentation and cortical reconstruction.[128] The iBEAT V2.0 pipeline involves (a) inhomogeneity correction for T1w/T2w images; (b) skull stripping and cerebellum removal. For participants with incomplete cerebellum removal, we performed frame-by-frame manual corrections. (c) tissue segmentation; (d) cortical surface reconstruction; (e) topological correction of the white matter surface; and (f) reconstruction of the inner and outer cortical surfaces. The individual cortical surfaces derived from the iBEAT structural pipelines were aligned to the adult fs_LR_32k standard space through a three-step registration process. Initially, the individual surfaces were subsequently aligned to their corresponding monthly age templates.[142] These monthly templates were subsequently aligned to the 12-month template, which in turn was aligned to the fs_LR_32k surface template. We then transformed the parcellation atlas from the fsaverage standard space to the fs_LR_32k space. On the basis of the registration information obtained from the process described above, the parcellation atlas in the standard fs_LR_32k space was first registered back to the corresponding monthly age templates and then to each participant's surface space to obtain regional morphometric measurements at the individual level (Figure S2).

For participants from the dHCP dataset (postmenstrual age range of 37 to 42 weeks and full-term infants, defined as 0 years in this study), we applied the dHCP structural pipelines,[126] which is specifically designed to handle the unique characteristics of neonatal MRI data. This HCP-style pipeline includes several steps: (a) bias correction and brain extraction from motion-corrected, reconstructed T2w images; (b) tissue segmentation; (c) cortical reconstruction of the white matter surface; (d) correction of surface topology; (e) creation of pial and mid-thickness surfaces; (f) generation of inflated surfaces from the white matter surface; and (g) surface registration through spherical projection. The specific steps for surface registration were as follows. First, individual surfaces were registered to specific templates corresponding to the individual's postmenstrual age.[143] Second, 37-39 postmenstrual weeks templates and 41-42 postmenstrual weeks templates were registered to the 40-week template. Third, the 40-week template was then registered to the fs_LR_32k surface template from adulthood. We then transformed the parcellation atlas from the fsaverage standard space to the fs_LR_32k space. On the basis of the registration information obtained from the process described above, the parcellation atlas in the standard fs_LR_32k space was registered back to each participant's native space. The overview of the of the surface registration strategy are provided at https://github.com/Xinyuan-Liang/Cortical_Similarity_Networks_Lifespan.

(ii) Functional data preprocessing in volumetric space

For individuals aged two years and older, we implemented the HCP functional preprocessing pipelines.[122] The fMRIVolume stage included the following steps. (a) Slice timing correction. This step was performed for single-band acquisitions to correct temporal misalignments; however, it was not required for multiband acquisitions. (b) Motion correction. EPI images are aligned to the single-band reference image via 6 degree-of-freedom (DOF) FLIRT registration. When single-band imaging data were not available, the first fMRI frame served as the reference. The motion parameters, including translations, rotations, and their derivatives, were recorded. These parameters, with demeaned and linearly detrended parameters, were used to perform subsequent nuisance regression analyses. (c) EPI distortion correction. Geometric distortion correction was conducted via either the opposite-phase encoded spin-echo images (when LR-RL or AP-PA encoded acquisitions were available) or the regular (gradient-echo) fieldmap images (when fieldmap acquisitions were available). If neither image was available, this step was skipped. (d) Anatomical registration. The fMRI images were aligned to the corresponding T1w image using 6 DOF FLIRT with boundary-based registration (BBR). (e) Intensity normalization. The fMRI data, masked by the final brain mask from the PostFreeSurfer structural pipeline, were finally normalized to a 4D whole-brain average of 10,000. To mitigate the computational burden of fMRI processing of the large ABCD dataset, we chose to use the community-shared, preprocessed data released through the ABCD-BIDS Community Collection[125] (ABCD collection 3165; https://github.com/ABCD-STUDY/nda-abcd-collection-3165). The multimodal neuroimaging data were preprocessed using the ABCD-HCP pipeline, a variant of the HCP pipeline adapted to better suit the ABCD dataset. Modifications to the ABCD-HCP structural pipeline include structural volume registration algorithms and bias field correction methods. Notably, the fMRIVolume stage remained unchanged. Further details of these modifications can be found in the online document (https://collection3165.readthedocs.io/en/stable/pipelines/).

For participants aged 0–24 months, we adapted HCP-style procedures to preprocess volumetric fMRI data. (a) Motion correction. The functional images were aligned to the single-band reference image using 6 DOF FLIRT registration. When a single-band reference was not available, we used mean functional images (with all frames aligned to the first frame) as the reference. (b) Distortion correction. Distortion correction was applied using opposite-phase encoding (AP-PA) spin-−echo images. This step was only performed for participants with available images. (c) EPI to anatomical registration. The fMRI reference image was registered to the corresponding anatomical image (T1w or T2w image) using 6 DOF FLIRT registration.

For participants of postmenstrual age from 37 to 42 weeks, we applied the dHCP functional pipeline.[127] Building on the foundation of the HCP pipeline and the FSL FEAT pipeline, this pipeline is designed specifically for neonatal fMRI analysis. The key components of the pipeline included the following steps. (a) Fieldmap preprocessing. This step involves calculating the susceptibility distortion field based on the opposite-phase encoded spin−echo images and subsequent alignment of this field to the functional data. (b) Registration. This step includes BBR of the fieldmap magnitude to the T2w image, BBR of the single-band reference image to the T2w image with incorporation of field map-based distortion correction, and 6 DOF FLIRT registration of the first volume of the functional multiband EPI to the single-band reference image. (c) Susceptibility and motion correction. This step includes slice-to-volume motion correction, motion-by-susceptibility distortion correction, and estimation of motion nuisance regressors. These steps resulted in distortion-corrected and motion-corrected 4D multiband EPI images in the T2w native volumetric space.

The objective of the fMRISurface stage of the HCP functional pipeline to map the volume time series data onto the standardized CIFTI gray ordinate space. For participants whose images were preprocessed by the dHCP and iBEAT pipelines, we followed the same steps of the HCP fMRISurface pipeline to ensure precise representation of cortical BOLD signals on the surface. This involves segregating the fMRI volumetric data into left and right hemispheres and applying a partial-volume weighted, ribbon-constrained volume-to-surface mapping technique[122] to map data accurately onto each participant's mid-thickness surface. The time series data were subsequently transformed from the individual's native space to the fs_LR_32k standard space via surface registration transformations derived from the structural preprocessing stage.

(iii) Functional data postprocessing

For the ABCD dataset, we applied the ABCD-HCP functional pipeline, which uses DCANBOLDProcessing software (https://collection3165.readthedocs.io/en/stable/pipelines/) to minimize spurious variance that is unlikely to reflect neural activity. For the other datasets, we uniformly postprocessed the preprocessed fMRI data with SPM12 (v6470) and GRETNA (v2.0.0) with a uniform pipeline. Specifically, the following steps were applied to the time series data for each vertex in the fs_LR_32k space (59,412 vertices in total): linear trend removal, regression of nuisance signals (24 head motion parameters, white matter signals, cerebrospinal fluid signals, and global signals), and temporal bandpass filtering (0.01–0.08 Hz). To mitigate the effects of head motion, we further implemented motion censoring by discarding volumes with a FD greater than 0.5 mm and their adjacent volumes (one before and two after). To maintain the temporal continuity of the fMRI time series, we subsequently filled these censored frames using a linear interpolation. These interpolated data were retained in the time series prior to the construction of the functional connectivity matrices. Surface-based smoothing was then conducted with a 6-mm full width at half-maximum (FWHM) kernel.

(iv) Microarray gene expression data preprocessing

Regional gene expression data were obtained from the Allen Human Brain Atlas (http://human.brain-map.org).[36] Since samples from the right hemisphere were available for only two of the six donors (mean age: 42.50 ± 13.38 years; one female), analyses were restricted to the left hemisphere. The regional microarray expression data were preprocessed using the abagen toolbox (https://github.com/netneurolab/abagen).[137,144] Microarray gene expression data were preprocessed following standard procedures, encompassing probe reannotation, background noise filtering, selection of the most stable probe per gene, spatial assignment of tissue samples to brain regions (using the DK-318 atlas), normalization across donors using a scaled robust sigmoid function, and averaging across samples and donors. Only genes with differential stability values greater than 0.1 were retained for subsequent analyses. The full preprocessing details are available in our previous study.[102] After preprocessing, a gene expression matrix (156 brain regions × 8470 gene expression levels) was generated.

Construction of morphometric networks and functional networks

To construct the individual morphometric and functional networks, we first parcellated the cerebral cortex into 318 cortical regions (219 of which were used for validation) on the basis of the randomly modified Desikan-Killiany atlas. The detailed construction method is described below.

(i) Morphometric brain networks

We estimated the individual morphometric network via the state-of-the-art MIND method.[20] Specifically, for each participant, we obtained five morphological features through surface reconstruction: surface area (SA), cortical thickness (CT), gray matter volume (Vol), mean curvature (MC) and sulcal depth (SD). Each feature was standardized (*Z* score) across all vertices. The morphometric similarity between each pair of regions was estimated by calculating the regional multivariate Kullback-Leibler (KL) divergence of these five vertex-level features. By leveraging a k-nearest neighbor approach, the multivariate KL divergence can be efficiently estimated from vertex-level morphometric measures, thus circumventing the challenges of estimating probability density functions in

Please cite this article in press as: Liang et al., Dissecting human cortical similarity networks across the lifespan, Neuron (2025), https://doi.org/10.1016/j.neuron.2025.06.018

high dimensional spaces. For example, the KL divergence from region *a* to region *b* was represented by $\widehat{D}_{KL}(P_a \parallel P_b)$. The symmetric KL divergence was obtained using the following function.

$$\widehat{D}(P_a, P_b) = max(\widehat{D}_{KL}(P_a \parallel P_b), 0) + max(\widehat{D}_{KL}(P_b \parallel P_a), 0)$$

Finally, the morphometric similarity value between region *a* and region *b* was estimated as follows:

$$\text{MIND}\ (a, b) = \frac{1}{1+\widehat{D}(P_a, P_b)}$$

(ii) Functional brain networks

We first averaged the post-processing time courses of all vertices within each region. The individual functional networks were then estimated by calculating the pairwise Pearson correlation coefficients between regional time courses, which were then subjected to Fisher's r-to-z transformation. The resulting *Z* score matrix was used as the individual functional connectome for further analysis.

Morphometric similarity strength analysis

For each participant, the global variance of the morphometric networks was quantified by calculating the standard deviation of all connections (i.e., morphometric similarity), and the global mean of the networks was obtained by averaging the values of all connections. Intra-class connectivity was defined as the average of all pairwise morphometric similarities among regions within the same cytoarchitectonic class, whereas inter-classes connectivity was defined as the average of all pairwise connections between regions in one class and regions in other classes. The regional MSS was calculated as the average of the connections with all other regions.

To investigate the influence of the distance effect on the morphometric networks, for each participant, all connections within each hemisphere were divided into three categories on the basis of inter-regional Euclidean distance. The approximate anatomical distance of each pair of regions was determined by calculating the Euclidean distance between the centroids of the two regions; interhemispheric connections were not included because of the large discrepancy between the actual axonal projection length and the Euclidean distance between regions in the two hemispheres.[45] The connections were categorized into three bins: short, middle, and long. Short connections comprised the shortest 15%, middle connections included those between 15% and 60%, and long connections included the longest 40%. For each bin, the mean of all connections was calculated to investigate the growth pattern of the distance-dependent morphometric similarity.

Graph-theory analysis

To analyses the graph theoretical metrics of the morphometric networks, first, we binarized the individual networks by applying a 10% density threshold. The graph theory measures, including the modularity and small-world measures (Gamma (γ), Lamda (λ), and Sigma (σ)), are defined below. All analyses were performed with GRETNA software.[133]

Modularity

Modularity reflects the degree to which a network can be divided into distinct modules. Nodes within the same module are more densely connected with each other than with nodes in other modules.[145] To characterize the modular structure of each morphometric network, we calculated the modularity index *Q*. For a given partition *p* of the network, *Q* was defined as:

$$Q(p) = \sum_{\mathrm{i}=1}^{N_\mathrm{m}} \left[\frac{l_\mathrm{i}}{L} - \left(\frac{d_\mathrm{i}}{2L} \right)^2 \right]$$

where N_m is the number of modules, L is the total number of connections in the network, l_i is the number of connections between nodes within the module *i*, and d_i is the sum of the node degrees in module *i*. The maximum modularity index was generated through a spectral optimization algorithm.[145]

Small-world properties

A small-world network is characterized by high local among-node clustering and short average path lengths.[146,147] The degree of clustering in a network is quantified by the clustering coefficient. The clustering coefficient (C_i) of node *i* is defined as the ratio of the actual number of connections (e_i) between its neighbors to the maximum possible number of connections between them, which is given by $k_i(k_i - 1)/2$; then the clustering coefficient of a network (C_p) is the average of the clustering coefficients across all nodes. The shortest path characterizes the optimal route for information transfer between nodes in a network. For nodes *i* and *j*, the shortest path (L_{ij}) is defined as the path with the minimum number of edges connecting them. The shortest path length (L_p) represents the average shortest path length of the network between all pairs of nodes within the network. The C_p and L_p values of the brain networks were then compared with those of random networks. Specifically, we generated 100 random networks with same nodes, edges, and degree distributions as the empirical networks.[148] γ was defined as $\gamma = C_p^{\text{real}}/C_p^{\text{rand}}$, and λ was defined as $\lambda = L_p^{\text{real}}/L_p^{\text{rand}}$. The small-worldness ($\sigma$) was defined as $\sigma = \gamma/\lambda$, which is greater than 1 for small-world networks.

Lifespan associations of morphometric networks and functional networks

We first estimated lifespan growth patterns of functional connectivity strength using GAMLSS models in which age was included as a smoothing term, sex and mean FD were included as covariates, and the scanner site was included as a random effect. Then, we obtained individual global morphology-function coupling by calculating Pearson's correlation coefficient between the upper triangle edges of the morphometric brain network and the functional network. For each region, we estimated regional morphology-function coupling by calculating Pearson's correlation coefficient between the morphometric similarity profiles and the functional connectivity profiles. Age-related changes in coupling were subsequently analyzed with normative models by setting age as a smoothing term, sex, the Euler number, and in-scanner head motion (mean FD) as covariates, and the scanner site as a random effect. Additionally, we calculated the mean regional coupling and its growth rate within each cytoarchitectonic class at each time point.

To further explore the potential associations between morphometric similarity and functional connectivity, we computed Pearson correlations at each time point (with intervals of 0.01 years): between the regional MSS maps and regional coupling maps and between their growth rate maps. We employed a spatial permutation test ("spin test")[25,149] to assess the significance of the correlation and applied the FDR correction for multiple comparisons.

Lifespan associations between morphometric networks and brain metabolism

To understand the relationship between morphometric network and brain metabolic demands, we employed the regional metabolic data from a previous study.[35] PET-based measurements of brain metabolism, including the AG, CBF, CMRGlc, and $CMRO_2$, were from 165 cognitively normal adults aged 20 to 82 years. We analyzed age-related changes in brain metabolism measures through normative GAMLSS models by setting age as a smooth term, and sex as a covariate. Regional curves of metabolism measures were modeled for 34 bilateral cortical regions, as defined by the Desikan-Killiany parcellation. Given that the study[35] only provides metabolic data for 34 cortical regions, for comparison, we resampled the MSSs from the 318 parcellations to the Desikan-Killiany parcellation and averaged the values of the left and right hemispheres. We subsequently computed Pearson's correlation coefficients between the spatial distributions of MSS and each metabolic measure at each time point (with intervals of 0.01 years). We employed a spatial permutation test ("spin test")[25,149] to assess the significance of the correlation and applied the FDR correction for multiple comparisons.

Lifespan associations between morphometric networks and gene expression profiles

We used PLS regression analysis to explore the associations between the transcriptional profiles (8470 genes from 156 cortical regions in the left hemisphere) and the MSS growth rate maps at each representative age. Gene expression data were used as predictor variables, and the Z-map of the MSS growth rate was set as the response variable. We employed a spatial autocorrelation-corrected permutation test ("spin" test) to determine whether the variance explained by each PLS component was significantly greater than that expected by chance. For each significant component, we performed bootstrapping to estimate the variability of gene weights and computed *Z* scores by dividing each weight by its bootstrap-derived standard error. Genes with positive weights ($Z > 5$) or negative weights ($Z < -5$) were then input into the Metascape website (https://metascape.org/gp/index.html#/main/step1) to identify enriched Gene Ontology terms. We identified the following genes with positive and negative weights at each time point: 2,160 and 2,025 genes at 0 months, 2,119 and 1,982 genes at 1 year, 2,095 and 1,943 genes at 2 years, 2,027 and 1,878 genes at 3 years, 1,950 and 1,777 genes at 4 years, 1,698 and 1,519 genes at 6 years, and 918 and 734 genes at 8 years, respectively. Significant enrichment was determined on the basis of the following thresholds: (1) a P value cutoff of 1×10^{-5} for the advanced parameter settings, and (2) a false discovery rate-adjusted *p* value (p_{FDR}) < 0.05.

Clinical relevance of morphometric network-based normative models in brain disorders

To ascertain the clinical relevance of the established morphometric normative models, we included participants with one of three brain disorders. All quality control, image preprocessing, and network analysis procedures were identical to those used for the morphometric network-based normative modeling. The final analyses included the data from 568 HCs and 400 patients with ASD from the ABIDE dataset (13 sites), 535 HCs and 622 patients with MDD from the DIDA-MDD dataset (5 sites), and 187 HCs and 180 patients with AD from the MCADI dataset (5 sites).

(i) Individual deviation Z scores

The standard protocol for normative model[48] emphasizes the importance of incorporating some control samples from the same imaging sites as the patients in the testing set. This is done to verify that the observed case-control differences are not due to performing analyses with controls in the training set and cases in the testing set.[48,49] This approach also allows estimation of site effects within the case-control datasets. To establish the normative models for all three disorders using the same set of healthy participants, all the HCs in the three case-control datasets were randomly divided in half ($n_{\text{HC-train}} = 641$; $n_{\text{HC-test}} = 649$), stratified by age, sex, and site. Lifespan normative models were reconstructed with the training set ($n_{\text{train}} = 33{,}288$), which consisted of the data of half of the HCs ($n_{\text{HC-train}} = 641$) and all samples from other datasets that did not include patient data ($n = 32{,}647$). The testing set, comprising the data of the other half of the HCs ($n_{\text{HC-test}} = 649$) and the patient cases, was used as a completely independent set to determine the deviation scores. Specifically, the individual quantile scores were first estimated relative to the normative curves. The deviation *Z* scores were subsequently derived via quantile randomized residuals,[150] an approach that transforms quantiles of the fitted JSU distribution into standard Gaussian-distribution *Z* scores. This process was repeated 100 times, generating 100 new models and 100 sets of deviation scores for both the patients and the healthy controls in the testing set. Our subsequent analysis was based on these independently derived deviation scores in the HCs (HC_{test}) and cases (patients with the three brain disorders). Notably, these disease-related deviations were obtained based on the sex-stratified normative growth model.

Please cite this article in press as: Liang et al., Dissecting human cortical similarity networks across the lifespan, Neuron (2025), https://doi.org/10.1016/j.neuron.2025.06.018

(ii) Stability of deviation scores across 100 repetitions

To quantitatively assess the similarity between the estimated growth curves in 100 distinct normative models and the curves in the main results, we sampled 80 points at 1-year intervals for each growth curve and calculated Pearson's correlation coefficients between the corresponding curves (Figure S6B; Tables S4 and S5). The curves of all the metrics demonstrated a high degree of similarity to the curve of the main results (mean $r > 0.95$, mean MSE $< 8.6\times10^{-8}$). To evaluate the stability of the individual deviations, we computed the pairwise Pearson's correlation coefficients and MSEs of the deviation scores among 100 distinct models. The results indicated a high degree of stability in the estimates of the individual deviations for patients within specific disease cohorts (mean $r > 0.97$, mean MSE < 0.09 for all metrics).

(iii) Individual heterogeneity of deviations

Extreme deviations were defined as $z > |2.6|$ (corresponding to a $p < 0.005$), which is consistent with the criteria used in previous studies.[49,151] The numbers of total, positive, and negative extreme deviation metrics were calculated for each patient. To quantify the percentage of extreme deviations within each disease group, we averaged the 100 sets of deviation scores for patients in each group and assessed the extreme deviations for each metric. The percentage map of extreme deviations indicated substantial individual heterogeneity within each disease group.

(iv) Case-control differences between patients and their matched HCs

The numbers of total, positive, and negative extreme deviation metrics of the patients were compared to those of their matched HCs. For each metric, the significance of the median differences between the patients and HCs was assessed with the Mann-Whitney U test. p values were adjusted for multiple comparisons with Benjamini-Hochberg FDR correction across all possible pairwise tests ($p < 0.05$). For each metric, the case-control difference analysis was repeated 100 times. The proportion of tests that passed the significance threshold out of the 100 comparisons is reported.

(v) Predictions of clinical scores on the basis of network-based deviations

Using SVR with a linear kernel, we sought to assess the ability of the morphometric network-based deviations to predict the clinical scores of patients. Each participant's deviation pattern was averaged across 100 repetitions. A two-fold cross-validation framework was implemented to estimate the prediction accuracy. Each fold alternately served as the training or test set. To mitigate the impact of features with greater numeric ranges, we normalized each feature in the training set and applied the resulting parameters to the testing set. The final predictive performance was quantified with Pearson's correlation coefficients between the predicted and observed clinical scores. The statistical significance of the prediction accuracy was evaluated through the nonparametric permutation (1,000 times). During each permutation, the observed scores of the patients were randomly shuffled prior to implementing SVR and cross-validation. This process yielded a null distribution of the correlation coefficients, and the p value was computed. The codes for the prediction analysis were modified from Cui and Gong[152] (https://github.com/ZaixuCui/Pattern_Regression_Matlab) and libsvm software (www.csie.ntu.edu.tw/∼cjlin/libsvm/).

QUANTIFICATION AND STATISTICAL ANALYSIS

Statistical analysis

Statistical analyses were performed with R (v4.2.0) and MATLAB (R2018b). Significance was defined as a p value < 0.05, with FDR-corrected p values used for multiple comparisons. Tests used are detailed in corresponding figure legends and results.

Normative growth modeling of the morphometric brain network

In line with the recommendations of the World Health Organization,[38] GAMLSS models were used to establish normative reference curves of the brain network phenotypes.[4,34,153] The growth rate of each network phenotype was obtained by calculating the first derivatives of the corresponding normative growth curve.

(i) Model distributions

We assessed a set of GAMLSS distribution families, each with three or four parameters (i.e., μ, σ, ν, τ).[153] To determine the most suitable distribution, we fitted GAMLSSs with different distributions to three global brain phenotypes, including the global variance of the morphometric network, the global mean of the morphometric network, and the whole-brain morphology−function coupling. The optimal distribution was evaluated on the basis of global brain phenotypes, as they are likely to be more reliable and less noisy than regional-level phenotypes.[4,34,153] The optimal distribution was identified as the model with the lowest Bayesian Information Criterion (BIC) among the converged models. Although the optimal distribution differed across different phenotypes, the Johnson's Su (JSU) distribution generally demonstrated better fit performance than the other distributions across all three phenotypes (Figure S7A). This distribution was also shown to be the most appropriate for brain functional phenotypes in our previous study.[34]

(ii) GAMLSS fitting

We used a GAMLSS with a JSU distribution to estimate the normative growth curves for each phenotype in healthy participants. The JSU distribution has four parameters, including the median (μ), coefficient of variation (σ), skewness (υ), and kurtosis (τ). For each morphometric network metric (denoted by *y*), the model was defined as follows:

$$
\begin{gathered}
y = \text{JSU}\ (\mu, \sigma, v, \tau), \\
\mu = f_\mu(\text{ age }) + \beta_\mu^1(\text{ sex }) + \beta_\mu^2(\textit{Euler number}) + z_\mu(\text{ site }), \\
\sigma = f_\sigma(\text{ age }) + \beta_\sigma(\text{ sex }), \\
v = \beta_v \\
\tau = \beta_\tau
\end{gathered}
$$

Where the morphometric network metric is the dependent variable, with age included as a smoothing term, sex and the Euler number as covariates, and scanner site as a random effect. To evaluate the effectiveness of the GAMLSS models in correcting for site effects, we performed one-way ANOVA analyses on three global network features from the ABCD cohort—a demographically harmonized multisite dataset. As shown in Figure S8, the uncorrected data exhibited significant site-related differences across all three features (all $p_{\text{Anova}} < 10^{-16}$), whereas the GAMLSS models effectively mitigated these site effects (all $p_{\text{Anova}} > 0.05$).

In line with the methods in a previous study,[34] for each phenotype, we fitted GAMLSSs with three degrees of freedom (df = 3-5) for the B-spline basis functions in the location (μ) parameters. For the scale (σ) parameters, the degree of freedom was set as the default value (df = 3). We included only an intercept term for the ν and τ parameters.[4,34,153] For each model, the maximum number of iteration cycles was set to 200, and the default convergence criterion (log-likelihood difference = 0.001) was used. The optimal model for each metric was identified as that which presented with the lowest BIC value among all the converged models. This flexible statistical modeling approach allowed us to map age-related growth patterns in network phenotypes, represented by the μ parameter, and to capture inter-individual variability in these phenotypes over time, represented by the σ parameter. All metrics successfully converged in our study.

(iii) Model evaluation

To evaluate the goodness of fit, we initially employed two standard diagnostic methods to check the model residuals. First, we generated four statistical plots: residuals against the fitted values of μ, residuals against the index, a kernel density estimate of the residuals, and a normal quantile-quantile (Q-Q) plot. The residuals behave well across all models (Figure S7B), reflected by their even distribution around the zero line when plotted against both the fitted μ values and the observation index. Additionally, the kernel density estimate suggested that the residuals were approximately normally distributed, and the Q-Q plot showed a nearly straight line with a zero intercept and a slope of one. Second, we used the detrended transformed Owen's plots (DTOP)[154] to assess the adequacy of the GAMLSSs. This method creates a nonparametric confidence interval for the true distribution. As shown in the DTOP plots in Figure S7B, the zero horizontal line was contained within the confidence interval, indicating that the residuals followed a normal distribution.

In addition, to further quantitatively assess model fitting, we divided the data into training and test sets. All healthy participants were randomly split into two halves, stratified by age and scanner site. For the morphometric metrics, one subgroup consisted of 17,071 individuals and the other consisted of 16,866 individuals, whereas for morphology-function coupling metrics, the subgroups comprised 16,445 and 16,442 individuals, respectively. The groups alternately served as the training and testing sets. Normative models were established with the training set, and out-of-sample metrics were calculated in the testing set. The R-squared (R^2) of the central tendency was first calculated. The centile calibration was subsequently evaluated via randomized *Z* scores.[150] Ideally, if the modeled distribution closely matches the observed distribution, the randomized *Z* scores should conform to a normal distribution. We assessed their normality with the Shapiro-Wilk test,[155] where W values near 1 indicate a better fit to normality. We found that the Shapiro-Wilk W values were consistently above 0.99 for all phenotypes. Additionally, we examined skewness and kurtosis, with skewness values close to 0 reflecting more symmetrical residuals and kurtosis values near 0 indicating a well-behaved distribution with light tails[156] (Figure S7C).

(iii) Sex differences across the lifespan

To evaluate sex differences in the phenotypes of the morphometric networks, we obtained the μ coefficients, T values, and *p* values for the sex variable using the *summary* function in R. To avoid the influence of brain volume, the total intracranial volume (TIV) was also included as a covariate in the GAMLSS in this analysis. We measured spatial correlations between the brain maps from the refitted models and the maps from the main results at each corresponding time point (with intervals of 0.01 years). High correlations were observed, with all correlation coefficients exceeding 0.98 across the lifespan. Next, the μ coefficients represent the adjusted mean effect of sex on the morphometric network phenotypes after accounting for age, the Euler number, and TIV as control variables, and the scanner site as a random effect.

Sensitivity analysis of the normative models

To evaluate the robustness of the lifespan growth patterns, we employed the following analyses.

Please cite this article in press as: Liang et al., Dissecting human cortical similarity networks across the lifespan, Neuron (2025), https://doi.org/10.1016/j.neuron.2025.06.018

(i) Bootstrap resampling analysis

To assess the robustness and determine the confidence intervals of each lifespan growth curve, we conducted 1,000 bootstrap resampling analyses, stratified by age and sex to preserve the distribution characteristics of the original participants. For each phenotype's 50th percentile growth curve, we generated 1,000 replicates and calculated the 95% confidence intervals (CIs) on the basis of the mean and standard deviation across all iterations.

(ii) Split-half replication analysis

To evaluate the replicability of the GAMLSSs across independent datasets, we employed a split-half strategy. All healthy participants were randomly split into two halves, stratified by age and scanner site. For mapping the growth of the morphometric network, one half consisted of 17,071 individuals and the other of 16,866 individuals, whereas for mapping the growth of morphometric–function coupling, the subgroups comprised 16,445 and 16,442 individuals, respectively. Lifespan normative growth patterns were then independently assessed within each subgroup.

(iii) Leave-one-site-out (LOSO) analysis

To test whether the lifespan growth curves were influenced by data from specific sites, we performed LOSO analyses. We iteratively excluded one site from the dataset and re-estimated the GAMLSSs. The 95% CIs for the LOSO normative growth curves and growth rates were calculated on the basis of the mean and standard deviation across all iterations. The resulting CIs were narrow, indicating that the robustness of our main results was high.

(iv) Balanced resampling analysis (strategy I)

To determine whether the changes in the morphometric network-based metrics were influenced by the imbalance in sample size across different age groups, we adopted a balanced resampling strategy, ensuring that the number of participants was relatively consistent across age groups. All participants were divided into 16 age groups with 5-year intervals, and the number of participants in each group was recorded. Given that most metrics in our study exhibited significant changes during the first 30 years of life, we defined the baseline for balanced resampling on the basis of the minimum number of participants ($n_{\text{participant}}$) in the first six age bins (0-30 years). All other age groups were randomly sampled according to this standard. Within each age group, we further divided participants into five sub-bins at 1-year intervals and ensured that the number of participants in each sub-bin was as equal as possible during resampling. If the number of participants in a given age bin was less than $n_{\text{participant}}$, all participants in this bin were selected. After resampling, data for 12,414 individuals were used to calculate morphometric metrics, and data for 8,071 individuals were used to calculate morphology–function coupling. The distribution of participants after resampling is shown in Tables S7 and S8. This resampling procedure was repeated 1,000 times, and the GAMLSS models were refitted for each iteration. We then calculated the 95% CIs on the basis of the mean and standard deviation across all iterations. Additionally, we assessed the correlations between the 1,000 median (50th) centile curves and the median centile curve derived from the entire cohort.

(v) Balanced resampling analysis (strategy II)

To determine whether the changes in the morphometric network-based metrics were influenced by the imbalance in sample size and the number of scanner sites across different age groups, we adopted a balanced resampling strategy, ensuring that the number of participants and sites was relatively consistent across age groups, which aligns with our previous study.[34] All participants were divided into 16 age groups with 5-year intervals, and the number of participants and scanning sites for each age group were recorded. Given that most metrics in our study exhibited significant changes during the first 30 years of life, we defined the baseline for balanced resampling on the basis of the minimum number of participants ($n_{\text{participant}}$) and the minimum number of sites (n_{site}) in the first six age bins (0–30 years). All other age groups were randomly sampled according to this standard. If the number of participants in a particular age bin was less than $n_{\text{participant}}$, data from the top n_{site} centers with the most participants were selected. After resampling, 11,114 individuals were included for calculating morphometric metrics, and 7,555 individuals were included for calculating morphology–function coupling. The distribution of participants and sites after resampling is shown in Tables S7 and S8. This resampling procedure was repeated 1,000 times, and the GAMLSS models were refitted for each iteration. We then calculated the 95% CIs on the basis of the mean and standard deviation across all iterations. Additionally, we assessed the correlations between the 1,000 median (50th) centile curves and the median centile curve derived from the entire cohort.

(vi) Cortical parcellation validation

To investigate whether the lifespan growth curves were stable under different parcellation resolutions,[157] we replicated the growth curves using all healthy participants by parcellating their cortex into 219 cortical brain regions. GAMLSS models for each metric were then re-estimated at the global, cytoarchitectonic-class, and regional levels.

(vii) Leave-one-feature-out analysis

To assess the MIND stability of the morphometric similarity estimation, we reconstructed the morphometric network for each participant by removing one feature at a time. We re-estimated the growth curves of each four-feature network using the data from all healthy participants and then assessed the spatial correlations between the four-feature and original five-feature MSS maps.

ADDITIONAL RESOURCES

ABCD: data used in the preparation of this article were obtained from the Adolescent Brain Cognitive Development (ABCD) Study (https://abcdstudy.org), held in the NIMH Data Archive (NDA). This is a multisite, longitudinal study designed to recruit more than 10,000 children age 9–10 and follow them over 10 years into early adulthood. The ABCD Study® is supported by the National

Institutes of Health and additional federal partners under award numbers U01DA041048, U01DA050989, U01DA051016, U01DA041022, U01DA051018, U01DA051037, U01DA050987, U01DA041174, U01DA041106, U01DA041117, U01DA041028, U01DA041134, U01DA050988, U01DA051039, U01DA041156, U01DA041025, U01DA041120, U01DA051038, U01DA041148, U01DA041093, U01DA041089, U24DA041123, U24DA041147. A full list of supporters is available at https://abcdstudy.org/federal-partners.html. A listing of participating sites and a complete listing of the study investigators can be found at https://abcdstudy.org/consortium_members/. ABCD consortium investigators designed and implemented the study and/or provided data but did not necessarily participate in the analysis or writing of this report. This manuscript reflects the views of the authors and may not reflect the opinions or views of the NIH or ABCD consortium investigators. The ABCD data repository grows and changes over time. The ABCD data used in this report came from https://nda.nih.gov/edit_collection.html?id=3165, shared by the DCAN Labs ABCD-BIDS Community Collection (ABCC) (Collection Investigators: Damien Fair).

ABIDE I: primary support for the work by Adriana Di Martino was provided by the (NIMH K23MH087770) and the Leon Levy Foundation. Primary support for the work by Michael P. Milham and the INDI team was provided by gifts from Joseph P. Healy and the Stavros Niarchos Foundation to the Child Mind Institute, as well as by an NIMH award to MPM (NIMH R03MH096321).

ABIDE II: primary support for the work by Adriana Di Martino and her team was provided by the National Institute of Mental Health (NIMH 5R21MH107045). Primary support for the work by Michael P. Milham and his team provided by the National Institute of Mental Health (NIMH 5R21MH107045); Nathan S. Kline Institute of Psychiatric Research). Additional Support was provided by gifts from Joseph P. Healey, Phyllis Green and Randolph Cowen to the Child Mind Institute.

ADNI: Data used in preparation of this article were obtained from the Alzheimer's Disease Neuroimaging Initiative (ADNI) database (adni.loni.usc.edu). As such, the investigators within the ADNI contributed to the design and implementation of ADNI and/or provided data but did not participate in analysis or writing of this report. A complete listing of ADNI investigators can be found at: http://adni.loni.usc.edu/wp-content/uploads/how_to_apply/ADNI_Acknowledgement_List.pdf. Data collection and sharing for this project was funded by the Alzheimer's Disease Neuroimaging Initiative (ADNI) (National Institutes of Health Grant U01 AG024904) and DOD ADNI (Department of Defense award number W81XWH-12-2-0012). ADNI is funded by the National Institute on Aging, the National Institute of Biomedical Imaging and Bioengineering, and through generous contributions from the following: AbbVie, Alzheimer's Association; Alzheimer's Drug Discovery Foundation; Araclon Biotech; BioClinica, Inc.; Biogen; Bristol-Myers Squibb Company; CereSpir, Inc.; Cogstate; Eisai Inc.; Elan Pharmaceuticals, Inc.; Eli Lilly and Company; EuroImmun; F. Hoffmann-La Roche Ltd and its affiliated company Genentech, Inc.; Fujirebio; GE Healthcare; IXICO Ltd.;Janssen Alzheimer Immunotherapy Research & Development, LLC.; Johnson & Johnson Pharmaceutical Research & Development LLC.; Lumosity; Lundbeck; Merck & Co., Inc.; Meso Scale Diagnostics, LLC.; NeuroRx Research; Neurotrack Technologies; Novartis Pharmaceuticals Corporation; Pfizer Inc.; Piramal Imaging; Servier; Takeda Pharmaceutical Company; and Transition Therapeutics. The Canadian Institutes of Health Research is providing funds to support ADNI clinical sites in Canada. Private sector contributions are facilitated by the Foundation for the National Institutes of Health (www.fnih.org). The grantee organization is the Northern California Institute for Research and Education, and the study is coordinated by the Alzheimer's Therapeutic Research Institute at the University of Southern California. ADNI data are disseminated by the Laboratory for Neuro Imaging at the University of Southern California.

BCP: data used herein is supported by NIH grant (1U01MH110274) and the efforts of the UNC/UMN Baby Connectome Project Consortium.

dHCP: data were provided by the developing Human Connectome Project, KCL-Imperial-Oxford Consortium funded by the European Research Council under the European Union Seventh Framework Programme (FP/2007-2013) / ERC Grant Agreement no. [319456]. We are grateful to the families who generously supported this trial.

HCP: data were provided by the Human Connectome Project, WU-Minn Consortium (Principal Investigators: David Van Essen and Kamil Ugurbil; 1U54MH091657) funded by the 16 NIH Institutes and Centers which support the NIH Blueprint for Neuroscience Research; and by the Mc-Donnell Center for Systems Neuroscience at Washington University.

HCP Lifespan: data used in this publication was supported by the National Institute of Mental Health of the National Institutes of Health under Award Number U01MH109589 and by funds provided by the McDonnell Center for Systems Neuroscience at Washington University in St. Louis. The content is solely the responsibility of the authors and does not necessarily represent the official views of the National Institutes of Health.

NKI-RS: funding for key personnel provided in part by the New York State Office of Mental Health and Research Foundation for Mental Hygiene. Additional project support provided by the NKI Center for Advanced Brain Imaging (CABI), the Brain Research Foundation (Chicago, IL), the Stavros Niarchos Foundation, and NIH grant P50 MH086385-S1.

NSPN: the NSPN study was funded by a Wellcome Trust award to the University of Cambridge and the University College London.
UK Biobank: this research has been conducted using data from UK Biobank (www.ukbiobank.ac.uk). UK Biobank is generously supported by its founding funders the Wellcome Trust and UK Medical Research Council, as well as the Department of Health, Scottish Government, the Northwest Regional Development Agency, British Heart Foundation, and Cancer Research UK.

Neuron, Volume *113*

Supplemental information

Dissecting human cortical similarity networks across the lifespan

Xinyuan Liang, Lianglong Sun, Mingrui Xia, Tengda Zhao, Gaolang Gong, Qiongling Li, Xuhong Liao, Zaixu Cui, Dingna Duan, Chenxuan Pang, Qian Wang, Qian Yu, Yanchao Bi, Pindong Chen, Rui Chen, Yuan Chen, Taolin Chen, Jingliang Cheng, Yuqi Cheng, Zhengjia Dai, Yao Deng, Yuyin Ding, Qi Dong, Jia-Hong Gao, Qiyong Gong, Ying Han, Zaizhu Han, Chu-Chung Huang, Ruiwang Huang, Ran Huo, Lingjiang Li, Ching-Po Lin, Qixiang Lin, Bangshan Liu, Chao Liu, Ningyu Liu, Ying Liu, Yong Liu, Jing Lu, Leilei Ma, Weiwei Men, Shaozheng Qin, Wen Qin, Jiang Qiu, Shijun Qiu, Tianmei Si, Shuping Tan, Yanqing Tang, Sha Tao, Dawei Wang, Fei Wang, Jiali Wang, Jinhui Wang, Pan Wang, Xiaoqin Wang, Yanpei Wang, Dongtao Wei, Yankun Wu, Peng Xie, Xiufeng Xu, Yuehua Xu, Zhilei Xu, Liyuan Yang, Chunshui Yu, Huishu Yuan, Zilong Zeng, Haibo Zhang, Xi Zhang, Gai Zhao, Yanting Zheng, Suyu Zhong, Alzheimer's Disease Neuroimaging Initiative, MCADI, DIDA-MDD Working Group, and Yong He

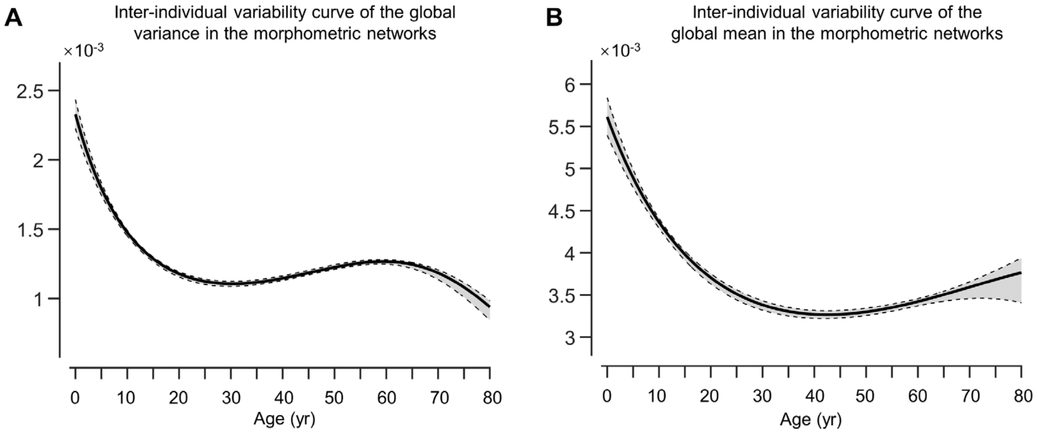

Figure S1. Inter-individual variability in the global variance and global mean of the morphometric networks, related to Figure 2. (A) Inter-individual variability curves for global variance in the morphometric networks. (B) Inter-individual variability curves for global mean in the morphometric networks. The solid line (median) represents the 50% centile, with 95% confidence intervals (shaded in gray) estimated through bootstrapping with 1,000 resamples. yr, year.

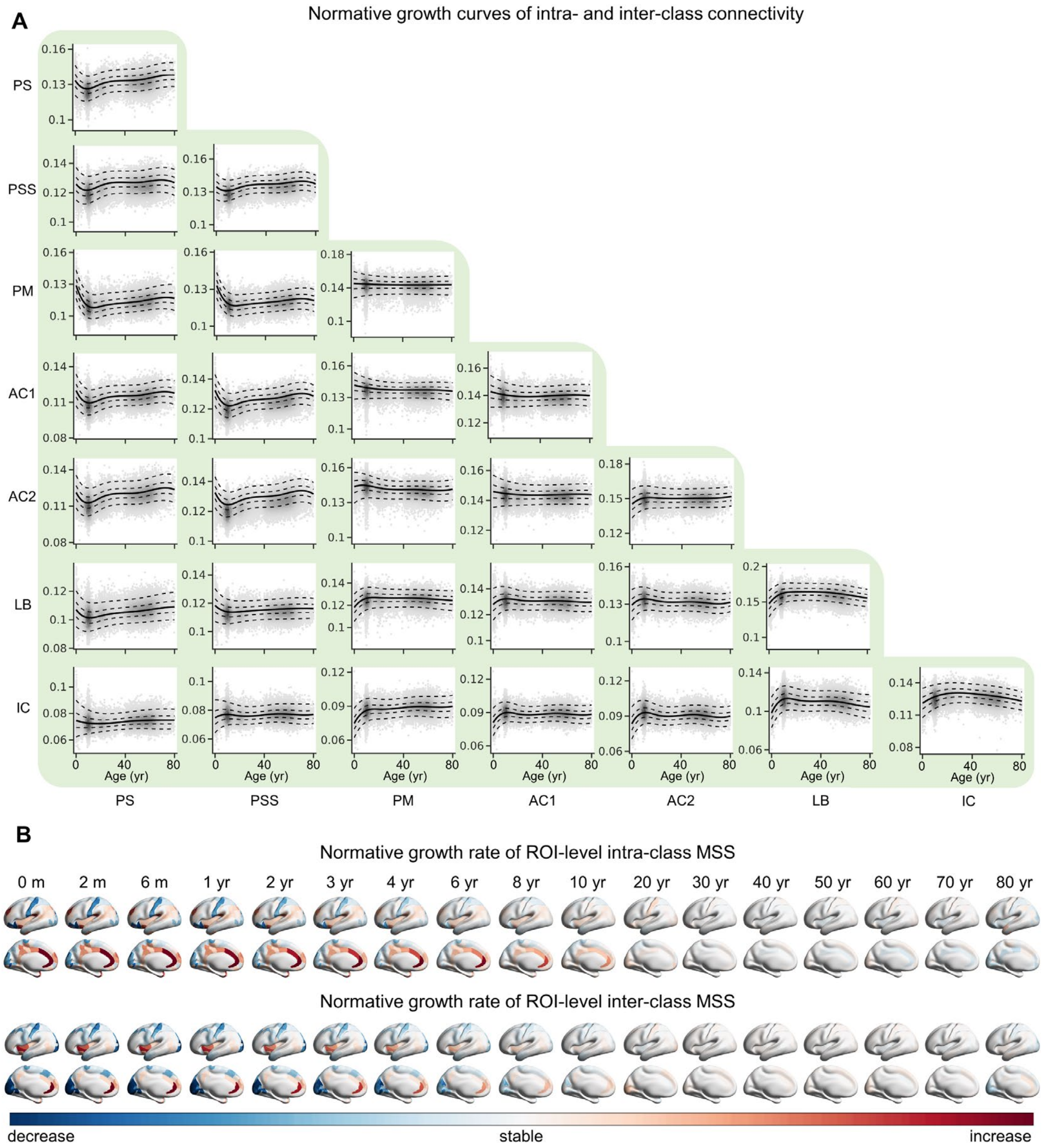

Figure S2. Normative growth of intra- and inter-class connectivity across the lifespan, related to Figures 3 and 4. (A) Normative growth curves of the morphometric networks at the cortical cytoarchitectonic class level across the human lifespan. The solid line (median) represents the 50% centile, and the dotted lines represent the 5%, 25%, 75%, and 95% centiles. (B) Surface maps of the growth rate of regional-level intra- and inter-class MSS. m, month; yr, year; PS, primary sensory cortex; PSS, primary/secondary sensory cortex; PM, primary motor cortex; AC1, association cortex I, AC2, association cortex II; LB, limbic region; IC, insular cortex; MSS, morphometric similarity strength.

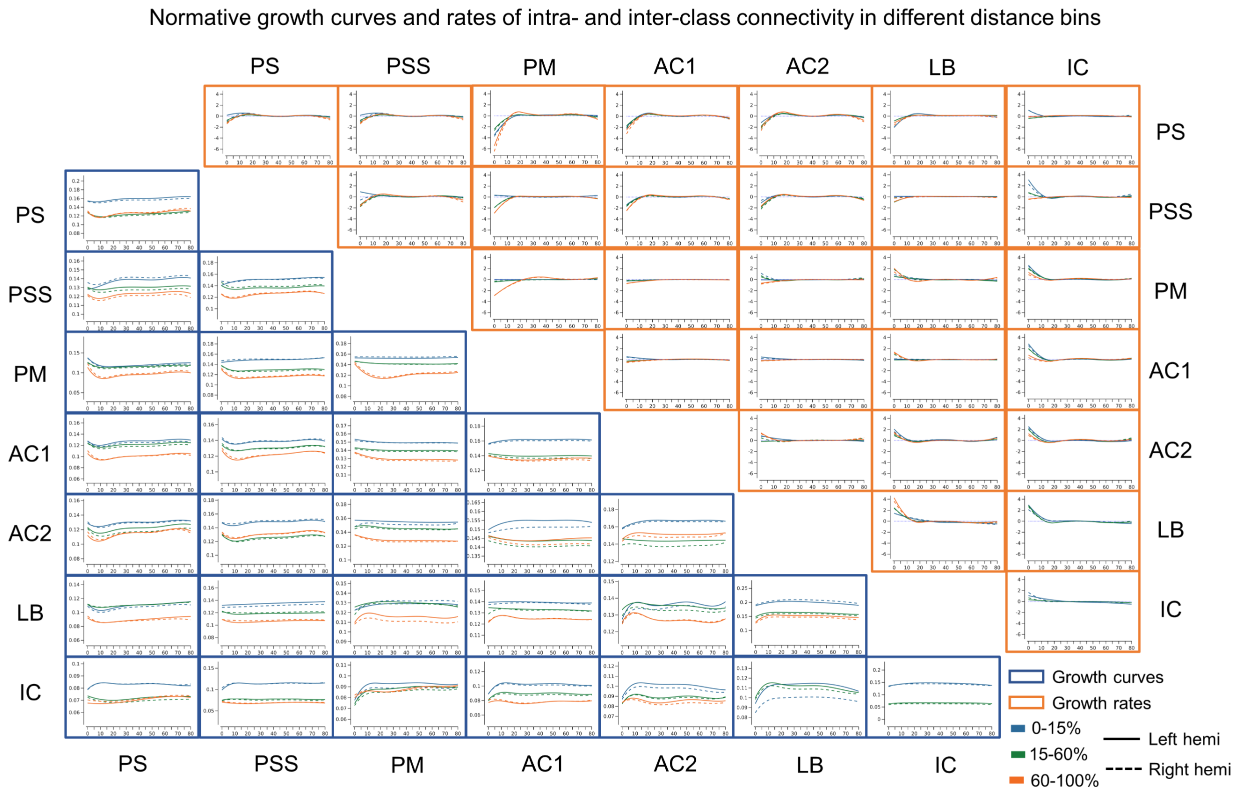
Normative growth curves and rates of intra- and inter-class connectivity in different distance bins

Figure S3. Lifespan growth curves and growth rates of the morphometric networks at the cytoarchitectonic class level across different distance bins, related to Figure 3. The plot shows the growth curves and rates for the 50th percentile of intra- and inter-class mean connectivity are shown. PS, primary sensory cortex; PSS, primary/secondary sensory cortex; PM, primary motor cortex; AC1, association cortex I; AC2, association cortex II; LB, limbic region; IC, insular cortex.

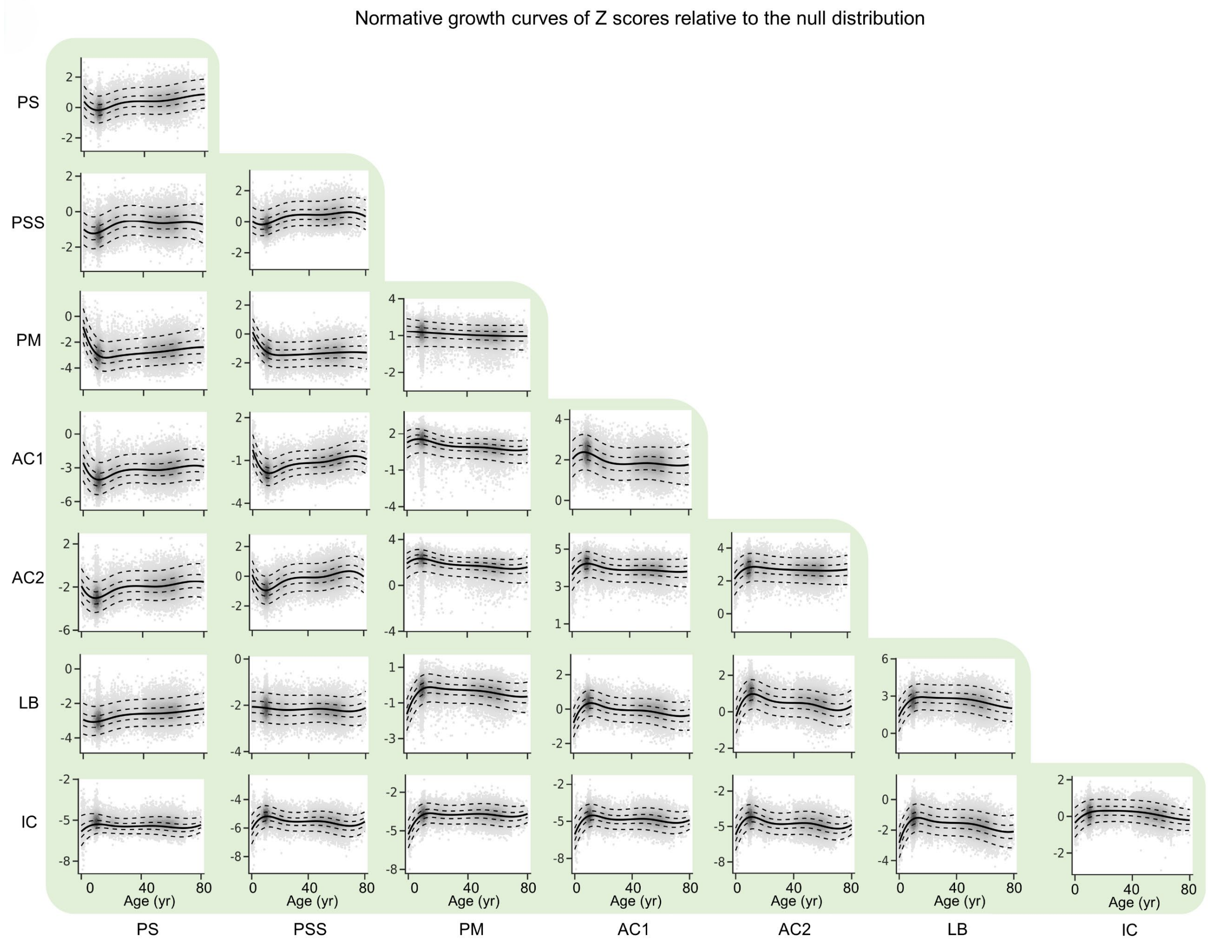

Figure S4. Normative growth curves of the Z scores relative to the null distribution at the cortical cytoarchitectonic class level across the human lifespan, related to Figure 3. To establish the baseline for MSS at the cytoarchitectonic class level, we shuffled the node labels for each participant's morphometric network while preserving spatial autocorrelation. This process generated 10,000 random morphometric networks, from which we derived the null distribution for both intra-class and inter-class connectivity. Each participant's connectivity was expressed as Z scores relative to these null distributions. The solid line (median) represents the 50% centile, and the dotted lines represent the 5%, 25%, 75%, and 95% centiles. yr, year; PS, primary sensory cortex; PSS, primary/secondary sensory cortex; PM, primary motor cortex; AC1, association cortex I, AC2, association cortex II; LB, limbic region; IC, insular cortex.

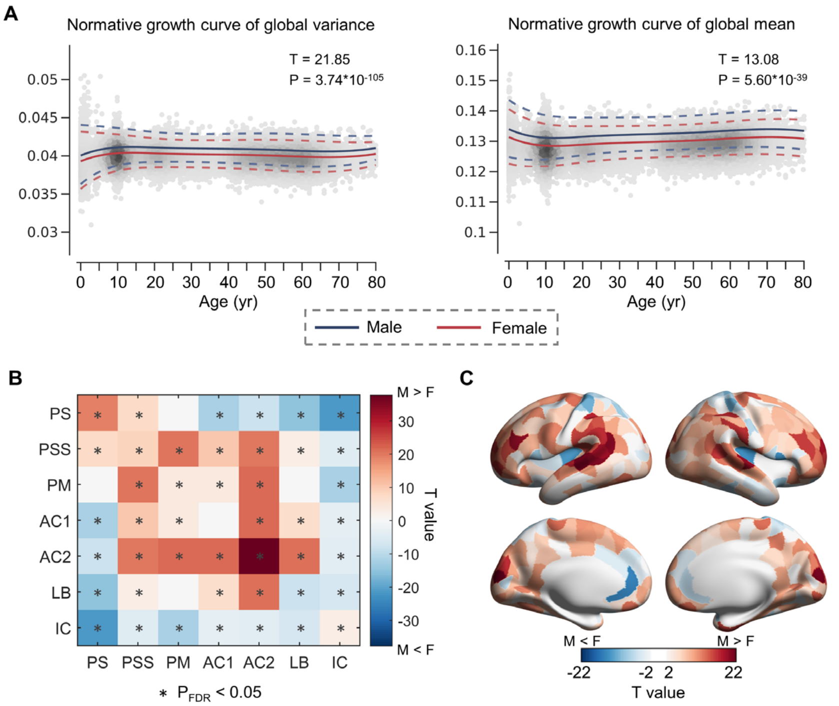

Figure S5. Sex differences in the morphometric brain networks, related to STAR Methods. (A) Sex-stratified growth curves for the global variance of the morphometric network (left panel) and the global mean of the morphometric network (right pane;). The solid line represents the 50% centile, with the two surrounding dotted lines represent the 5% and 95% centiles. (B) Sex differences (T values) in the morphometric network at the cortical cytoarchitectonic class level. Blue indicates greater connectivity strength in females than in males, while red indicates greater connectivity strength in males than in females. Asterisks denote a significance level at $P_{FDR} < 0.05$ ($P = 0.016$, FDR corrected). (C) Sex differences in the morphometric network at the regional level. Statistically significant differences are shown in blue or red ($P = 0.038$, FDR corrected). yr, year; PS, primary sensory cortex; PSS, primary/secondary sensory cortex; PM, primary motor cortex; AC1, association cortex I, AC2, association cortex II; LB, limbic region; IC, insular cortex; M, male; F, female.

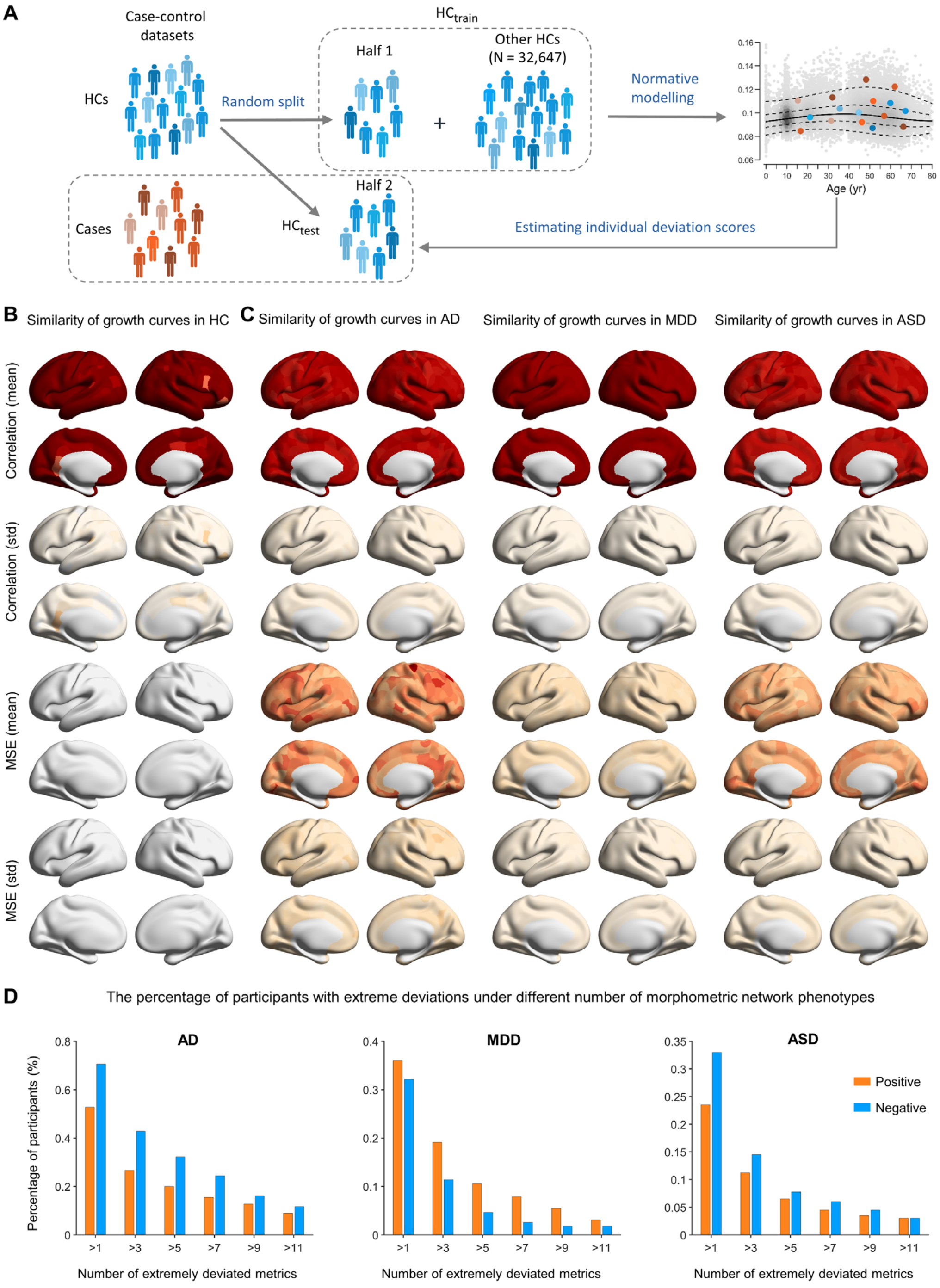

Figure S6. Normative modeling and deviation analysis across clinical groups, related to STAR Methods. (A) Schematic overview of normative modelling for patients. (B) Similarity between the curves estimated from 100 repeatedly constructed normative models using different sets of healthy controls and the curves from the main analysis. (C) Similarity between the deviation scores from 100 repeatedly constructed normative models and the deviation scores from the main analysis in AD patients, MDD patients, and ASD patients. Both the normative curves and the patients' deviation scores exhibited a high degree of stability across the 100 repetitions (average $r > 0.95$ and average mean squared error [MSE] < 0.09 for all metrics). (D) Bar plots show the percentage of participants with extreme deviations across different numbers of morphometric network phenotypes in AD (left panel), MDD (middle panel), and ASD (right panel).

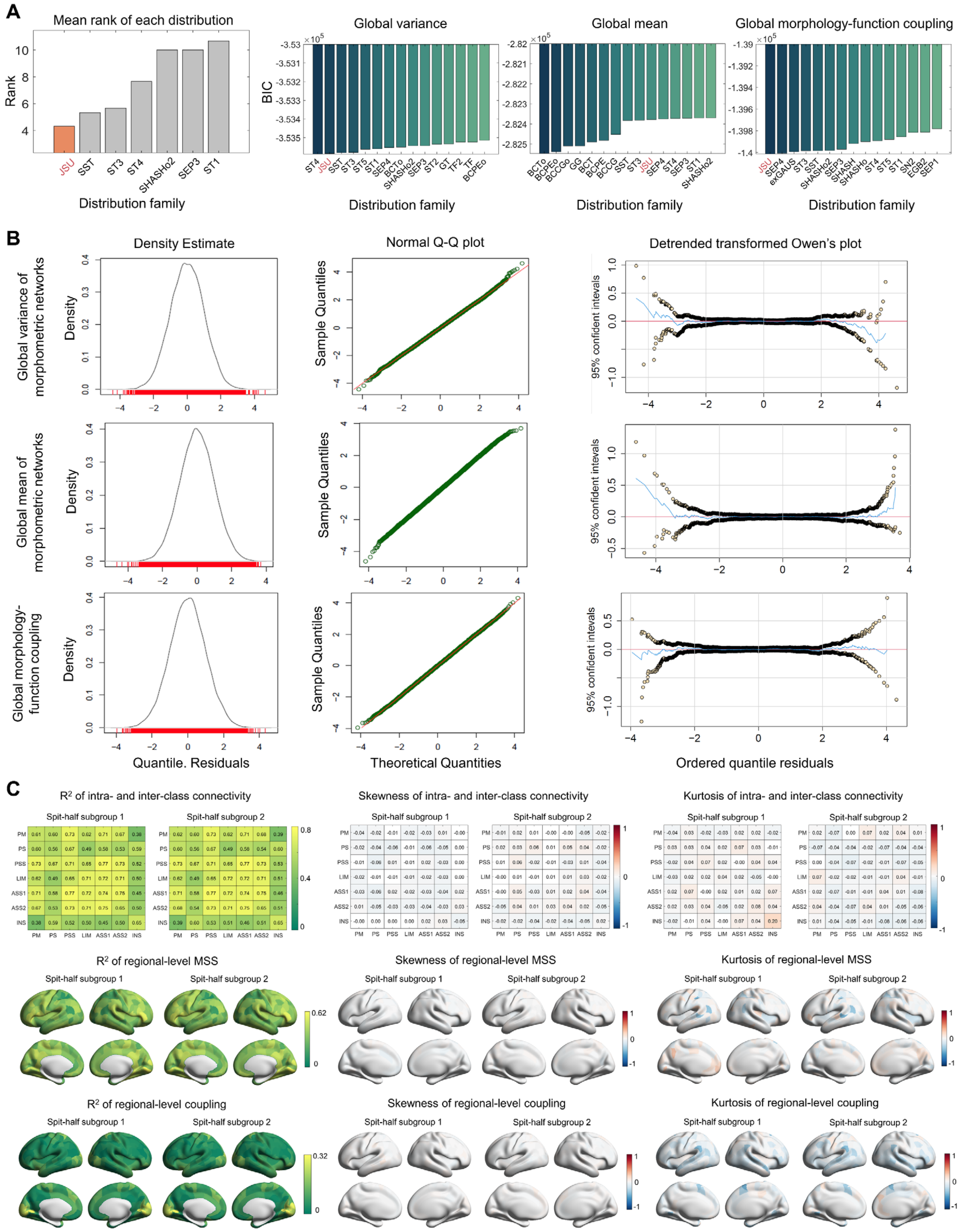

Figure S7. Model selection, evaluation, and goodness of fit for normative modeling, related to STAR Methods. (A) Selection of model distribution. (B) Model evaluation. Kernel density plots of residuals, Q-Q plots, and detrended transformed Owen's plots are shown for three global brain phenotypes. (C) Goodness of fit of normative model. R-squared (R^2), skewness, and kurtosis values of the normative model of intra- and inter-class morphometric similarity, the regional-level MSS, and regional-level coupling. MSS, morphometric similarity strength.

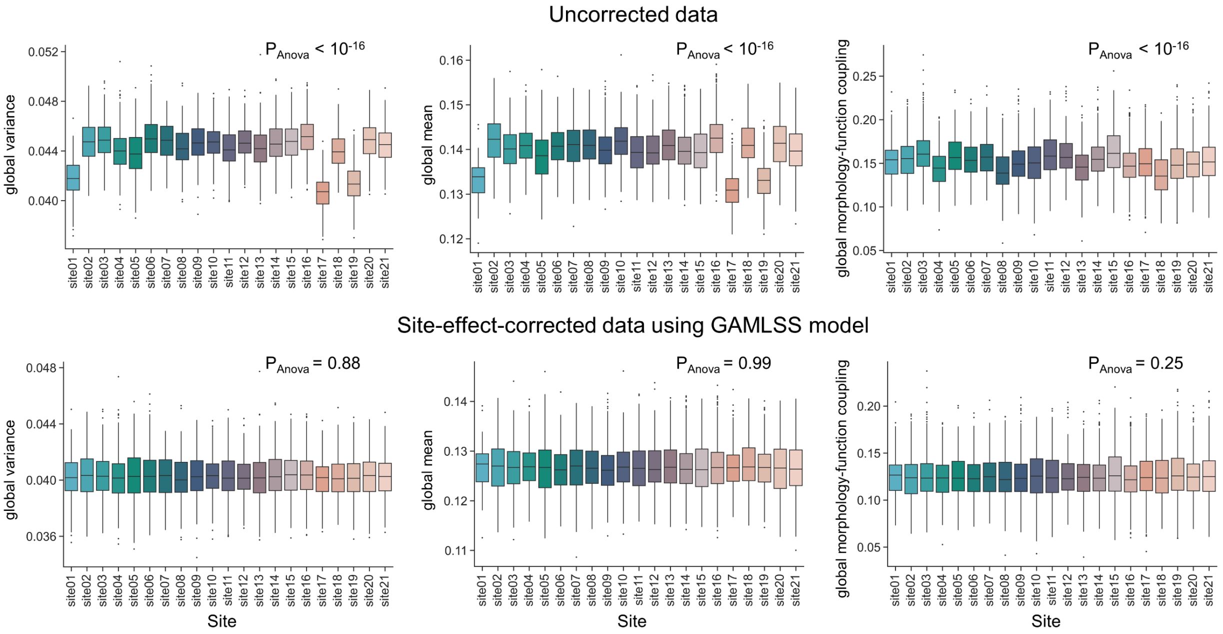

Uncorrected data

Site-effect-corrected data using GAMLSS model

Figure S8. Effectiveness of GAMLSS in correcting for site effects, related to STAR Methods. Box plots illustrating site-related differences before (top panels) and after GAMLSS-based correction (bottom panels) in three global network features. Each box represents the distribution of values in a given site.

Supplementary Tables

Table S1. Sample description, related to Figure 1.

Research aims	Dataset	Modality	N (subjects)	N (sites)	Age range (years)	Sex (F)
Aim 1: Mapping of morphometric brain network over the human lifespan	All set (healthy)	sMRI	33,937	141	0-80	53.7%
Aim 2: Mapping of morphology−function coupling over the human lifespan	Subset (healthy)	sMRI, fMRI	32,887	131	0-80	53.9%
Aim 3: Clinical relevance of normative models of morphometric brain networks	Training set (healthy)	sMRI	33,288	141	0-80	53.8%
	Testing set (healthy)	sMRI	649	23	6-80	45.9%
	AD	sMRI	180	5	51-80	58.9%
	MDD	sMRI	622	5	11-77	59.2%
	ASD	sMRI	400	13	5-59	14.3%

AD, Alzheimer's disease; MDD, major depressive disorder; ASD, autism spectrum disorder; fMRI, functional MRI; sMRI, structural MRI; F, female.

Table S4. Stability of growth curves and deviation scores according to Pearson's correlation coefficient based on 100 normative models, related to STAR Methods.

Metric	**Similarity of growth curves**		**Similarity of deviation score in AD**		**Similarity of deviation score in MDD**		**Similarity of deviation score in ASD**	
	R (mean)	**R (std)**	**R (mean)**	**R (std)**	**R (mean)**	**R (std)**	**R (mean)**	**R (std)**
Global variance of the connectome	1	7.4E-04	0.99	0.005	0.99	0.002	0.98	0.003
Global mean of the connectome	1	3.2E-04	0.99	0.004	1	0.002	0.98	0.004
Within the PS system	1	1.3E-04	0.99	0.005	1	0.002	0.98	0.003
Within the PSS system	1	1.2E-04	0.99	0.005	0.99	0.002	0.98	0.004
Within the PM system	1	1.5E-03	0.98	0.006	1	0.002	0.98	0.004
Within the AC1 system	1	4.1E-04	0.99	0.005	1	0.002	0.99	0.003
Within the AC2 system	1	2.7E-04	0.99	0.004	1	0.002	0.99	0.003
Within the LB system	1	9.1E-05	0.99	0.005	0.99	0.003	0.98	0.004
Within the IC system	1	6.1E-05	0.98	0.006	0.99	0.002	0.98	0.004
Between the PM and PS systems	1	9.1E-05	0.99	0.005	1	0.002	0.98	0.004
Between the PM and PSS systems	1	1.5E-04	0.99	0.004	1	0.002	0.98	0.004
Between the PM and LB systems	1	2.4E-04	0.98	0.005	0.99	0.002	0.98	0.003
Between the PM and AC1 systems	1	7.4E-05	0.98	0.005	1	0.002	0.98	0.003
Between the PM and AC2 systems	1	3.3E-04	0.99	0.004	1	0.001	0.98	0.003
Between the PM and IC systems	1	6.2E-05	0.98	0.006	1	0.002	0.98	0.004
Between the PS and PSS systems	1	3.2E-04	0.98	0.006	0.99	0.002	0.98	0.004
Between the PS and LB systems	1	2.7E-04	0.99	0.003	0.99	0.002	0.98	0.004
Between the PS and AC1 systems	1	1.7E-04	0.99	0.003	0.99	0.002	0.98	0.004
Between the PS and AC2 systems	1	1.3E-04	0.99	0.003	0.99	0.002	0.98	0.004
Between the PS and IC systems	0.99	1.7E-03	0.99	0.003	1	0.002	0.97	0.006
Between the PSS and LB systems	1	5.4E-04	0.99	0.005	0.99	0.002	0.98	0.004
Between the PSS and AC1 systems	1	9.0E-05	0.99	0.003	1	0.002	0.98	0.004
Between the PSS and AC2 systems	1	6.9E-05	0.99	0.005	1	0.002	0.98	0.004
Between the PSS and IC systems	1	2.0E-03	0.99	0.004	1	0.001	0.97	0.006
Between the LB and AC1 systems	1	3.8E-04	0.99	0.005	1	0.002	0.98	0.004
Between the LB and AC2 systems	1	2.3E-04	0.99	0.004	1	0.001	0.98	0.003
Between the LB and IC systems	1	1.2E-04	0.99	0.004	0.99	0.002	0.98	0.004
Between the AC1 and AC2 systems	1	7.7E-04	0.99	0.003	1	0.002	0.99	0.003
Between the AC1 and IC systems	1	1.4E-04	0.99	0.004	1	0.001	0.98	0.004
Between the AC2 and IC systems	1	1.6E-04	0.99	0.004	1	0.001	0.98	0.004

Abbreviations: PS, primary sensory cortex; PSS, primary/secondary sensory cortex; PM, primary motor cortex; AC1, association cortex I; AC2, association cortex II; LB, limbic region; IC, insular cortex.

Table S5. Stability of growth curves and deviation scores according to the mean squared error (MSE) based on 100 normative models, related to STAR Methods.

Metric	Similarity of growth curves		Similarity of deviation score in ASD		Similarity of deviation score in MDD		Similarity of deviation score in AD	
	MSE (mean)	MSE (std)	MSE (mean)	MSE (std)	MSE (mean)	MSE (std)	MSE (mean)	MSE (std)
Global variance of the connectome	2.8E-10	1.7E-10	0.06	0.017	0.01	0.005	0.04	0.007
Global mean of the connectome	2.4E-9	1.1E-9	0.05	0.015	0.01	0.005	0.04	0.01
Within the PS system	9.4E-9	4.0E-9	0.05	0.015	0.02	0.006	0.04	0.008
Within the PSS system	7.6E-9	2.9E-9	0.06	0.02	0.01	0.004	0.05	0.009
Within the PM system	2.5E-9	2.4E-9	0.06	0.017	0.01	0.004	0.04	0.007
Within the AC1 system	1.6E-9	1.3E-9	0.06	0.019	0.01	0.005	0.04	0.008
Within the AC2 system	2.1E-9	1.4E-9	0.05	0.014	0.01	0.005	0.03	0.007
Within the LB system	5.4E-9	4.5E-9	0.06	0.019	0.02	0.006	0.04	0.008
Within the IC system	4.4E-9	2.9E-9	0.06	0.018	0.02	0.006	0.05	0.009
Between the PM and PS systems	1.0E-8	3.7E-9	0.05	0.018	0.01	0.004	0.04	0.008
Between the PM and PSS systems	1.1E-8	3.6E-9	0.05	0.014	0.01	0.005	0.05	0.009
Between the PM and LB systems	4.3E-9	3.2E-9	0.06	0.017	0.02	0.006	0.04	0.007
Between the PM and AC1 systems	1.3E-9	1.2E-9	0.05	0.015	0.01	0.004	0.04	0.007
Between the PM and AC2 systems	2.8E-9	1.8E-9	0.04	0.013	0.01	0.004	0.04	0.007
Between the PM and IC systems	4.7E-9	2.7E-9	0.06	0.019	0.01	0.005	0.04	0.006
Between the PS and PSS systems	9.1E-9	3.3E-9	0.06	0.017	0.02	0.006	0.05	0.01
Between the PS and LB systems	7.5E-9	3.1E-9	0.04	0.011	0.02	0.006	0.05	0.011
Between the PS and AC1 systems	8.0E-9	3.4E-9	0.04	0.013	0.02	0.005	0.04	0.01
Between the PS and AC2 systems	1.0E-8	4.1E-9	0.04	0.012	0.02	0.005	0.05	0.01
Between the PS and IC systems	1.3E-8	3.9E-9	0.04	0.011	0.01	0.005	0.07	0.015
Between the PSS and LB systems	4.6E-9	1.9E-9	0.06	0.022	0.02	0.006	0.05	0.01
Between the PSS and AC1 systems	8.3E-9	2.1E-9	0.04	0.014	0.01	0.004	0.05	0.009
Between the PSS and AC2 systems	8.1E-9	2.0E-9	0.05	0.016	0.01	0.004	0.05	0.011
Between the PSS and IC systems	4.5E-9	1.7E-9	0.05	0.016	0.01	0.004	0.06	0.013
Between the LB and AC1 systems	1.9E-9	1.7E-9	0.06	0.019	0.01	0.005	0.04	0.008
Between the LB and AC2 systems	2.2E-9	1.6E-9	0.05	0.015	0.01	0.005	0.04	0.008
Between the LB and IC systems	8.4E-9	5.7E-9	0.05	0.018	0.01	0.004	0.04	0.009
Between the AC1 and AC2 systems	1.4E-9	9.1E-10	0.05	0.014	0.01	0.005	0.04	0.008
Between the AC1 and IC systems	3.5E-9	1.9E-9	0.06	0.018	0.01	0.004	0.04	0.008
Between the AC2 and IC systems	4.1E-9	2.3E-9	0.06	0.018	0.01	0.005	0.04	0.008

Abbreviations: PS, primary sensory cortex; PSS, primary/secondary sensory cortex; PM, primary motor cortex; AC1, association cortex I; AC2, association cortex II; LB, limbic region; IC, insular cortex.

Table S6. Similarity between the lifespan normative growth curves from the sensitivity analyses and the main results, related to STAR Methods.

Sensitivity analysis	**Global-level metrics**			**Class-level metrics**	**Regional-level metrics**	
	Global variance of the morphometric networks	**Global mean of the morphometric networks**	**Global morphology-functional coupling**	**Class-level MSS**	**Regional MSS**	**Regional morphology-functional coupling**
(i) Bootstrap resampling	0.97	0.99	0.99	0.99	1.00	1.00
(ii) Split-half subgroup 1	0.99	1.00	1.00	0.99	1.00	1.00
(ii) Split-half subgroup 2	0.96	0.99	1.00	0.99	1.00	1.00
(iii) Leave-one-site-out	1.00	1.00	1.00	1.00	1.00	1.00
(iv) Balanced resampling (strategy I)	0.99	0.98	0.99	0.99	1.00	1.00
(v) Balanced resampling (strategy II)	0.83	0.96	0.94	0.95	1.00	0.99
(vi) Cortical parcellation validation (DK-219)	0.80	0.95	0.98	0.95	—	—
(vii) Leave-one-feature-out (removed CT)	0.30	-0.63	0.98	0.53	0.97	0.94
(vii) Leave-one-feature-out (removed SA)	0.97	0.97	0.98	0.89	1.00	1.00
(vii) Leave-one-feature-out (removed Vol)	0.74	0.94	1.00	0.98	1.00	1.00
(vii) Leave-one-feature-out (removed MC)	0.67	0.91	1.00	0.95	0.99	0.99
(vii) Leave-one-feature-out (removed SD)	0.70	0.92	1.00	0.95	0.99	0.99

Note: For global- and class-level metrics, in the bootstrap resampling, leave-one-site-out, and balanced resampling analyses, we calculated the average similarity between the curves generated from multiple resamplings and the main result curve. For regional-level metrics, we calculated the average correlation between the brain maps from a single random sample and the maps from the main results in the bootstrap resampling and balanced resampling analyses. For the leave-one-site-out analysis, we calculated the average correlation coefficient between the brain maps of the sample after removal of the largest site (UKB1) and the brain maps from the main results. Notably, normative growth curves of global morphometric network metrics and surface maps of regional-level metrics for each sensitivity analysis are available at https://github.com/Xinyuan-Liang/Cortical_Similarity_Networks_Lifespan. MSS, morphometric similarity strength; CT, cortical thickness; SA, surface area; Vol, gray matter volume; MC, mean curvature; SD, sulcal depth.

Table S7. Distribution of samples and sites before and after balanced resampling, related to STAR Methods.

Age (year)	Before resampling		After resampling		
	Samples	Sites	Strategy I	Strategy II	
			Samples	Samples	Sites
[0,5]	944	15	907	816	15
(5,10]	4625	55	907	816	15
(10,15]	4415	64	907	816	15
(15,20]	1875	53	907	816	15
(20,25]	2277	47	907	816	15
(25,30]	907	37	907	816	15
(30,35]	635	28	635	602	15
(35,40]	457	29	457	406	15
(40,45]	2526	23	907	816	15
(45,50]	3062	25	907	816	15
(50,55]	3466	28	907	816	15
(55,60]	3937	37	907	816	15
(60,65]	3142	37	907	816	15
(65,70]	1231	53	907	816	15
(70,75]	283	45	283	207	15
(75,80]	155	41	155	107	15

Table S8. Distribution of samples and sites before and after balanced resampling (morphology–function coupling), related to STAR Methods.

Age (year)	Before resampling		After resampling		
			Strategy I	Strategy II	
	Samples	Sites	Samples	Samples	Sites
[0,5]	552	5	552	552	5
(5,10]	4321	48	552	552	5
(10,15]	4213	60	552	552	5
(15,20]	1750	49	552	552	5
(20,25]	2250	44	552	552	5
(25,30]	907	37	552	552	5
(30,35]	635	28	552	477	5
(35,40]	457	29	457	272	5
(40,45]	2526	23	552	552	5
(45,50]	3062	25	552	552	5
(50,55]	3466	28	552	552	5
(55,60]	3937	37	552	552	5
(60,65]	3142	37	552	552	5
(65,70]	1231	53	552	552	5
(70,75]	283	45	283	126	5
(75,80]	155	41	155	56	5